Technische Universität München

Fakultät für Physik

Quantum Communication with a Two-Atoms Network Node

Stefan Langenfeld

Vollständiger Abdruck der von der Fakultät für Physik der Technischen Universität München zur Erlangung des akademischen Grades eines

Doktors der Naturwissenschaften (Dr. rer. nat.)

genehmigten Dissertation.

Vorsitzende :		Prof. Dr. Nora Brambilla
Prüfer der Dissertation :	1.	Hon.-Prof. Dr. Gerhard Rempe
	2.	Prof. Jonathan J. Finley

Die Dissertation wurde am 20.01.2021 bei der Technischen Universität München eingereicht und durch die Fakultät für Physik am 31.01.2022 angenommen.

Abstract

A quantum internet at the global scale will be comprised of quantum nodes that are linked via quantum channels which support optical photons to bridge long distances. These nodes thus rely on a high-efficiency and high-fidelity quantum interface to make flying (photonic) qubits and stationary (matter) qubits interact. Single ^{87}Rb atoms in high-finesse optical cavities have been one of the pioneering platforms for building these nodes as this approach combines a well-controllable matter qubit with an excellent optical interface. Here we evolutionize this platform by extending it to multiple individually-useable atoms within the same cavity, which we directly make use of in two applications. In the first application, we demonstrate a random-access qubits memory for photonic polarization qubits, a building block analogous to classical random-access memories (RAM). We achieve nearly independent operation of the two memories, a coherence time of up to 1 ms and a storage-and-retrieval efficiency of 26%. We further exemplify the random-access nature by processing up to 11 qubits. As an interlude and preparation for the second application, we successfully investigate the extension of the coherence time of the atomic qubits via dynamical decoupling. We achieve a coherence time of more than 20 ms in an application-relevant scenario. Finally, and as the main result, we demonstrate a quantum repeater for quantum key distribution. We achieve unconditional security in the most efficient but also most difficult to realize key-distribution-scheme by beating the threshold in the quantum bit error rate of 11%. At the same time, we reach the theoretically predicted two-fold enhancement in rate-versus-distance scaling which highlights the repeater advantage compared to the repeater-less direct transmission. Our demonstrations present important achievements for the quantum information community and showcase that individual atoms within optical cavities remain at the cutting edge of quantum science and technology.

List of Publications

• Decoherence-protected memory for a single-photon qubit
M. Körber*, O. Morin*, S. Langenfeld, A. Neuzner, S. Ritter and G. Rempe
Nature Photonics **12**, 18-21 (2018).

• Deterministic shaping and reshaping of single-photon temporal wave functions
O. Morin, M. Körber, S. Langenfeld and G. Rempe
Physical Review Letters **123**, 133602 (2019).

• Accurate photonic temporal mode analysis with reduced resources
O. Morin, S. Langenfeld, M. Körber and G. Rempe
Physical Review A **101**, 013801 (2020).

• A network-ready random-access qubits memory
S. Langenfeld, O. Morin, M. Körber and G. Rempe
npj Quantum Information **6**, 86 (2020).

• A quantum-logic gate between distant quantum-network modules
S. Daiss*, S. Langenfeld*, S. Welte, E. Distante, P. Thomas, L. Hartung, O. Morin and G. Rempe
Science **371**, 614-617 (2021).

• Nondestructive detection of photonic qubits
D. Niemietz, P. Farrera, S. Langenfeld and G. Rempe
Nature **591**, 570-574 (2021).

• Quantum Teleportation between Remote Qubit Memories with Only a Single Photon as a Resource
S. Langenfeld*, S. Welte*, L. Hartung, S. Daiss, P. Thomas, O. Morin, E. Distante and G. Rempe
Physical Review Letters **126**, 130502 (2021).

• Quantum Repeater Node Demonstrating Unconditionally Secure Key Distribution
S. Langenfeld, P. Thomas, O. Morin and G. Rempe
Physical Review Letters **126**, 230506 (2021).

• Detecting an itinerant optical photon twice without destroying it
E. Distante, S. Daiss, S. Langenfeld, L. Hartung, P. Thomas, O. Morin, G. Rempe, and S. Welte
Physical Review Letters **126**, 253603 (2021).

• A nondestructive Bell-state measurement on two distant atomic qubits
S. Welte, P. Thomas, L. Hartung, S. Daiss, S. Langenfeld, O. Morin, G. Rempe and E. Distante
Nature Photonics **15**, 504-509 (2021).

Contents

1. Introduction

The theoretical understanding of quantum mechanics has lead to the greatest technological achievements of the 20^{th} century. The currently researched application of quantum mechanics is promised to have the same role for the 21^{st} century.

The understanding of quantum physics started with the works of Max Planck in 1900 [1], who introduced single quanta of energy exchange between light and matter to mathematically explain the spectrum of blackbody radiation. Up to this point, light had been regarded solely as an electromagnetic wave. This description could explain almost all experimental observations, most notably Young's double slit experiment [2]. Additionally, Maxwell could summarize a beautiful and seemingly complete mathematical description [3]. While Planck considered single quanta merely a mathematical trick, the explanation of the photoelectric effect by Einstein in 1905 [4] justified seeing photons, as they were later called, as the actual smallest constituent of light. The importance of these discoveries were soon acknowledged by awarding individual Nobel prizes to Planck [5] and Einstein [6]. In the following decades, quantum mechanics emerged as the evolution of Newton's mechanics to describe light and matter on a single quantum level, driven by the works of Bohr [7], de Broglie [8], Einstein [9], Heisenberg [10] and Schrödinger [11] among many others.

While this research was purely fundamental physics, it also lead to the development of new scientific tools and even impacts our everyday life, e.g. with the development of transistors, lasers for technological and medical applications, the global positioning system (GPS) or magnetic resonance imaging (MRI). This time period and its achievements can be summarized as the first quantum revolution, in which an understanding of quantum mechanics was established.

In 1982, Feynman envisioned building quantum machines, in that he realized that classical computers will not be able to simulate the underlying quantum mechanical behavior of complex systems in a reasonable time [12]. With this, Feynman already envisioned the second quantum revolution, in which quantum mechanics is actively employed to build fundamentally new devices, such as Feynman's quantum simulator. From a broader perspective, the second quantum revolution can be divided into the fields of quantum communication, quantum simulation, quantum sensing and quantum computation [13,14]. We have just passed the beginning of this revolution, which is gaining more and more momentum. Currently, the area attracting most publicity is quantum computing, as major tech giants such as IBM, Google and Honeywell have demonstrated small-scale quantum computers with first options of commercially using them [15–17]. But also quantum sensing and simulation have seen great successes [18,19].

In this work, we are mostly concerned about quantum communication, which today pro-

vides the quantum applications closest to market. This likely originates from the fact that quantum computation relies on collective effects of many qubits while quantum communication already benefits from single isolated qubits. For example, the application of quantum key distribution (QKD), i.e. the establishment of a fundamentally secure shared cryptographic key between two communication parties, is already enabled by the transmission of single photonic qubits. This is due to the fundamentals of quantum mechanics, as qubits cannot be intercepted without the communication parties noticing [20, 21]. In principle, these photons can use the optical communication backbone already existing for classical communication, which further accelerates the implementation of quantum communication. The development of quantum communication and cryptography started already in the late 1960s with the introduction of conjugate coding and a concept for quantum money [21]. Unfortunately, this was only recognized when Bennett and Brassard were inspired by this work and proposed the first QKD algorithm in 1984 [22].

Largely in parallel to the application-focused research in QKD were investigations on the fundamentals of quantum mechanics which turned out to be central to the further development of quantum communication. In 1935, the notion of quantum entanglement was introduced [9, 23]. In 1964, Bell proposed a nonlocal interpretation for this „spooky action at a distance“ [9]. This was quantified by Clauser et al. [24] which lead to significant experimental tests in 1982 by Aspect and coworkers [25]. This experiment did not only give indications for the non-locality of quantum mechanics, but it was also a strong experimental demonstration of using polarized photons as carriers of quantum information. Based on this, Ekert merged the BB84 protocol and the fundamental test of quantum mechanics to introduce an entanglement-based QKD algorithm [26]. At the latest starting from that, entanglement could be considered a resource for quantum communication, and so, long-distance entanglement distribution became a major goal of the community. This interest was further amplified by the introduction of quantum teleportation in 1993 [27], which allows to deterministically transport an unknown qubit via a lossy quantum channel, given pre-shared entanglement between sender and receiver. Since then, one of the major challenges has been to efficiently distribute entanglement between nodes of a quantum network. The usage of entanglement is not limited to QKD or teleportation, but more applications have been envisioned since then, which motivated the nomenclature of building a quantum internet [28, 29]. For example, it can also be used for distributed quantum computing [30–33] or for anonymous search, in which even the search engine would not know what you searched for [34].

The core challenge to realize long-distance entanglement distribution via optical fibers is to overcome the exponentially decaying transmission rate of single photons. The prime candidate for this are quantum repeaters, initially introduced by Briegel et al. in 1998 [35]. Just like their classical counterpart, they allow for efficient and reliable long-distance communication via lossy channels. Currently the vision is to build a quantum network employing the already available fiber backbone. Chains of quantum repeaters would be inserted into this network to connect remote quantum users. Another possibility which has emerged recently is the transmission of optical quantum signals via satellites [36], which do not suffer from exponentially decaying signal amplitudes. However, in classical communications only 1 % of the transatlantic communication goes via satellites [37]. Thus it is very likely that also in the quantum domain fiber-based communication will dominate.

These theoretical ideas have always been an interplay with experimental physicists and engineers pushing forward the boundary of what is technologically feasible. The foundation for this experimental endeavor has been the realization of the laser in 1960 by Maiman [38]. Only by having available a high-intensity monochromatic source of light, the quantum mechanical control of real and artificial atoms could be established. A following important step was the theoretical understanding and experimental realization of the trapping and cooling of atomic clouds [39–41], which quickly became a versatile tool in the laboratory. Again having these possibilities at hand, they were extended to trapping and cooling of single individual atoms, which nowadays allows to control individual atoms and photons on the most fundamental level [42, 43].

In the meantime, many different platforms for quantum communication have been established [44]. These are mainly single neutral atoms [45, 46], clouds of atoms [47, 48], single charged ions [49], vacancy centers in diamond and other solid state systems [50]. Currently all systems have their strengths and weaknesses, so that it is yet to be decided which one will be used in the future. Due to the broad range of possible applications and the challenging demands on quantum systems, also a combination of those seems possible. Independent of the specific implementation of the quantum system, many protocols in quantum communication rely on the efficient and low-noise detection of single photons. The development of this capability started already in 1949 with photomultiplier tubes, and has now culminated in basically deterministic, very low noise detection with superconducting nanowire or transition edge detectors [51]. Currently these devices necessitate cryogenic temperatures for operation, so that further developments are necessary for migrating them from the lab to the field.

With these developments, first proof of principle demonstrations of quantum networks distributing qubits and entanglement on a hundred meter scale have been realized [46, 52–56]. Due to its weaker demands on quantum control, QKD has already found its way into commercial realizations and fundamentally secure key distribution has been demonstrated over hundreds of kilometers [57], where it is currently stuck.

In this work, we push forward the physical understanding and technical implementations once again to realize quantum network and repeater nodes based on individual neutral atoms in high-finesse optical cavities. The combination of well-controllable matter qubits and a high-efficiency atom-photon interface enabled our group to demonstrate efficient atom-photon entanglement generation [58] and bi-directional storage and retrieval of single photonic qubits via a single atom [52, 59, 60]. This could be further advanced to the heralded storage of photonic qubits [61, 62] and their long-lived preservation [63]. Both aspects will play an important role in future network nodes. So far, this platform has been limited to the control of single atoms [45] or to collective effects of two atoms [64–66]. In contrast, other platforms have realized multi-qubit operation [67–73], but mostly in the direction of quantum computing and simulation, thus without a highly efficient atom-photon interface. Here we will break this limitation and develop the physics and tools to control two atoms individually within the same high-finesse cavity. Such a multi-qubit node has been proposed for distributed quantum computing [30–33] and for the construction of quantum repeater nodes [35, 74]. We will use the newly developed capabilities to first, demonstrate a random-access quantum memory. Analogous to its classical counterpart,

this can serve as a register in a quantum computer where the optical interface allows for connecting to different systems. Second, we will demonstrate a simplified version of a quantum repeater node, which can be used for QKD [75]. This node has the potential to fundamentally out-perform the achievable rate using direct transmission between the two communicating parties and thus lift the current fundamental boundaries.

The thesis is organized as follows: In Ch. 2 the experimental setup and the newly added techniques for multi-qubit operations are introduced. These tools find their first application in Ch. 3 describing the implementation of the random-access quantum memory. As an interlude, Ch. 4 gives details on our findings concerning the improvement of qubit coherence times using dynamical decoupling. This will be an important contributor to the realization of the quantum repeater scheme for quantum key distribution, which is presented in Ch. 5. Finally, Ch. 6 gives a summary and an outlook on possible improvements and future research opportunities.

2. Toolset for quantum communication with two atoms in a cavity

In this chapter, we lay the theoretical and experimental foundations for the experiments described later in this thesis. We start by giving a brief introduction to the quantum information carriers of our choice, namely single atoms and single photons and explain their fundamental interaction mechanism used throughout this thesis. We then detail the experimental setup which was initially set up in 2005 [76] and continues to serve as a state-of-the-art experiment for investigating quantum information fundamentals and applications. The following section explains which theoretical and experimental steps are necessary to advance this setup to more than one atom. Most importantly, we investigate the optical addressing of individual atoms and the avoidance of cross talk between multiple atoms via the common cavity mode. Afterwards an outlook will be given on how to scale this setup even further.

2.1. Quantum bits

In order to encode quantum information, in its elementary form a single quantum bit (qubit), two orthogonal states $|0\rangle$ and $|1\rangle$ are necessary. In contrast to classical bits, where every bit either takes the state „0“ or „1“, which are also in-principle orthogonal in that they have no overlap, quantum mechanics enables qubits to store a superposition of $|0\rangle$ and $|1\rangle$. Any qubit can then be represented as

$$|\Psi\rangle = \alpha\,|0\rangle + \beta\,|1\rangle \;\text{ with } |\alpha|^2 + |\beta|^2 = 1 \tag{2.1}$$

where α and β are complex numbers which contain the amplitude and phase information of the encoded qubit. Here we used the Dirac bra-ket notation [77]. As α and β can be continuous, this resembles analog computing [78]. However, there are fundamental advantages to qubits, such as quantum entanglement, an exponentially increasing state space with increasing qubits and the possibility of error correction. This increased capability comes at the need of controlling quantum mechanical systems at their fundamental level. One disadvantage is the limited timescale on which information can be stored. This timescale is characterized by the coherence time of the qubit carrier. It can be decomposed into a depolarization time T_1, i.e. the timescale on which population information is preserved, and a dephasing time T_2, i.e. the timescale on which the relative phase information of the qubits is preserved. While the latter only applies to superposition states ($\alpha \cdot \beta \neq 0$), the former is also relevant for energy eigenstates ($\alpha \cdot \beta = 0$).

Photonic qubits For single photons, the most used degrees of freedom for the implementation of $|0\rangle$ and $|1\rangle$ are either temporal modes (e.g. early and late) or different polarizations (e.g. horizontal and vertical), both belonging to the class of dual-rail encodings. In this thesis, the latter will be used exclusively. The following defines the photonic qubit states used throughout this work:

- $|R\rangle$
- $|L\rangle$
- $|D\rangle = \frac{1}{\sqrt{2}}(|R\rangle + i\,|L\rangle)$
- $|A\rangle = \frac{1}{\sqrt{2}}(|R\rangle - i\,|L\rangle)$
- $|H\rangle = \frac{1}{\sqrt{2}}(|R\rangle + |L\rangle)$
- $|V\rangle = \frac{1}{\sqrt{2}}(|R\rangle - |L\rangle)$.

The T_1 and T_2 times are not to be confused with the loss of single photons which is in-principle qubit-independent. T_1 and T_2 rather give the integrity of the quantum information, i.e. its accurateness, if the photon survived. The coherence times of photonic polarization qubits depend on the medium they travel in. Assuming the medium has no polarization-dependent loss (PDL) and no birefringence, T_1 and T_2 can be considered infinite. In our experiments, photon qubits travel either in free-space or in optical fibers. While the former intrinsically has only little birefringence and PDL, optical fibers do exhibit birefringence. As long as this birefringence is approximately constant over time, it can be compensated by unitary polarization rotations via e.g. optical waveplates. Thus, for the length- and timescales relevant to our experiments, photonic polarization qubits provide a faithful encoding of quantum information.

Atomic qubits For single atoms, long-lived ground states of heavy Alkali atoms have been proven to be good carriers of quantum information. Here, depending on the protocol, we use different Zeeman sub-levels of the hyperfine ground states of ^{87}Rb. As we only use long-lived ground states of ^{87}Rb to encode qubits, T_1 is in theory infinite for the timescales we investigate. However, practically T_1 is still limited as will be discussed in the experimental results of this work. T_2 depends heavily on the specific choice of atomic states. For our implementations, namely individual-atom memories using Zeeman sub-levels within the same hyperfine ground-state manifold, magnetic field fluctuations are most commonly the origin of limited coherence. This also holds for many other experiments in the Atom-Molecular-Optics (AMO) community beyond quantum information processing. In Ch. 4 we will discuss how to go beyond these limitations.

2.2. Atom-photon interaction mechanism

Quantum electrodynamics (QED) can describe the interaction of single photons with single atoms. Cavity-QED (CQED) extends this to the effects of confining atoms and photons inside a cavity, thereby enhancing the interaction between single photons and single atoms

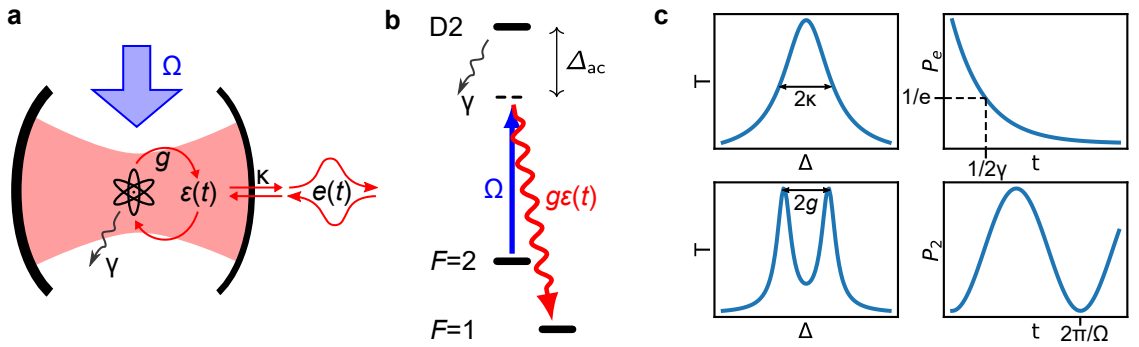

Figure 2.1.: Cavity and STIRAP schematics. **a** Illustrative explanation of the relevant rates for the atom-photon interaction inside an optical cavity. **b** Simplified view on the absorption or emission of a single photon by a single atom by means of a stimulated Raman adiabatic passage (STIRAP). **c** As there is a certain ambiguity for the definition of (g,κ,γ,Ω), we here give their definition in typical experimental scenarios. Clockwise, the four figures show an empty-cavity transmission T as a function of laser detuning Δ, the atomic excited state population P_e during spontaneous decay, the atomic population P_2 under Rabi-oscillations with Rabi-frequency Ω and the transmission T of a strongly-coupled atom-cavity system.

to a level which is usable for quantum information technologies and especially quantum communication. For an estimation of the performance of a CQED system, already three parameters are enough to determine the most important figures of merit for a communication system, namely the efficiency η, the fidelity $\mathcal{F}$ and the rate or bandwidth of the light-matter information interaction/transfer process. These three parameters are the light-matter coupling constant g, the cavity field decay rate κ and the atomic dipole decay rate γ (Fig. 2.1). They can be combined in the so-called cooperativity $C = g^2/2\kappa\gamma$, which gives the ratio of the coherent interaction process g over the two incoherent decay processes κ and γ. For example, the efficiency of the atom-photon interaction is closely related to $2C/(2C+1)$. Thus $C \gg 1$ is a necessary condition for high-efficiency and high-fidelity systems. At the same time, κ limits the light-matter interaction bandwidth, so that ideally one has $g \gg \kappa \gg \gamma$.

In this thesis, the atom-cavity quantum light-matter interface will be used for two processes. The first process is the absorption of an incoming single photon by a single atom in a stimulated Raman adiabatic passage (STIRAP) [60, 79], where the two contributors of the Raman transition are the incoming photon field $e(t)$ and an applied classical control field Ω (Fig. 2.1(a & b)). If the two light-fields are in two-photon resonance, i.e. their relative detuning equals the frequency splitting of the initial state $|g\rangle$ and the storage state $|s\rangle$, then the atom is elevated from $|g\rangle$ to $|s\rangle$. This process is in-principle independent of the single-photon detuning Δ_{ac}, i.e. the detuning of the virtual level with respect to the atomic excited states. Both arguments also hold for the second process, the so-called vacuum STIRAP (vSTIRAP) [80], which describes the emission of a single photon into the cavity mode. Here, the second contributor to the Raman scheme is the vacuum field of the cavity which gets populated during the process. Ideally, the process stops automatically after emission of a single photon, which can be achieved by choosing a final atomic state which is dark with respect to the applied control field, e.g. by dipole selection rules or a large two-photon detuning. Over the last two decades, continuous theoretical and ex-

perimental works [58, 60, 81–84] on the utilization of these interactions resulted in a deep understanding of the underlying processes and the relevant experimental parameters.

There are two main results relevant for this thesis [84]: First, the efficiency is a function of the atom-cavity detuning, $\eta = \eta(\Delta_{\mathsf{ac}})$ with distinct minima and maxima which are well understood. Second, there is a well-defined mode-matching relation between the classical control field Ω and the corresponding single-photon complex-valued temporal mode $e(t)$ which can either be absorbed or emitted.

So far, only the absorption or emission of the energy of single photons has been discussed. In the next sections, we will describe how these processes can be used for the processing of quantum information.

2.2.1. Storage and retrieval of photonic qubits on and from single atoms

In order to store a photonic qubit, the two polarization modes of the absorbed photon have to be mapped unambiguously and symmetrically onto two different atomic states. For qubit retrieval, there has to be a reversed mapping for the emitted photon which leaves no information on the atom, i.e. the final state of the atom is independent of the stored qubit.

The best currently known solution for these conditions was first introduced in 2011 [60]. In this scheme, the initial state is $|F = 1, m_{\mathsf{F}} = 0\rangle$ and the two final states are $|F = 2, m_{\mathsf{F}} = 1\rangle$ and $|F = 2, m_{\mathsf{F}} = -1\rangle$ for R- and L-polarized photonic qubits, respectively (Fig. 2.2(a)):

$$(\alpha\,|R\rangle + \beta\,|L\rangle) \otimes |1, 0\rangle \underset{\text{retrieve}}{\overset{\text{store}}{\rightleftharpoons}} \alpha\,|2, 1\rangle + \beta\,|2, -1\rangle\,. \tag{2.2}$$

Here we omit the vacuum component of the photonic mode on the right side of the formula. Note that α and β stay the same, as both atomic transitions are symmetric in their transition amplitudes, so that this common factor vanishes when normalizing the resulting state. This of course only holds if the two-photon detuning is the same for the two processes, which is ensured by relatively small magnetic fields and thus small Zeeman-induced splittings. Another point which can be noticed already here, is that the initial and final state of the atom are the same, i.e. $|F = 1, m_{\mathsf{F}} = 0\rangle$. This is not necessary for the qubit memory implementation, but it is useful as basically no re-initialization is necessary once the atom was initially well-prepared, a feature which will become relevant in our two-atom qubit memory experiments (Ch. 3). In recent experiments [84], we also found that this process works for a large range of atom-cavity detunings Δ_{ac}, which will become necessary in avoiding cavity-induced cross talk (Sec. 2.5).

2.2.2. Entanglement generation between an atom and a photon

Single atoms in optical cavities can also be used for generating entanglement between the atom and an emitted single photon. In this case, the atom emits a photon and, depending on the photon polarization, ends up in one or another state. Again, the states have to be chosen so that both polarizations have the same transition magnitude and that the

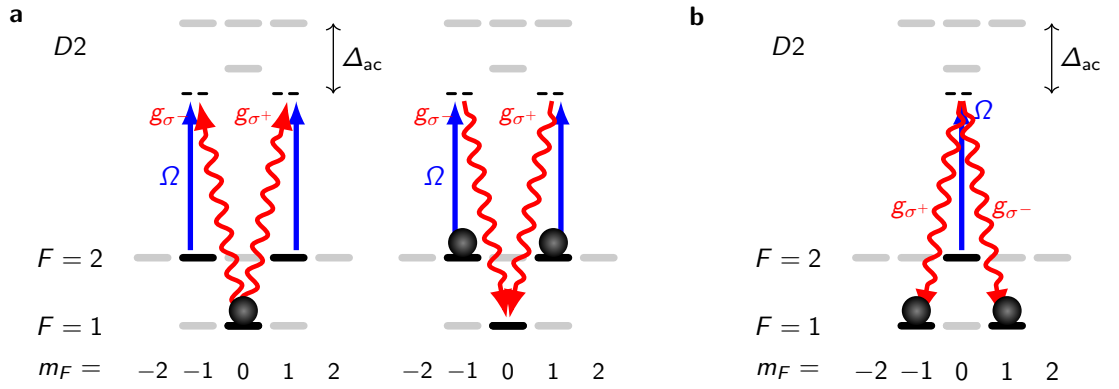

Figure 2.2.: Overview of STIRAP processes used in this work. **a** Storage and retrieval of photonic polarization qubits in the basis $\sigma^{\pm}$ by application of a classical control beam Ω. The two light-fields are in two-photon resonance but detuned from the excited states. **b** Photon generation process, in which the atomic state and the photonic polarization are entangled afterwards. All cavity interactions used in this thesis are close to the D_2-line of ^{87}Rb.

process stops after the emission of the photon. This time however, the photon is supposed to leave maximum information on the atom.

Following previous work from our group [58], we use the initial state $|F = 2, m_F = 0\rangle$ and the two storage states $|F = 1, m_F = 1\rangle$ and $|F = 1, m_F = -1\rangle$ which leads to the following process (Fig. 2.2(b)):

$$|2,0\rangle \rightarrow \frac{1}{\sqrt{2}} \left(|L\rangle |1,1\rangle - |R\rangle |1,-1\rangle \right). \tag{2.3}$$

Note, that this is one of the four maximally entangled Bell states [34], including a local π phase due to the same magnitude but opposite sign in transition amplitudes. The photon generation process stops automatically after the first photon, as the initial and the final state are in different hyperfine manifolds, so that the final two-photon detuning is $\Delta_{hf} = 6.8\,\mathrm{GHz}$. In contrast to the storage and retrieval of photonic qubits, the entanglement generation process is not easily reversible. In order to fulfill time-reversal, only the exact photonic qubit which had been emitted before can be absorbed. As this photon is entangled with the atom, the state is not known unless one of the two is measured, which adds significant experimental overhead.

In Ref. [84], we only investigated the storage and retrieval process discussed in the last section. There, each atomic population is exactly mapped to one cavity mode, either σ^+ or σ^-. Here, the full atomic population has two modes to decay into. In the following, we modify the original equations of Ref. [84] to adapt them to our situation:

$$\begin{aligned} \dot{\mathcal{E}} &= -\kappa \mathcal{E} + ig P, \\ \dot{P} &= -\left(\gamma + i\Delta\right) P + ig\mathcal{E} + i\tfrac{1}{2}\Omega S, \\ \dot{S} &= i\tfrac{1}{2}\Omega^* P. \end{aligned} \tag{2.4}$$

Here, $\mathcal{E}$, P and S are the amplitudes of the cavity field, the excited state and the storage state, respectively. The processes are quite intuitive. The cavity field $\mathcal{E}$ can either

propagate outside with rate κ, or be transferred to an atomic excited state P with rate g. P itself either decays naturally with rate γ, or back to the cavity field with rate g, or is driven to the storage state S with the STIRAP control field Ω. Now we can extend this so that the cavity has two available modes $\mathcal{E}_{1,2}$:

$$\begin{aligned}
\dot{\mathcal{E}}_{1,2} &= -\kappa\mathcal{E}_{1,2} + igP, \\
\dot{P} &= -\left(\gamma + i\Delta\right)P + ig(\mathcal{E}_1 + \mathcal{E}_2) + i\tfrac{1}{2}\Omega S, \\
\zeta &= \tfrac{1}{\sqrt{2}}(\mathcal{E}_1 + \mathcal{E}_2), \\
\dot{\zeta} &= -\kappa\zeta + i\sqrt{2}gP, \\
\dot{P} &= -\left(\gamma + i\Delta\right)P + i\sqrt{2}g\zeta + i\tfrac{1}{2}\Omega S.
\end{aligned} \tag{2.5}$$

Thus by introducing ζ as the sum of the two cavity modes we can re-use the initial equations by just replacing g by $\sqrt{2}g$, which equals an effective increase in the light-matter interaction rate and thus also increases the photon production efficiency.

2.3. Experimental setup

Figure 2.3 shows the experimental setup which was first set up in 2005 [76] and has been advanced ever since. Thus we will only give a brief recap and highlight changes which have been made to the setup. All depicted components are placed in a $L\text{x}W\text{x}H \approx 17\times17\times9\,\mathrm{cm}^3$ vacuum chamber with a pressure of $P \approx 10^{-10}\,\mathrm{mbar}$.

Table 2.1.: Cavity parameters taken form Refs. [76, 85].

mirror transmissions	$T_1 = 4 \pm 0.5\,\mathrm{ppm}$
	$T_2 = 101 \pm 2\,\mathrm{ppm}$
radius of curvature	$r = 5\,\mathrm{cm}$
mirror distance	$l = 495 \pm 2\,\mu\mathrm{m}$
mode waist radius	$w_{1/e^2} = 29.6\,\mu\mathrm{m}$
free spectral range	$FSR = 303 \pm 1\,\mathrm{GHz}$
cavity decay rate	$\kappa/2\pi = 2.7 \pm 0.1\,\mathrm{MHz}$
finesse	$F = 56000$
round-trip loss	$L_{\mathrm{rt}} = 2\pi/F = 113 \pm 2\,\mathrm{ppm}$
output directionality	$\eta_{\mathrm{out}} = 89\%$
resonator quality factor	$Q = 68 \cdot 10^6$

Cavity The core of the setup is a Fabry-Pérot optical resonator which allows for the interaction of single atoms and single photons as described theoretically in the last sections. Its core parameters are given in Table 2.1. As it directly affects the efficiency of the single-photon production process, the cavity output directionality $\eta_{\mathrm{out}} = \kappa_{\mathrm{out}}/\kappa = 89\,\%$, with $\kappa_{\mathrm{out}}/2\pi = (2.4 \pm 0.1)\,\mathrm{MHz}$ being the coupling rate via the in/out-coupling mirror and $\kappa/2\pi = (2.7 \pm 0.1)\,\mathrm{MHz}$ being the total cavity decay rate, is especially important. Additionally, κ_{out} will set the maximum bandwidth of all atom-photon interactions. With

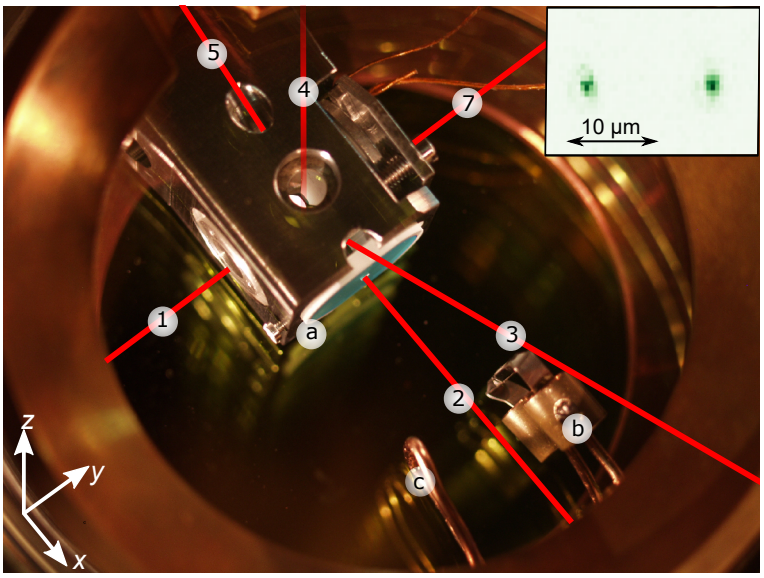

Figure 2.3.: Picture of individual-atoms-cavity setup. In the center of the image, the two mirrors of the cavity can be seen. There are up to six beams which impinge on the atoms. (1) is the in- and out-coupling beam of the cavity, which is used for all single-photon applications. (2) and (7) are standing-wave traps which confine the atoms at the center of the cavity. (3) is a retro-reflected beam used for polarization gradient cooling of the atoms and for generating fluorescence light used for imaging of the atoms (inset). (4) is π-polarized, tightly focused and can be steered onto individual atoms. (5) is the only classical beam which can have arbitrary polarization, while all others pass a polarizer and waveplates before entering the vacuum chamber. The axis of (2) is also used from the other side (not shown), from which two separate beams of different polarizations (π and $\sigma^{\pm}$) are applied. The waist of these beams is about $w_R \approx 40\,\mu\mathrm{m}$. Additionally, the depicted hardware elements are (a) mirror for creating the magneto-optical trap (MOT), (b) ^{87}Rb dispenser and (c) a coil for compensating the magnetic field induced by the current through the dispenser.

these parameters, and knowledge of the employed atomic species ^{87}Rb, the light-matter interaction parameter g can already be estimated:

$$g = \sqrt{\frac{\mu^2 \omega}{2\epsilon_0 \hbar V}} = 2\pi \cdot 5.06\,\mathrm{MHz}, \tag{2.6}$$

where ϵ_0 is the vacuum permittivity, $\omega/2\pi = 384\,\mathrm{THz}$ is the relevant transition frequency of ^{87}Rb, $\mu_0 = 1.63 \cdot 10^{-29}\,\mathrm{Cm}$ is the transition dipole moment on the frequently used transition $\left|5^2S_{1/2}, F = 1, m_F = 0\right\rangle \leftrightarrow \left|5^2P_{3/2}, F' = 1, m_F = 1\right\rangle$ [86] and $V = 3.42 \cdot 10^{-13}\,\mathrm{m}^3$ is the mode volume of the cavity [85]. Experimentally, we find $g/2\pi = (4.9 \pm 0.1)\,\mathrm{MHz}$, in good agreement with the given estimation. Together with $\gamma/2\pi = 3.03\,\mathrm{MHz}$ [86], this puts the light-matter interaction in an intermediate to strong coupling regime, and results in a cooperativity of $C = (1.47 \pm 0.11)$.

A clear path to increasing g and thus also improving the efficiency would be reducing the mode-volume V. However, having already in mind that we want to work with more than one atom in the cavity and that the different atoms should be individually addressable (see Sec. 2.4), the spatial atomic distance has to be larger than their transition wavelength

[87], which in turn necessitates a cavity mode which is sufficiently large to accommodate multiple atoms. Figure 2.4 illustrates the photon generation efficiency of a single atom at different positions along the cavity mode waist. Due to the Gaussian envelope of the cavity mode and thus the atom-photon interaction rate g, the efficiency decays for off-centered atoms.

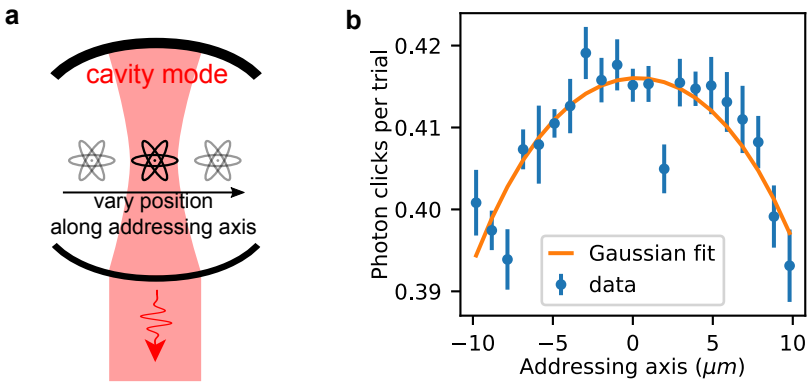

Figure 2.4.: Cavity mode size and its impact on the photon generation efficiency. Varying the atomic position along the waist position of the cavity results in different photon generation efficiencies. **a** Schematic of the different atomic positions within the cavity mode. **b** Experimental data for the photon click generation efficiency within this mode. The fit scales with $2C/(2C+1)$ where $C \propto g^2$ and g follows a Gaussian envelope.

Atom loading and trapping For the loading and trapping of the atoms, details like the different trap depths and the polarization of the trapping beams have been adjusted according to the needs of the individual protocols. These will be discussed in their respective chapters. Other than that, the loading and trapping of the atoms has not changed since the detailed investigations by former PhD student Andreas Neuzner [85]. In summary, a magneto optical trap (MOT) is prepared about 1 cm displaced from the cavity center. From there, atoms are guided in a far-detuned $\lambda = 1064\,\mathrm{nm}$ running-wave laser that transports them to the center of the cavity. At this position, the running-wave is switched to a retro-reflected standing-wave pattern which traps the atoms along this direction. Additionally, the laser field used for stabilizing the length of the cavity ($\lambda = 772\,\mathrm{nm}$) is ramped up in intensity to also form a blue-detuned, repulsive standing-wave pattern along the cavity axis. Importantly, the externally retro-reflected standing wave along the x-axis can be shifted by a motorized rotatable glass plate which changes the optical path length. This allows to re-position the center-of-mass of the atoms along this axis. In contrast, the cavity-standing-wave along the y-axis can not be shifted, so that the only option of repositioning atoms along this axis is a ramp in intensity which should refocus the atoms to the center of the attractive $1064\,\mathrm{nm}$ beam. This control of position will be the main reason why we position multiple atoms along the x-axis instead of the y-axis. The z-axis is only loosely confined by the envelope of the $1064\,\mathrm{nm}$ x-axis trap, which leaves the atoms in a two-dimensional optical lattice. Trapping times within the lattice depend largely on the applied experimental sequence, but are typically in the range of $5\,\mathrm{s}$ to $20\,\mathrm{s}$ for a single atom. In order to load n atoms, the MOT duration is tuned to have on average more than n atoms within the cavity. Excessive atoms can then be removed by optically heating them

selectively via the addressing system as already performed in Ref. [85]. Obviously, this preparation only works if the individual atoms have a distance larger than the resolution of the addressing system, which makes the n-atom preparation only almost deterministic.

Atom imaging There are multiple reasons why we want live images of the atoms (inset to Fig. 2.3). First, it is always impressive to show images of single individual atoms to visitors. Second, it guarantees that the experiments are always performed with the desired number of atoms. Third, we need to know the exact position of the atoms to program the optical addressing system to apply light fields atom-selectively as will be discussed in Sec. 2.4. Imaging is achieved via a high numerical aperture (NA=0.43) objective and a low-noise electron-multiplying charge-coupled device (EMCCD) camera whose sensitivity is mostly limited by scattered light within the apparatus. In combination, they detect the fluorescence light which the atoms emit during Sisyphus cooling [88, 89]. The cooling is integrated within the „physics“ sequences by interleaving the two with about 50 % duty cycle.

2.4. Addressing individual atoms with a classical laser beam

An enabling technology for the experiments presented in this thesis is the application of light fields onto individual atoms inside the cavity mode to drive coherent and incoherent processes atom-selectively. This is achieved with an addressing system, which was previously implemented by former PhD student Andreas Neuzner for atom shoot-out [64], and was optimized during this thesis for the aforementioned (in-)coherent manipulation purposes.

An overview of the optical and electronic setup is given in Fig. 2.5. The key components are an acousto-optical deflector (AOD), whose deflection angle depends on the applied radio frequency and a high-NA objective. The latter translates the different angles of the AOD to different atom positions and is also used for imaging of the atoms.

The addressing beam is used to apply light fields onto atoms which are distributed along the x-axis and centered along the cavity (y-)axis. To this end, the width of this beam along the addressing axis should be significantly smaller than the expected atom-atom distance, which itself is upper limited by the cavity mode size of 30 μm. However, in order to be less susceptible to mechanical drifts of the setup, it is beneficial to have the addressing waist bigger than its theoretical minimum of 0.6 μm. Here, we tuned the optical system to have a full width at half maximum (FWHM) in intensity of about 2 μm. As there is no addressing along the cavity (y-)axis, the beam is elongated three-fold along this direction. This allows to accept a larger range of possible atom positions resulting in a higher data rate.

The experimental sequence for addressing individual atoms is as follows: Based on the fluorescence images, the atoms are positioned to pre-defined trapping regions. As there is no control on every individual atom's position, the aiming of the addressing has to be adjusted to the actual exact position of the atoms. To this end, a multi-profile direct digital

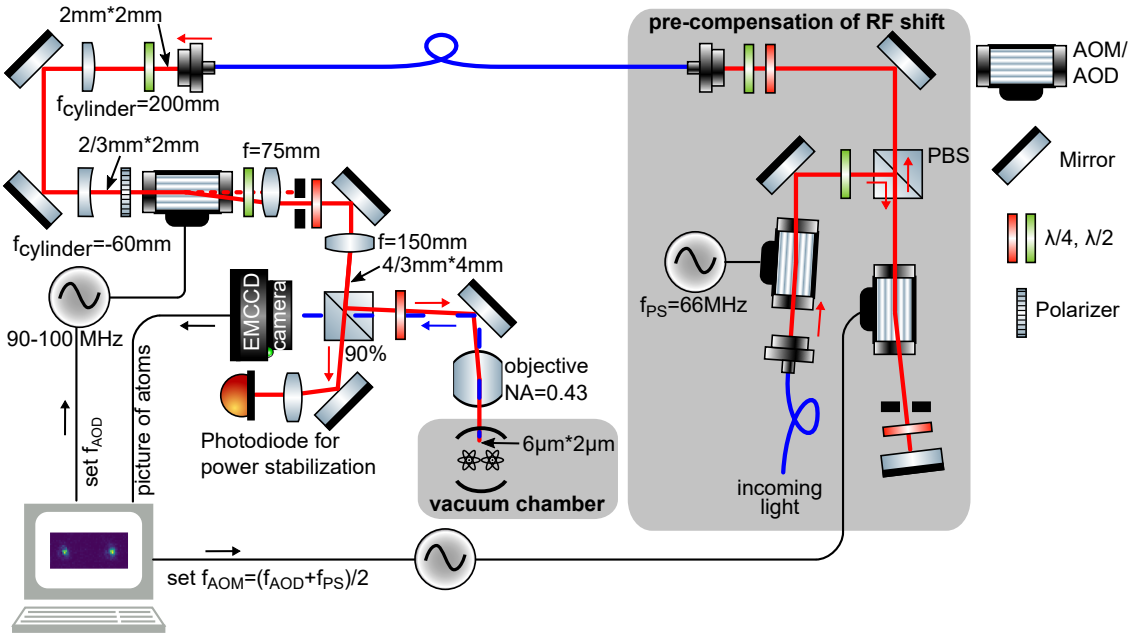

Figure 2.5.: Experimental implementation of our addressing system. Optical and electrical setup for addressing individual atoms within the cavity. Key elements are an acousto-optical deflector (AOD) and a high numerical aperture (NA) objective. The compensation of the AOD-RF-shift via two preceding acousto-optical modulators (AOMs) is necessary so that the atom always sees the same light frequency independent of its position. All numbers indicating the beam width at a given position denote the FWHM of the beam.

synthesizer (DDS) is used as a radio-frequency (RF) source for the AOD. The switching between different profiles is faster than a μs, while the actual re-addressing-time is limited by the sound propagation time in the AOD to $40\,\mu$s. As an AOD not only deflects the beam, but also changes its frequency, this shift has to be pre-compensated so that the atoms always see the same laser frequency independent of their position. To this end, a combination of two AOMs is used, one of which is frequency-shifted simultaneously with the AOD. Every light field applied through the addressing system to the atoms passes this pre-compensation. Afterwards, it is guided to the cavity setup via a polarization maintaining (PM) fiber. A combination of lenses is used to pre-condition the beam according to the design goals described above, namely a roughly $6\,\mu\text{m} \times 2\,\mu\text{m}$ beam along the y- and x-axis at the position of the atoms, respectively. While it is necessary to have a large waist at the input of the objective, care has to be taken to have a small waist at the AOD, as typically the propagating sound wave in the crystal has inhomogeneities which can not be avoided with a too large beam. An example of this effect is shown in Fig. 2.6(a), where the beam intensity profile after the AOD is compared between a too large input waist and an optimized input waist.

For experimentally determining the intensity beam profile at the position of the atoms, the beam is focused at a fixed position while the ensemble average of single atoms randomly samples different spatial positions. We employ laser-induced fluorescence state detection

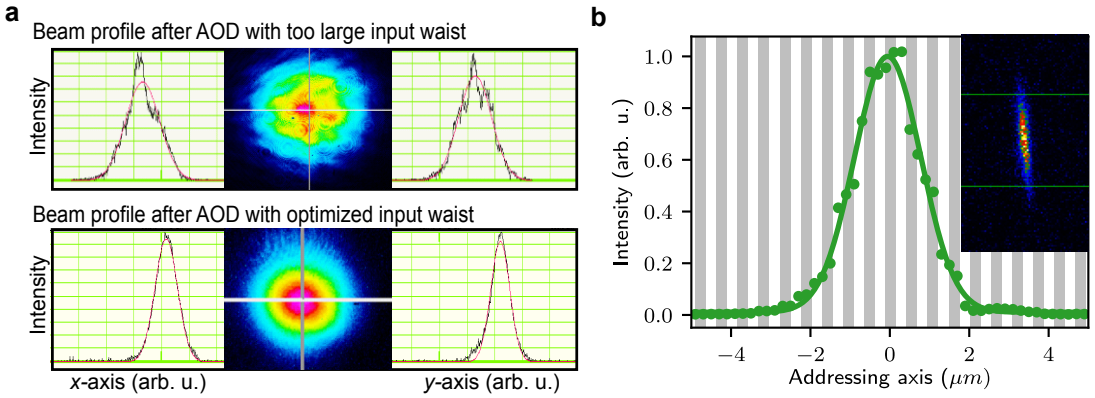

Figure 2.6.: Experimentally obtained addressing profile. **a** Beam quality measurement with a commercial beam profiler after transpassing the AOD for two different input beam configurations. **b** Intensity profile as seen by the atom together with a Gaussian fit indicating a FWHM of $(1.96 \pm 0.04)\,\mu$m. The same measurement can be used for precisely calibrating the relation between addressed pixel and applied AOD RF frequency. The grey regions indicate the periodicity of the underlying optical lattice, giving a reference for the width of the profile. The inset shows an image of the final addressing beam after the AOD, taken with the EMCCD camera usually used for atom imaging.

as the number of scattered photons picked up by the cavity and detected on a photon counter is linear in intensity for intensities small compared to the saturation intensity [90]. The resulting profile along the addressing axis is depicted in Fig. 2.6(b), together with a Gaussian fit which yields a FWHM of $(1.96 \pm 0.04)\,\mu$m. As the system is designed so that the atoms do not sample a significant fraction of the addressing beam along the y-axis, we verify the asymmetry by imaging the addressing beam on the EMCCD camera usually used for atom imaging. The result is shown in the inset of Fig. 2.6(b), where the asymmetry of the beam is nicely visible.

2.5. Cross talk between distant atoms in the same cavity

Another potential cross talk mechanism next to the cross-illumination due to the finite beam waist of the addressing system is the coupling of both atoms to the common cavity mode. The challenge then lies in having a maximum efficiency and fidelity interaction when the control field is applied to a specific atom, and having no interaction at all when the control field is not applied. Figure 2.7(a) showcases the relevant atomic level structure for the storage of photonic qubits on ^{87}Rb. A similar mechanism is present in the case of atom-photon entanglement which will be discussed in Chapter 5.

The control field is applied atom-selectively on atom A, while atom B is dark. As both atoms are prepared to the initial state $|i\rangle = |F = 1, m_F = 0\rangle$, they can both interact with the incoming photon which is close to resonance from $|i\rangle$ to some excited state. While atom A undergoes a STIRAP process to store the photon, atom B can absorb the photon and get transferred to an excited state with probability p_e. Afterwards it decays spontaneously.

This has two effects: First, the efficiency of the storage on atom A is reduced as the photon is already absorbed by atom B, and second, atom B stores a random information which might lead to infidelities when this atom is supposed to store some incoming qubit later on.

One solution to reduce the incoherent scattering probability p_e is increasing the atom-cavity detuning Δ_{ac}. However, this is only advantageous if the STIRAP efficiency does not decrease the same way. Due to the thorough investigation on the STIRAP process mentioned above, we were able to make the STIRAP efficiency almost constant over a large range of detunings [84]. Figure 2.7(b) shows a quantitative summary of the described processes as a function of Δ_{ac}. For detunings of about 100 MHz with respect to the closest excited state, the incoherent scattering side-channel becomes negligible.

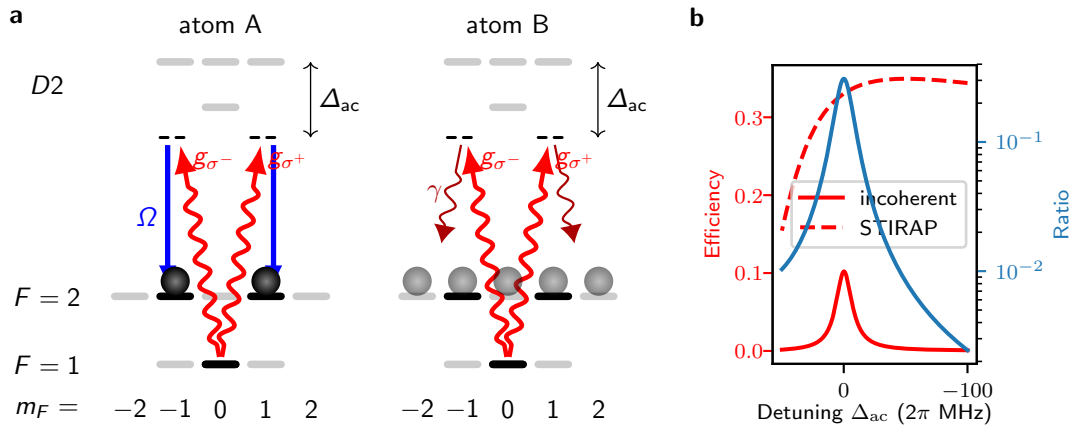

Figure 2.7.: Cavity cross talk mechanism. **a** Illustration of incoherent scattering process due to the simultaneous coupling of both atoms to the common cavity mode. Here shown exemplary for the photonic storage process but it also applies more generally to any cavity population. **b** Comparison of incoherent and unwanted scattering on atom B with the efficiency of the STIRAP process on atom A for different values of the atom cavity detuning Δ_{ac} with respect to $|F' = 1\rangle$.

A different solution, which still goes in the same direction of increasing detuning, is hiding the atoms which are not supposed to interact with the cavity population. In the memory case described above, one possibility would be having all atoms which are not supposed to interact with the atom in the other hyperfine manifold, i.e. $|F = 2\rangle$. In this way, they are detuned by $\Delta_{hf} = 6.8\,\text{GHz}$ while the desired STIRAP protocol is operated at its normal detuning. Obviously, this would require atom-selective coherent bi-directional transfers, such as stimulated Raman transitions, which we currently can not do with high fidelity due to polarization and power-stability limitations.

2.6. Outlook

For scaling to more than $n = 2$ atoms within the same cavity, atom trapping times T_{trap} have to be improved so that even T_{trap}/n is well above 5 s, an arbitrary number at which it becomes experimentally feasible to operate the experimental setup at a satisfying data rate.

This might be achievable with very deep dipole traps, as experiments with Strontium have shown recently [72]. In the same direction goes the loading of multi-atom patterns, which currently can not be performed deterministically, which further reduces the duty cycle of the data acquisition. Recently, there have been great achievements on the deterministic preparation of one-dimensional and even up to three-dimensional atomic patterns in free space with the optical tweezer technique [70–72]. A combination of this approach with our experimental setup seems feasible and will be a prominent candidate for controllably increasing the number of atoms within the cavity mode.

One natural limit to the number of atoms within the cavity mode is the size of the mode itself compared to the minimum distance of atoms either dictated by the addressing system resolution or ultimately by the lattice periodicity. Quantum gas microscopes have shown, that this ultimate limit of one atom per lattice site can indeed be reached [69]. While those typically operate in a one- or two-dimensional fashion, there has been a demonstration of addressing individual atoms in a three-dimensional lattice, although not yet with μm resolution [91]. One of the reasons why it is difficult to combine the aforementioned techniques with high-finesse optical cavities is probably that there is a mismatch between the mode volume of the cavity, which should be as small as possible for QIP applications, and the continuously increasing number of atoms and thus size of optical lattice or tweezer experiments. In addition, there is only limited optical access to atoms within a Fabry-Pérot resonator. One possible solution could be distributing multiple atoms over multiple cavity mode maxima along the cavity instead of squeezing all atoms into a single maxima [92]. Another possible solution to marry the two fields are nano-structured cavities with optical tweezers [93]. They combine small mode volumes with many trapping sites which can be individually addressed. However, currently these techniques are still at an infancy and do not reach the level of control single atoms in Fabry-Pérot style cavities have reached over the last 20 years.

3. A random-access qubits memory

The content of this chapter has been published in:
A network-ready random-access qubits memory
S. Langenfeld, O. Morin, M. Körber and G. Rempe,
npj Quantum Information **6**, 86 (2020).

In the last chapter, we have developed the necessary tools to process quantum information with multiple individual neutral atoms inside a high-finesse optical cavity. Here we will make use of this toolset to experimentally demonstrate a random-access two-qubits memory which can be used in a future quantum internet as it also in-principle allows to perform quantum computations on the stored qubits. We will start by giving an overview on qubit memories in general and the different evolutional steps towards a random-access computing memory. Afterwards the theory and experimental implementation of relevant processes new to this work will be discussed. We will then discuss the experimental results and provide an outlook on future research opportunities.

3.1. Overview

Classical information storage is based on the measurement and repeated preparation of individual bits. This approach does not work for quantum information, as, following the Kopenhagen interpretation of quantum mechanics, the measurement of a quantum state collapses the quantum mechanical wave function and thus alters the encoded information [10]. As is also described by the no-cloning theorem [20], quantum information can thus not be repeatedly processed or stored. This calls for the storage of quantum information in so-called qubit memories, which faithfully preserve any quantum-mechanical superposition state without knowledge thereof. As is the case for classical memories and classical information processing, qubit memories are part of most protocols in quantum communication and computation. In computation, they are typically used to first, prepare and preserve a set of input states, and afterwards, to save a computation result. This requires qubit memory implementations which fulfill the five criteria of DiVincenzo [94] and thus enable scalable quantum computation. For quantum communication, two additional criteria are necessary, namely to interconvert stationary and flying qubits and the ability to transmit these flying qubits between specified locations. While the latter is achieved by modern fiber- or satellite networks supporting optical photons as flying qubits, the former requires a high-efficiency and faithful interface between the well-isolated stationary qubit memory and the flying optical photons.

Optical qubit memories provide this interface and allow for the (bi-)directional conversion between photon and matter qubit carriers. While still most of the developed platforms only allow for the (efficient) emission of optical photons [95], some systems are also able to convert in both directions, which we call store-and-retrieve qubit memories [60,96–101]. As our system falls into this most general category, we will restrict ourselves to the discussion of this group.

The natural next step starting from single qubit memories is the extension to multimode memories. The first and obvious advantage is the scaling to larger systems for constant resources. The current capacity leaders are memories based on atomic frequency combs in solid-state systems. They shape their intrinsic inhomogeneous broadening into a comb-like absorption spectrum. Photons are then stored in a superposition of different comb-teeth and rephase after a time given by the inverse tooth-separation. The availability of many comb-teeth allows for the storage and retrieval of many temporal modes.

This technique offers multiple advantages. It is on-demand [102], i.e. the time of emission can be arbitrarily chosen by transferring the population to a state outside of the comb. It has demonstrated up to 100 modes [103] and features a coherence time of about a millisecond [104], with further advancements in reach [105]. However, it is also intrinsically limited to serial storage and retrieval of the qubits without the possibility to further process the information stored in the different modes. Furthermore, the mode capacity is traded off against optical bandwidth [106] and requires a minimum optical depth [107].

Random-access qubits memories (RAQM) mitigate the first disadvantage by providing access to specific modes of the memory where the access-time is independent of which mode was chosen. The first demonstration of this kind was performed recently in a segmented magneto-optical trap of neutral atoms [101]. Acousto-optical deflectors (AODs) steer control pulses and the photonic qubits to a specific spatial mode of the MOT where then electromagnetically induced transparency (EIT) is used to store and retrieve the photonic qubits. Due to the limited coherence time of $28\,\mu\mathsf{s}$, only 3 modes could be used simultaneously, while in-principle up to 105 modes were available. While demonstrating an important step for RAQMs, their system design has some major flaws. First, the usage of a MOT only allows for limited coherence times as already mentioned. Second, the precious photonic qubit carriers have to be directed via lossy AODs, which almost fundamentally limits the achievable efficiency. Most importantly, however, the usage of spatially separated modes without common interaction channel misses out on many benefits achievable with RAQMs.

These benefits are enabled by the ability to compute on- and between different qubits stored in the RAQM, leading to what one might call computing memories. In essence, they form the synthesis of small quantum computers and optical qubit memories, which both sides can benefit from. For example they can be used to boost quantum communication via error correction [35, 108, 109] or they can advance quantum computation by enabling the distribution of computations onto optically-connected computing modules [31].

Although we do not demonstrate the computing aspect of this synthesis, single atoms in optical cavities are known to feature single- and two-qubit gates as well as means to prepare and measure qubits [45, 66], which represent the universal building blocks of a small-scale

quantum computer [94]. Here we demonstrate a random-access qubits memory in this platform. While we currently only use two atoms and thus provide the capacity of two qubits, this is already enough to fulfill the requirements for many protocols which rely on the combination of computing and communication [35, 108, 110, 111]. We believe that we have identified and solved the obstacles which arise when transitioning from a single qubit to multiple qubits within the same cavity. The further scaling to larger numbers of atoms is not to be underestimated, but represents mainly a technological effort.

3.2. Performance definition and characterization

The two most important figures of merit for a qubit memory are its efficiency and fidelity which both can be potentially storage-time dependent.

The efficiency describes the integrity of the carrier. For a qubit memory, it quantifies how likely the combined storage-and-retrieval process is successful. Here we define it as:

$$\eta = \frac{n_{\mathsf{out}}}{n_{\mathsf{in}}}, \tag{3.1}$$

where n_{out} is the average number of output photons if there were on average n_{in} input photons. For ensemble-based memories, the re-emission of an excitation depends on the collective phase of all emitters which leads to a coherence and thus storage-time-dependent efficiency. In contrast, there is no such collective effect for single atoms in cavities which makes the efficiency time-independent. We are interested in the performance for single-photon qubit inputs. However, as we will describe in Sec. 3.3, for practical reasons we use weak coherent pulses to probe the memory. As a single atom can at most absorb a single photon, higher photon number contributions of the coherent pulse bias the obtained efficiency to lower numbers. For our findings, this will be compensated by extrapolating to $n_{\mathsf{in}} \to 0$ [112]. Experimentally, the efficiency can be accessed by calibrating the input photon number and then measuring the memory output with single-photon counters.

The fidelity describes how faithfully the memory preserves the encoded quantum information during its storage time. For a given input, it is defined as the overlap between this input and the actually received, potentially mixed, output:

$$\mathcal{F} = \langle \psi_{\mathsf{in}} | \, \rho_{\mathsf{out}} \, | \psi_{\mathsf{in}} \rangle \,, \tag{3.2}$$

where ρ_{out} is the density matrix describing the received output state. In principle, it can be accessed by repeatedly probing the memory with well-known pure states $|\psi_{\mathsf{in}}\rangle$ and performing polarization tomography on the ensemble of output photons. For a qubit memory, this can be simplified to only measuring the output photons along the qubit-basis defined by the input. For example, when probing the memory with H-polarized input qubits, only measurements in the (H,V) detection basis are necessary. The fidelity is then given by:

$$\mathcal{F} = \frac{n_{\mathsf{H}}}{n_{\mathsf{H}} + n_{\mathsf{V}}}, \tag{3.3}$$

where $n_{\mathsf{H,V}}$ denotes the number of clicks in the (H, V) single photon detectors.

3.3. Experimental implementation

Atom trapping The atoms are trapped in a two-dimensional optical lattice with trapping frequencies $\omega_{\mathsf{trap}}/2\pi = (220, 335, 3.3)\,\mathsf{kHz}$ along the x, y, z direction, respectively [63]. The same trap depths were used for earlier experiments on a single-atom qubit memory, where the trap intensities had to be as small as possible to reduce off-resonant scattering while still trapping the atom reliably [63]. For reasons of compatibility, the same parameters were used for the demonstration of this two-atom memory. The polarization of the trap along the x-axis is linear, while the polarization of the trap along the cavity (y-)axis is elliptical, as this improves the trapping of atoms at low trap depths [85]. This ellipticity leads to a vector AC-Stark shift, which thus acts similar to a magnetic field. This shift however depends on the overlap of the atomic wave function with the trapping light, and thus is a function of the number of mechanical excitations along this axis, n_y. As any differential energy between the two qubit carrying atom states has to be constant, n_y has to be constant. This is easiest achieved by fixing $n_y = 0$ by employing motional ground-state cooling within the experimental sequence which will be discussed in the next section.

For the two-qubit memory, two atoms have to be trapped and coupled to the common cavity mode. As both atoms serve identical roles, they are coupled equally to the cavity by placing them symmetrically to the cavity center. The maximum interatomic distance is restricted by the cavity mode size while its minimum is limited by the individual-atom addressing beam profile. These aspects will be investigated in the memory sequence itself and are given together with the experimental results. After the two atoms are at the desired positions, the protocol of the two-qubit memory starts, typically with a repetition rate of $500 - 1000\,\mathsf{Hz}$.

3.3.1. Single-atom memory protocol

For each individual atom, the implemented protocol follows previous work on single-atom qubit memories in the same setup [60,63]. We will thus focus our attention on the relevant modifications for scaling such a system to two or even more qubits per cavity. The experimental sequence is divided into state preparation, the storage of photonic input states, the (passive) waiting time and the retrieval of single photons (Fig. 3.1). This protocol allows to characterize the most-important parameters of our qubit memory and is also close to a realistic implementation.

State preparation The initial state of the employed protocol is $|F = 1, m_{\mathsf{F}} = 0, n_y = 0\rangle$. To end up in this state, a combination of Raman resolved-sideband cooling, incoherent optical hyperfine pumping to $|F = 1\rangle$ and Zeeman-selective optical pumping to $|m_{\mathsf{F}} = 0\rangle$ is applied. Zeeman selectivity is achieved by using a π-polarized beam which is close to resonance to the transition $\left|5^2S_{1/2}, F = 1, m_{\mathsf{F}}\right\rangle \leftrightarrow \left|5^2P_{3/2}, F' = 1, m_{\mathsf{F}}\right\rangle$. As this transition is dipole-forbidden for $m_{\mathsf{F}} = 0$, $|F = 1, m_{\mathsf{F}} = 0\rangle$ becomes a dark state so that population accumulates there. Another dark state of this transition is any population which ends up in $\left|5^2S_{1/2}, F = 2\right\rangle$, as the applied light field is far-detuned. This population is repumped

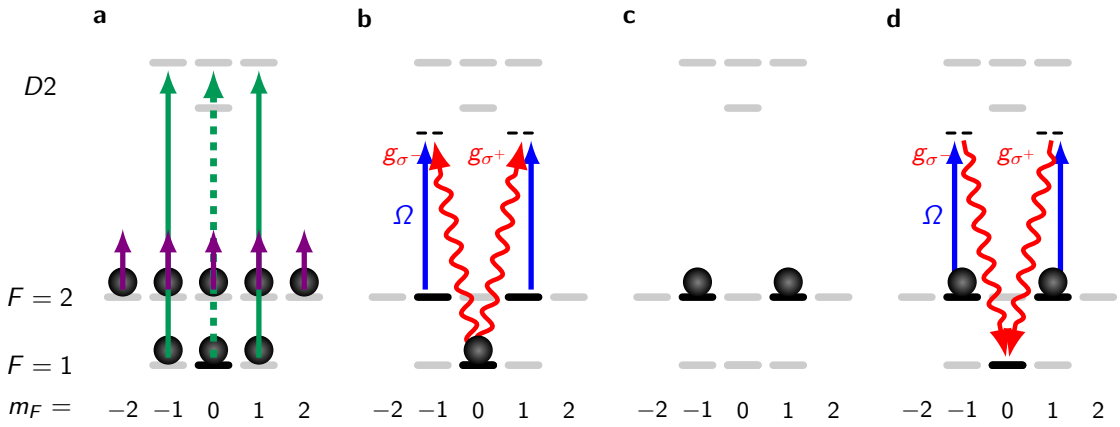

Figure 3.1.: Individual-atom qubit memory. **a** State preparation consisting of Zeeman pumper (green), where a dashed line indicates a forbidden transition, and the repumper (purple), where the exact transitions are not shown for clarity. The additionally necessary ground-state cooling is described in the main text. **b** Absorption of an incoming single photon. The polarization information of the photon is mapped to atomic states. **c** During the waiting time, the atom is dark and follows free evolution. **d** Generation of a single photon with encoded quantum information.

to the $|F = 1\rangle$ manifold by application of a combination of π- and $\sigma^{\pm}$-polarized beams which couple $|F = 2\rangle$ to all excited manifolds $\left|5^2P_{3/2}, F'\right\rangle$. This prevents the formation of any dark state within $|F = 2\rangle$. For cooling to the motional ground state along the y-axis, i.e. $n_y = 0$, Raman resolved-sideband cooling uses a combination of coherent transitions from $|F = 1, n_y\rangle$ to $|F = 2, n_y - 1\rangle$ and incoherent pumping from $|F = 2, n_y - 1\rangle$ to $|F = 1, n_y - 1\rangle$. Thus, per loop, one quanta of mechanical excitation is removed from the atom until $n_y = 0$ is reached. To this end, we apply a total of 50 loops. The whole preparation takes about 1 ms in total.

This preparation is done for both atoms simultaneously using the global beams of the atom-cavity setup. Thus, in-principle no modification is necessary for two or more qubit memories. However, experimentally we found that the Rabi-frequency of the resolved-sideband Raman transition significantly varies along the addressing (x-)axis. To this end, all light intensities had to be optimized for the actual atomic positions which is simplified by the symmetric positioning of two atoms with respect to the cavity center.

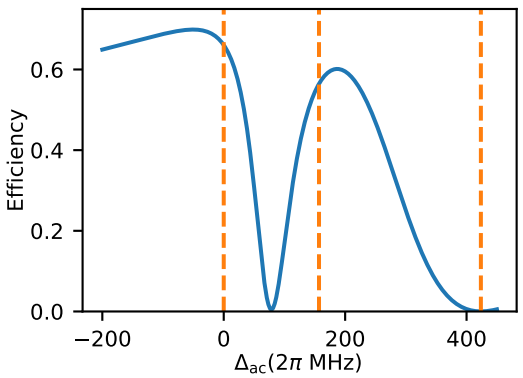

Figure 3.2.: Theoretical efficiency of the STIRAP process. Solid line shows efficiency including the cavity escape efficiency $\eta_{\text{out}} = 0.89$. Dashed lines show the positions of the relevant excited states $|F' = \{1,2,3\}, m_F = \pm 1\rangle$.

Absorption We use weak coherent pulses, typically with an average photon number $\bar{n} = 1$, to simulate single-photon input states to the qubit memory. The temporal mode is

shaped via an acousto-optical modulator so that the resulting intensity profile follows a sech^2 profile with characteristic photon length of $t_{\mathsf{ch}} = 1\,\mu\mathsf{s}$. These pulses are sent onto the high-transmission mirror of the optical cavity, which for historic reasons is labeled „backprobe“. At the (known) time at which the photon enters the cavity, the control pulse of the STIRAP is applied atom-selectively via the optical addressing system (Sec. 2.4) which transfers the photonic qubit onto the addressed atom with a certain efficiency. Otherwise the photon is reflected, absorbed or scattered and the atom is either incoherently transferred to another state or just stays in the initial state. The intended transition is given by

$$(\alpha\,|R\rangle + \beta\,|L\rangle)_p \otimes |1,0\rangle_a \xrightarrow{\text{store}} \alpha\,|2,1\rangle + \beta\,|2,-1\rangle\,. \tag{3.4}$$

As was introduced in Ch. 2, the efficiency of this process is a function of the atom-cavity detuning Δ_{ac}, which is plotted in Fig. 3.2. The efficiency is almost constant for a wide range of negative detunings, which allows to use it for minimizing cavity-induced cross talk as will be described later in this chapter.

Waiting time The atoms preserve the stored qubit for a time τ. However, during that time, atomic superposition states undergo a Larmor precession due to the applied magnetic guiding field of $\delta_{\mathsf{L}}/2\pi = 30\,\mathsf{kHz}$, resulting in the state:

$$\alpha\,|2,1\rangle + \beta\,|2,-1\rangle \xrightarrow[\text{time}]{\text{evolution}} \alpha e^{i\delta_{\mathsf{L}}\tau}\,|2,1\rangle + \beta e^{-i\delta_{\mathsf{L}}\tau}\,|2,-1\rangle\,. \tag{3.5}$$

Photon retrieval For emission of a photon and thus retrieval of the stored qubit, a vSTIRAP is used. As part of this process, a control pulse is again applied via the optical individual-atom addressing system. The spatial intensity profile of this beam was analyzed in Sec. 2.4. As the STIRAP is adiabatic and thus non-linear in control-field intensity, the effective spatial beam profile relevant for the STIRAP process differs from the intensity beam profile given earlier.

Figure 3.3 displays the analysis of the effective spatial profile of the photon generation efficiency. As the STIRAP is also non-linear in time and saturates at some point (Fig. 3.3(a)), we analyze the profile for different cut-offs in time. Figure 3.3(b) displays the experimentally obtained spatial profiles which are acquired similar to the intensity profile but with single-photon production in contrast to resonance fluorescence. For the full STIRAP duration ($t_{\mathsf{c}} = 12\,\mu\mathsf{s}$), there is abundant control power so that even atoms which are not at the center of the beam are saturated and efficiently emit a photon. This broadens the overall spatial profile. In contrast, if the cut-off is too early ($t_{\mathsf{c}} = 7\,\mu\mathsf{s}$), the process does not reach the necessary saturation to completely transfer the excitation from atom to photon, so that the beam profile is more narrow but the resulting efficiency is reduced. We chose $t_{\mathsf{c}} = 8\,\mu\mathsf{s}$ as a trade-off between these two effects, which results in a relevant width of the addressing profile of $\mathsf{FWHM} = (2.5 \pm 0.1)\,\mu\mathsf{m}$. Note that in principle this analysis also holds for the STIRAP employed for the storage of the input photon states. However, this process relies on the input of photonic states so that ideally no transition is driven in the „saturation regime“, i.e. when there is maximum control power but no single-photon input. Obviously this does not hold if the unaddressed atom is already in the storage state, as the write-in control beam can also lead to a read-out of the unaddressed atom.

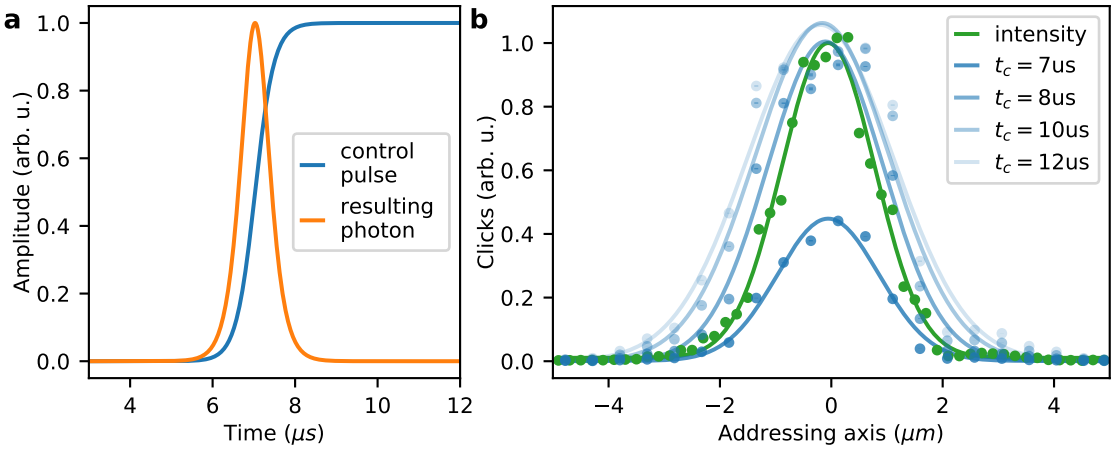

Figure 3.3.: Effect of temporally cutting the STIRAP control beam on the spatial addressing profile. **a** Theoretical control pulse and resulting photon for the photon generation process. **b** Effective spatial profile when using the addressing beam for photon generation via a STIRAP. The timing given in the legend corresponds to a cut-off time in part (a) at which the control pulse is prematurely turned off. Due to saturation of the atom, the different cut-offs lead to different effective spatial profiles. The green curve serves as a reference and is obtained via resonance fluorescence, which does not saturate for the employed optical power and thus faithfully depicts the spatial intensity profile.

Unfortunately, this was only realized after the project and thus remains an opportunity for future improvements.

In summary, the atom-photon state is given by:

$$\alpha e^{i\delta_L \tau} |2,1\rangle + \beta e^{-i\delta_L \tau} |2,-1\rangle \xrightarrow{\text{retrieval}} (\alpha e^{i\delta_L \tau} |R\rangle + \beta e^{-i\delta_L \tau} |L\rangle)_p \otimes |1,0\rangle_a . \tag{3.6}$$

The information carried by the photons generated in this process is afterwards analyzed in a single-photon polarization-resolved detection setup, which will be described in the next section.

3.3.2. Detection and probing setup

For the characterization of the two-qubit memory performance, the atomic memories are probed with photons of different input polarizations. After the storage time, the retrieved photonic qubits are analyzed in a polarization tomography setup. As input and output photons enter/leave via the same high-transmission mirror of the cavity, both photon preparation and analysis have to be combined in a single setup, which is depicted in Fig. 3.4.

Starting from the left, photons emitted by the atom pass a 10 m optical single-mode fiber. The varying birefringence of this fiber is compensated via a combination of three waveplates so that the polarization of the photons traveling from/to the atom is preserved. Afterwards, the path is split to combine two detection setups which potentially have different detection bases. Each detection setup consists of motorized waveplates to change the

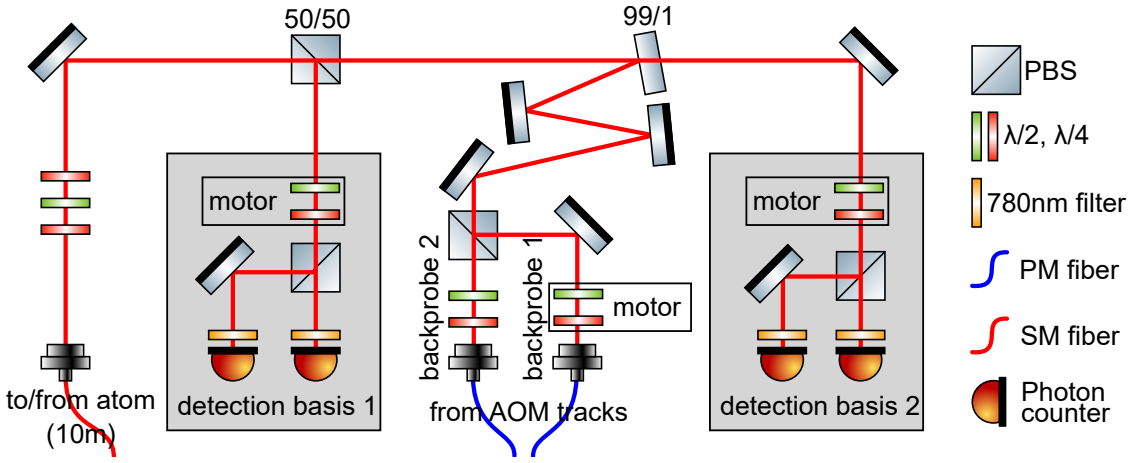

Figure 3.4.: Detection setup used for two-atom memory. Two detection setups are combined with two independent backprobes to be able to test the memories with arbitrary input combinations.

detection basis, a polarizing beamsplitter to project onto orthogonal polarizations, 780 nm interference filters to block background light and single-photon detectors for counting photons. The backprobes are combined into one of these setups via a 99/1 beamsplitter which allows to have maximum detection efficiency of the true single photons emitted by the atoms while introducing additional losses to the backprobes which are only weak coherent pulses. Thus losses will be compensated by tuning the average photon number in front of the cavity. In a realistic application, this beamsplitter would be replaced by an optical circulator.

3.3.3. Two-atom sequences

The qubit memory protocol is applied individually on both atoms. For two identical atoms, the simplest access patterns for a random-access qubit memory are $A_W B_W A_R B_R$ and $A_W B_W B_R A_R$, where (A_W, B_W) are the write-in and (A_R, B_R) the read-out operations on atom A or atom B, respectively. The access-time to the individual memories is given by the response-time of the acousto-optical deflector. The resulting limitations on the access-patterns are illustrated in Fig. 3.5. Any switching between two atoms takes a minimum of $40\,\mu s$. In addition, for the rephasing of the initially stored qubit, the readout is timed to a multiple of the inverse precession frequency $\tau_L = 1/2\delta_L$. This results in minimum storage times of $(96, 16)\,\mu s$ for atom (A, B) in the $A_W B_W B_R A_R$ configuration and $96\,\mu s$ for both atoms in the $A_W B_W A_R B_R$ configuration.

Figure 3.5(c) shows an extension of the $A_W B_W B_R A_R$ scenario, where the intermediate write and read on atom B is repeated k times, denoted $A_W[B_W B_R]^k A_R$. This illustrates one of the advantages of random-access qubit memories which already becomes apparent with as little as two memories. One can re-use one memory while storing on the other one, usable e.g. for synchronization tasks. This rather simple extension to many qubits is possible because in principle no re-initialization of the memory is necessary, as the initial state of

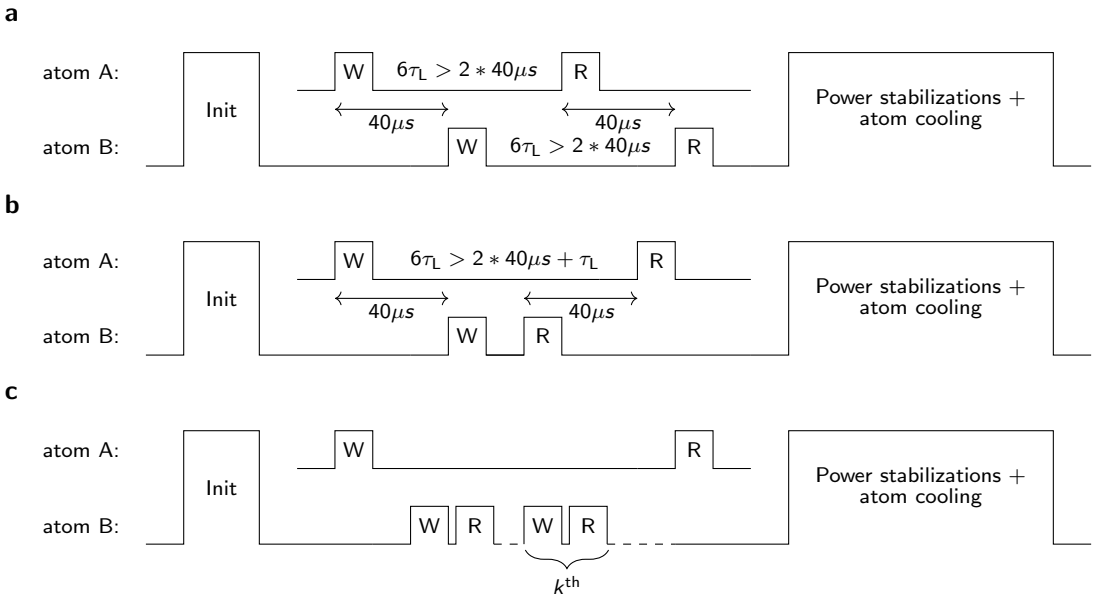

Figure 3.5.: Access patterns for two-qubit memory. All sequences start with a global state initialization and end with atom cooling and auxiliary tasks such as power stabilization of specific beams. **a** $A_W B_W A_R B_R$, due to the minimum switching time of the AOD of $40\,\mu s$, the minimum storage time for both memories is $6\tau_L = 96\,\mu s$. **b** $A_W B_W B_R A_R$, here the minimum storage time is different for the two atoms. If atom B is not re-addressed because it is planned from the beginning to directly read it again, its minimum storage time is $\tau_L = 16\,\mu s$. If this is not known, the absolute timings of the pulses do not change compared to part (a), just which atoms they address. **c** $A_W[B_W B_R]^{k \leq k^*} A_R$, an arbitrary number k^* of write-read attempts is performed on atom B during the storage time of atom A.

our qubit memory implementation is also the final one. The limits of that will be discussed in the experimental results.

3.4. Experimental results

3.4.1. Cross talk elimination

In order to achieve high-efficiency and high-fidelity multi-qubit memories, cross talk between the individual memories has to be avoided. We identified two main cross talk mechanisms. First, the STIRAP control field is applied through an addressing system with finite beam waist. Thus, depending on this waist and the atomic distance, there will be cross-illumination. Second, both atoms are coupled to the same cavity mode. Thus, even if the classical control field is applied perfectly, in- and outgoing photons are not atom-selective and thus can couple to both atoms. In the following we will describe how to mitigate these effects.

Classical cross-illumination The addressing system beam waist has already been discussed in Sec. 2.4 and Sec. 3.3.1. The only free parameter to optimize the unwanted cross-illumination is thus to vary the distance between neighboring atoms. Here we will use the qubit memory protocol itself to evaluate the introduced cross talk. We utilize the $A_W B_W A_R B_R$ sequence with minimum storage time and circular polarization qubits. Atom A and atom B are probed with orthogonal input qubits (R,L) to maximally highlight any cross talk between the two memories. Figure 3.6 shows the fidelity and efficiency of atom A for a range of interatomic distances. For the maximum distances, fidelity and efficiency are in the range known from single-atom experiments, namely $> 90\,\%$ fidelity and $\approx 25\,\%$ efficiency. For intermediate distances, the fidelity and efficiency stay at this level with irregularities which we attribute to statistical fluctuations. For distances below about $4\,\mu$m, the fidelity decreases significantly. At the same time, the error bar of the acquired data increases as the two atoms become less distinguishable which results in a less frequent preparation success. Both effects are linked as they originate from the limited resolution of the addressing and imaging system. Based on this, we only use atomic patterns where the interatomic distance is at least $6\,\mu$m.

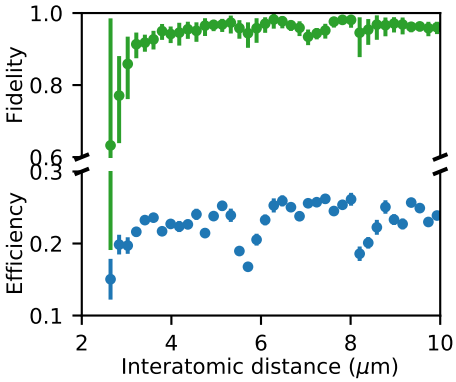

Figure 3.6.: Minimum interatomic distance for low cross-illumination. Depicted is the efficiency and fidelity of atom A in the $A_W B_W A_R B_R$ access pattern, probed with orthogonal circular polarizations.

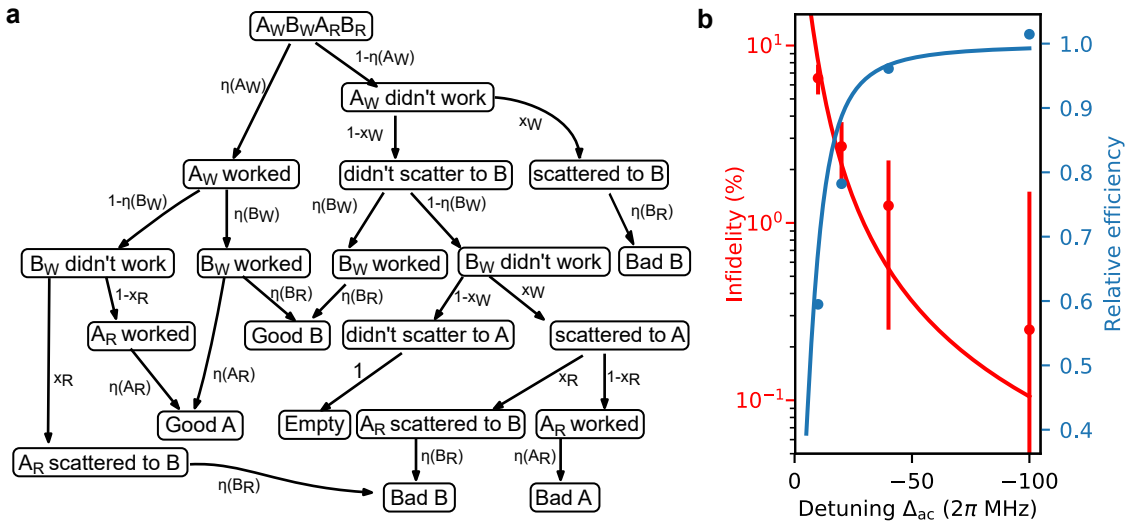

Figure 3.7.: Single-photon detuning for low cross talk. **a** Markov model to track possible outcomes of the memory operation. x_W and x_R denote the detuning-dependent scattering probability of the unaddressed atom for the write-in and read-out, respectively. **b** Experimental results and obtained theory curve for impact of cavity-induced cross talk on fidelity and efficiency of atom A.

Cavity-induced cross talk The cross talk via the common cavity mode has already been discussed in general in Sec. 2.5. Here we use the qubit memory protocol to analyze this effect quantitatively and decide on experimental parameters for its implementation. Figure 3.7(a) gives the model which was used to estimate how this effect translates to an impact on the fidelity.

We again use sequence $\mathsf{A_W B_W A_R B_R}$ with minimum storage time and orthogonal circular input qubits for the two atoms. Figure 3.7(b) shows the infidelity and relative efficiency of atom A for different atom-cavity detunings Δ_{ac}, which is defined with respect to the transition $|F = 1, m_{\mathsf{F}} = 0\rangle \leftrightarrow |F' = 1, m_{\mathsf{F}} = 1\rangle$. For small negative detunings, the infidelity is high and the relative efficiency is low. This is according to expectation as there is a high probability that the unaddressed atom interacts with the cavity population. With increasing negative detunings, this probability decreases while the STIRAP efficiency stays about constant [84]. As a consequence, the infidelity becomes negligible for a detuning of $\Delta_{\mathsf{ac}}/2\pi = -100\,\mathsf{MHz}$ for which we experimentally obtained an incoherent scattering probability per input photon of only $(0.15 \pm 0.01)\,\%$ and a coherent STIRAP write-in efficiency of $(38 \pm 3)\,\%$. The experimental results are well-matched by the according theoretical model (Fig. 3.7(a)). Finally, we set $\Delta_{\mathsf{ac}}/2\pi = -100\,\mathsf{MHz}$ for all experiments presented in the following. Using even larger detunings does not gain much in fidelity and requires significantly more and well-stabilized optical power of the control beam.

Cross talk summary In order to characterize how well these cross talk mechanisms are suppressed, we now probe the qubit memories with different inputs and with different access patterns. Table 3.1 summarizes the obtained results. We use a combination of parallel and orthogonal circular input qubits to investigate whether there is any population exchange between the two memories. As the achieved fidelity equals the single-atom performance [63] independent on whether orthogonal or parallel inputs were used, we conclude that there is no noticeable population cross talk. The same analysis is done for phase cross talk with linear, i.e. superposition, inputs. Here we set the write-in time of atom B so that the qubit which is already stored in atom A has rephased to its initial state. This ensures that orthogonally polarized input qubits are still orthogonal when they are stored on the two different atoms. Again, there is no significant difference between orthogonal or parallel inputs which signals the independent operation of the two memories. Note that the fidelity of atom A in the $\mathsf{A_W B_W B_R A_R}$ pattern is reduced by about $2\,\%$. This is due to the limited coherence time of the memory in combination with the longer storage

Table 3.1.: Summarizing the two-qubit performance. Fidelity in percent for two access patterns and four polarization combinations. In the $\mathsf{A_W B_W A_R B_R}$ scheme, the storage times are $133\,\mu\mathsf{s}$ for both atoms while in the $\mathsf{A_W B_W B_R A_R}$ scheme they are $(183, 83)\,\mu\mathsf{s}$ for atom A and B, respectively.

	$\mathsf{A_W B_W A_R B_R}$		$\mathsf{A_W B_W B_R A_R}$	
input pol.	atom A	atom B	atom A	atom B
$\|R\rangle_{\mathrm{A}}, \|R\rangle_{\mathrm{B}}$	97.0 ± 0.7	96.8 ± 0.6	97.2 ± 0.4	97.3 ± 0.3
$\|R\rangle_{\mathrm{A}}, \|L\rangle_{\mathrm{B}}$	97.8 ± 0.6	96.4 ± 0.4	97.0 ± 0.3	98.1 ± 0.5
$\|H\rangle_{\mathrm{A}}, \|H\rangle_{\mathrm{B}}$	95.4 ± 1.3	93.3 ± 1.4	92.1 ± 0.9	94.3 ± 1.2
$\|H\rangle_{\mathrm{A}}, \|V\rangle_{\mathrm{B}}$	94.5 ± 1.2	95.2 ± 1.4	92.1 ± 1.2	94.6 ± 1.8

time of atom A in this pattern. The coherence time of our qubits memory implementation will be discussed in the next section.

In the analysis described so far, the storage and emission for both atoms was probabilistic, i.e. not all of the storage attempts were successful. When postselecting on a retrieved photon for both memories, i.e. heralding the success of storage and retrieval, the average fidelity as defined in Table 3.1 on average increases by 0.6 %. While this is within error, it also makes sense intuitively that the fidelity increases as the relative probability of excitation of the wrong atom decreases.

3.4.2. Efficiency

The fidelity is sensitive to even small admixtures of the wrong polarization input. This is not the case for the efficiency. Thus the efficiency is less prone to cross talk. Due to the development of more advanced theory in the meantime, it even surpasses the single-atom performance and reaches $(26 \pm 3)\,\%$. This already includes the slightly reduced efficiency of atoms which are not perfectly centered in the cavity mode (see also Fig. 2.4). Following the theoretical description in Sec. 3.3.1, the expected store-and-retrieve efficiency is $0.69^2 = 0.48$ at $\Delta_{ac}/2\pi = -100\,\mathrm{MHz}$. We test the photon emission efficiency by deterministically preparing one of the storage states $|F = 2, m_F = \pm 1\rangle$ and subsequent application of the STIRAP protocol. Here we indeed find the theoretically predicted efficiency of about $\eta_R = (69 \pm 2)\,\%$. From this we deduce a write-in efficiency of $\eta_W = \eta/\eta_R = (38 \pm 3)\,\%$. This lack in write-in efficiency was already observed in single-atom experiments [84]. The precise origin is still unknown. However, it is reasonable that the write-in efficiency is reduced compared to the retrieval efficiency. This is mainly due to imperfect state preparation in $|F = 1, m_F = 0\rangle$ and the necessity for mode-matching the STIRAP control pulse to the incoming complex-valued photon temporal mode, both of which can be in the 90 % range, which would already explain the observed discrepancy.

3.4.3. Coherence time

The coherence time is a very important property of any qubit memory, as it characterizes for how long the stored quantum information can be faithfully preserved. We probe the coherence time by varying the delay between the two write-ins $A_W B_W$ and the two read-outs $A_R B_R$ in the $A_W B_W A_R B_R$ access pattern. Again we use circular and linear input qubits to capture any time-dependent effect on the memory performance. Figure 3.8 shows the fidelity of atom A and atom B for a scan in the storage time. Most prominently, the fidelity for linear polarization qubits oscillates with a frequency of about 60 kHz. This is due to the energy splitting of the two atomic basis states which leads to an evolution of the superposition phase according to Eq. (3.6). The ratio of the maximally investigated storage time (1 ms) and the oscillation period (17 μs) is too big to conveniently probe the whole storage time simultaneously. Thus, multiple slices were recorded separately. Each slice is fit individually to give the local fidelity amplitude. These amplitudes are then fit with a Gaussian envelope. For linear polarization inputs, this yields a coherence time of greater than 800 μs while no decay in fidelity is observable for circular polarization

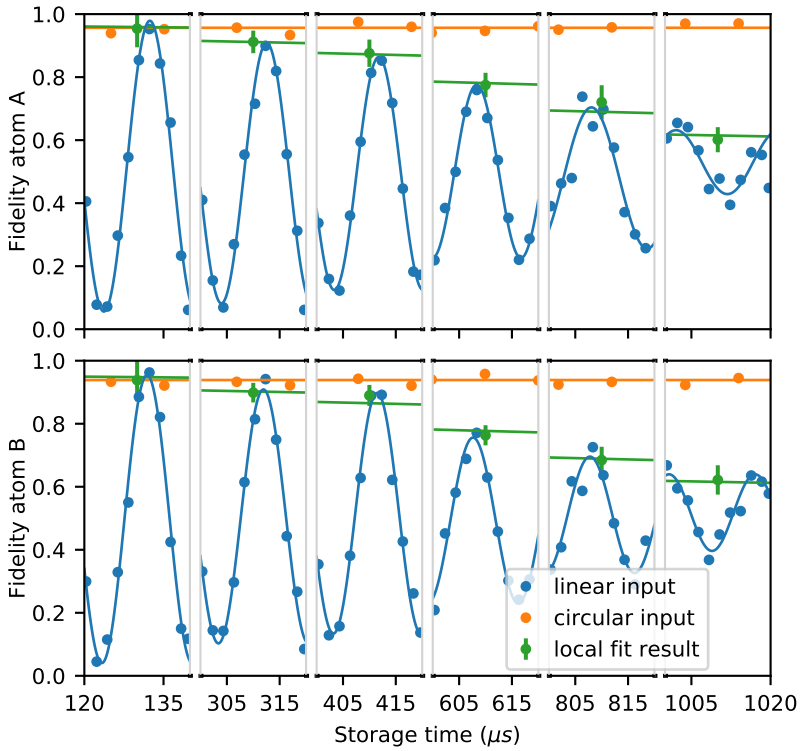

Figure 3.8.: Qubit coherence time. Fidelity of both atoms for varying storage times in the $A_W B_W A_R B_R$ access pattern. For the linear polarization input each local segment is fit individually yielding the green data points.

inputs within the examined range. As circular polarization qubits are mapped to energy eigenstates which are long-lived ground states, observing no decay in fidelity for these timescales matches expectations. However, the coherence time for linear polarization inputs is shorter compared to single-atom memory implementations where it reaches up to 1.1 ms, mostly limited by magnetic field fluctuations. This can be explained by the varying atom positions which are used in the two-atom scenario while single-atoms are always centered with respect to the cavity mode.

Figure 3.9 showcases the origin of this effect. Atoms are placed within a certain acceptance region, which covers varying intensities of the intra-cavity trap (Fig. 3.9(a)). As this intensity mostly varies along the addressing (x)-axis, we restrict our analysis to this axis. Due to the ellipticity of this trap, there is a vector light-shift (see also Sec. 3.3). This acts like an additional magnetic field on the stored qubits. We probed this effect by Zeeman-selective spectroscopy of the relevant ground states. The results for two magnitudes of the ellipticity are shown in Fig. 3.9(b). The dependence of this „magnetic field"-contribution on the magnitude of the ellipticity confirms that this is a trap-induced effect rather than just spatially varying magnetic fields. For the qubit memory, varying magnetic fields lead to a fluctuating phase-evolution and thus to decoherence. Figure 3.9(c) shows the expected coherence time for the already mentioned different ellipticities and a single-atom reference. As the effect is smaller for smaller ellipticities, we chose this setting to implement our qubit

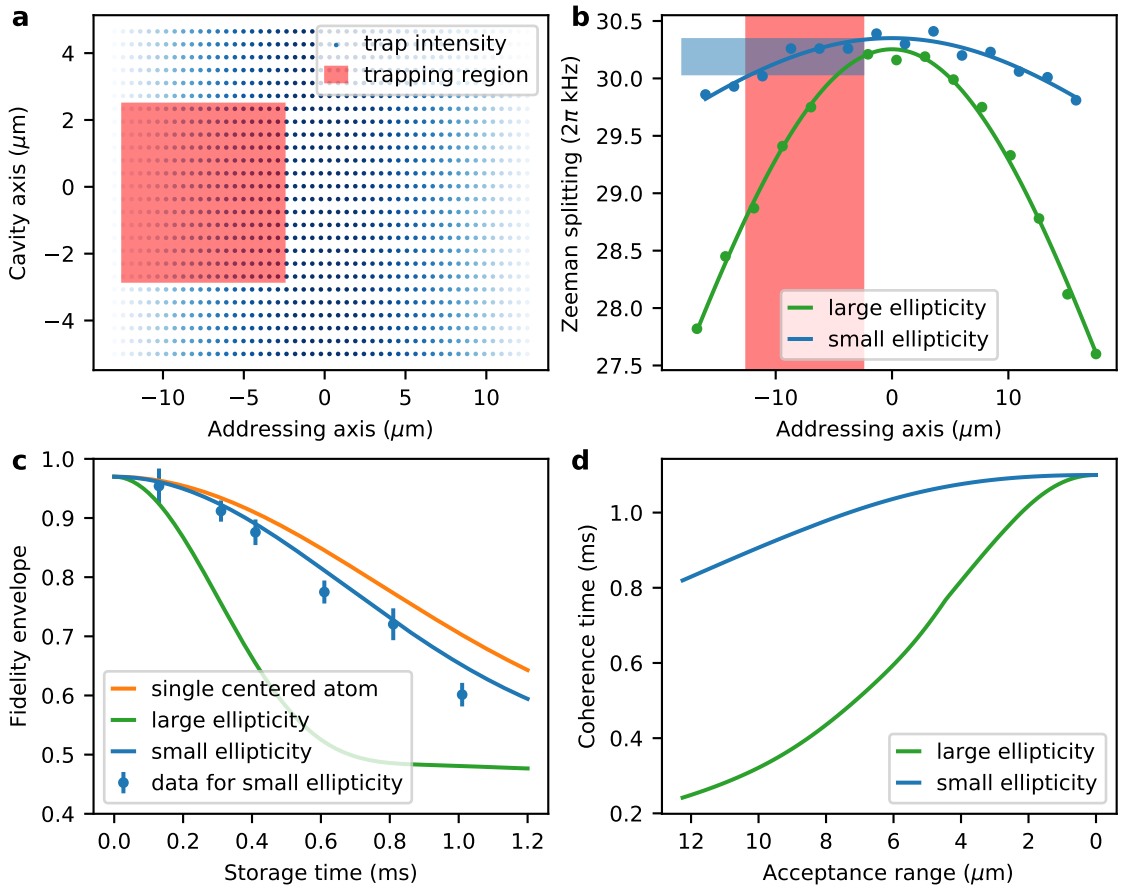

Figure 3.9.: Decoherence due to varying atom positions within intra-cavity trap. **a** Acceptance region for atomic positions within the varying intensity of the intra-cavity dipole trap. **b** Due to a vector light-shift which depends on the amount of ellipticity, there is an effective Zeeman splitting which depends on the trap intensity and thus the atom position. **c** Varying atom positions lead to varying qubit frequencies and thus decoherence. The data points are taken from the experimental results of the obtained coherence time (Fig. 3.8). **d** By reducing the acceptance range of the atom positions, the coherence time converges towards the single-atom value. Points always show experimental data while lines show theoretical estimates.

memory. Thus, Fig. 3.9(c) also shows the obtained data taken from Fig. 3.8 which nicely matches the theoretical estimation. The obvious solution to this effect would be to use perfectly linearly-polarized traps. Despite the experimental challenge of precisely tuning a polarization inside the vacuum chamber, linearly-polarized traps also result in worse atom trapping times [85]. Another solution is to have fixed atom positions. Indeed, using the introduced theoretical description, Fig. 3.9(d) shows estimates for how the coherence time improves for smaller acceptance regions of the atom positions, until it reaches the single-atom coherence time for fixed atom positions.

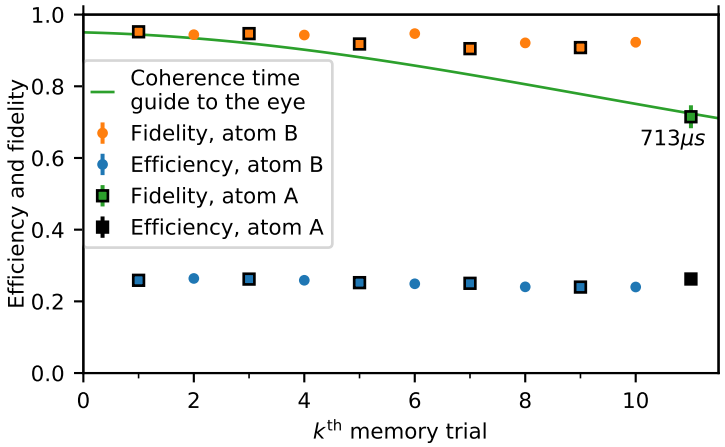

Figure 3.10.: Experimental results for the A[BB]^{k}A sequence. Depicted are k storage and retrieval attempts on atom B while atom A preserves its qubit for in total $713\,\mu$s. The decay is well-explained by the atom's limited coherence time. Circumferenced data points denote the storage of linear polarization qubits while all others are circularly polarized.

3.4.4. Storing and retrieving up to 11 photonic qubits

After characterizing the individual aspects of the qubit memory implementation, we showcase one application where up to 11 qubits are (subsequently) stored in a random-access fashion. For this we use the $A_W[B_W B_R]^k A_R$ pattern introduced in Sec. 3.3.3 with $k \leq 10$. In order to highlight the random-access nature of this memory, we re-address atom B every time it is accessed for either write-in or read-out, just as if the decision on which atom to process would not be known in advance. Thus, the time-spacing in-between write and read of the individual trials on atom B is $4\tau_L = 64\,\mu$s. The total storage time for atom A is $713\,\mu$s. We probe atom A with a linear polarization qubit as it is most sensitive to cross talk. As atom B is used multiple times, we alternate the encoded information between linear and circular polarization qubits to avoid systematic effects of residual populations.

Figure 3.10 shows the combined experimental results for atom A and atom B alongside a guide-to-the-eye for the coherence time of atom A taken from Fig. 3.8. The combined storage and retrieval fidelity of atom A after the 10 intermediate trials on atom B lies perfectly on the estimator given by the limited coherence time. And also the efficiency of atom A is the same as in a simple two-qubit protocol. This once again shows that even after 10 intermediate trials, there is still no relevant cross talk between the two memories. Note that only a fraction of these 10 attempts are successful. However, for every trial the cavity is populated and the classical control field is applied, so that even the unsuccessful trials can lead to cross talk.

Investigating atom B, the efficiency and fidelity stay high but do decay by 0.29pp and 0.44pp per trial, respectively. We attribute this to the state preparation which degrades after more trials as we do not re-initialize atom B in-between. Ideally, the qubit memory protocol is a closed loop, so that the final atomic state is the initial state again. However, there are experimental shortcomings which can lead to a different initial state. This is

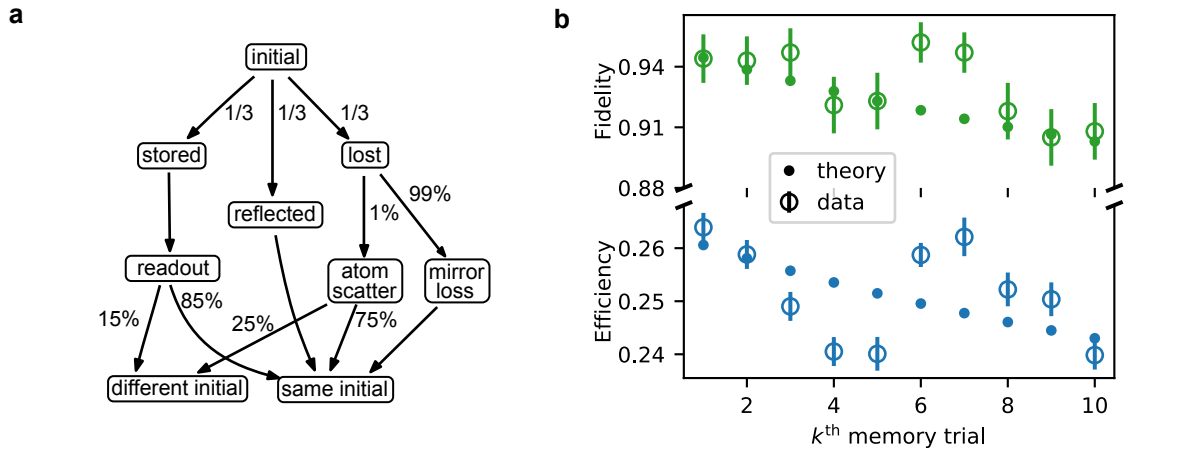

Figure 3.11.: Theory for re-initialization in A[BB]^{k}A scheme. a Markov process of possible events which either lead to the same initial state of the qubit memory protocol or a different initial state within the $F = 1$ manifold. In summary, the probability to stay within the same initial state is about 95 %. **b** Comparison of theoretically predicted and experimentally obtained fidelity and efficiency for atom B in the A[BB]^{k}A scheme.

further analyzed in Fig. 3.11. Part (a) shows how the probability evolves for staying in the initial state $|F = 1, m_F = 0\rangle$ or evolving to different initial states $|F = 1, m_F = \pm 1\rangle$ which would still be usable for a memory but with reduced fidelity and efficiency. All numbers are taken from independent measurements of theoretical estimations for weak coherent pulse inputs. The main effect leading to a different initial state is the very left branch, which describes the successful storage of the input, but includes scattering to the wrong initial state upon creation of the readout photon. Assuming the correct storage state was populated, i.e. $|F = 2, m_F = \pm 1\rangle$, the STIRAP process should lead to $|F = 1, m_F = 0\rangle$. However it can also scatter the population which can lead to $|F = 1, m_F = \pm 1\rangle$. The resulting photons are π-polarized and thus not supported by the cavity. Thus they do not lead to a decrease in fidelity for the current trial but still result in the wrong initial state for the next one. The impact of this worse state preparation is depicted in part (b) which compares the theoretically expected decay in fidelity and efficiency with the experimentally observed one. While there are fluctuations on the experimental data, there is an overall agreement between theory and experiment.

3.5. Summary and outlook

We have demonstrated a random-access two-qubits memory with a coherence time approaching 1 ms and a combined write-read efficiency of 26 %. We have shown that it can be used for handling of at least 11 qubits with negligible cross talk between the two memories. For future implementations, electro-optical deflectors would reduce the switching time between memories from currently 40 μs down to 2 μs. This would enable many more random accesses during the coherence time of the memory. These accesses can either be used in the two-atom version demonstrated here, or with more atoms as has been already

discussed in Sec. 2.6. For this transition, further decreasing the cross talk between the different memories would be beneficial. For this a larger atom-photon interaction rate g would increase the coherent efficiency of the storage-and-retrieval process while the off-resonant scattering of cavity population can be further decreased by going to even larger atom-cavity detunings. A larger g would also increase the probability to end up in the correct initial state after a memory trial. As an alternative, atom-selective state preparation would ensure high-fidelity and high-efficiency operations independent of the earlier utilization of the individual memory. Finally, atom-selective stimulated transfers would enable to transfer individual atoms to decoherence-free substates which would enable larger than 100 ms coherence times [63]. Alternatives for extending the coherence times without atom-selective transfers will be discussed in the context of Ch. 4, before Ch. 5 describes how we can extend the qubit register demonstrated here to build a quantum repeater.

4. Extending coherence with dynamical decoupling

Extending the coherence time of qubit memories is still one of the greatest challenges for scaling quantum technologies to larger, fully-coherent computers on the one side and extending quantum communication distances in quantum repeater based networks on the other.

There are mainly four options for extending coherence time. First, shielding of the sensitive qubit carriers either by external equipment (e.g. mu-metal) [113, 114] or by outer-lying electronic orbitals of the same matter qubit carrier [115]. While both approaches are promising, they have to be considered at the initial setup of an experiment. In addition, they can only protect from externally applied noise and cannot compensate for atomic temperature or trap potential fluctuations to only name two possible internal noise sources. Second, the qubit can be transferred to a decoherence-protected subspace, in which the sensitivity to noise is intrinsically reduced [63, 116, 117]. This again does not necessarily protect from internal fluctuations and additionally might only be achievable on the cost of an overall reduction in fidelity and a significant experimental overhead [63]. In the third option, the qubit fluctuations due to internal and external noise are averaged out by manipulating the qubit so that it constantly rephases to its initial state. This approach is called dynamical decoupling, and is heavily used in solid state systems [105, 118–120]. The fourth option is currently far from being experimentally in reach for our system, which is using error-correcting codes for encoding a logical qubit into multiple physical qubits which can detect and correct for occurring bit and phase flips [121–125].

Here we use the third option to dynamically decouple the magnetic-field sensitive qubits stored in Zeeman states of the same hyperfine manifold in ^{87}Rb. This will increase the coherence time for qubit memories like the one presented in Ch. 3 and contribute to enabling the quantum repeater demonstration presented in Ch. 5.

4.1. Theory

The idea of dynamical decoupling started in 1950, with the observation of spin-rephasings in nuclear magnetic resonance experiments [126]. Its working principle is shown in Fig. 4.1 and is based on the constant coupling to a dephasing bath which can be reversed by applying a σ_x gate at half time of the coupling duration. In an ideal picture, the applied gate has no imperfections, has zero duration and does not alter the decoupling bath. These ideal-world assumptions can be lifted, at least partially, by the extension to composite pulse-sequences. By repeating these sequences again and again, the spin ensemble can be

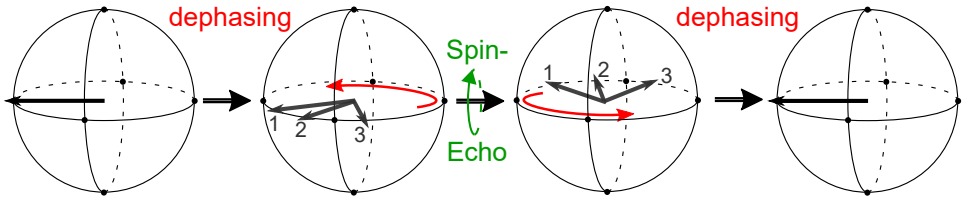

Figure 4.1.: Spin-echo illustration. The constant coupling to a dephasing bath can be reversed by application of a spin-echo (σ_x gate) at half time of the coupling duration, so that the initial state is restored at the end of the process.

constantly decoupled from the dephasing bath, which was labeled dynamical decoupling [127]. The earliest and arguably easiest of these sequences, named after their inventors Carr-Purcell (CP) and Meiboom-Gill (CPMG), were designed for specific input qubits [128, 129]. Here, σ_x gates are repeated with a constant time interval, which determines the timescale on which fluctuations can be compensated. Later on, sequences such as XY4 [130] were developed where a combination of σ_x and σ_y gates decouples all possible input states and on top of that is more resilient against pulse-area imperfections.

Nevertheless, having fast and almost error-free gates is still an important prerequisite for efficient dynamical decoupling and probably most often their absence is the reason why alternative approaches have to be considered. In the next sections, we will thus look at how to perform high-fidelity gates on our qubit basis states.

4.1.1. Intra-hyperfine $\Delta m_F = 1$ transfer

The goal is to drive transitions between the energy eigenstates $|\uparrow_z\rangle = |F = 1, m_F = 1\rangle$ and $|\downarrow_z\rangle = |F = 1, m_F = -1\rangle$ in a far-detuned Raman configuration, so that off-resonant scattering is minimized. Due to destructive interference of transitions via multiple excited states, $\Delta m_F = 2$ transitions can not be driven far-detuned, but only with the virtual excited state having a different sign in detuning with respect to the different excited state manifolds, effectively limiting the single-photon detuning to only 400 MHz [63, 131]. Here we bypass this limitation by doing a multi-step Raman transition in which each individual step is only $\Delta m_F = 1$. The disadvantage of having multiple steps which need to be timed is mitigated by performing both steps simultaneously. Another advantage to our scheme is that the qubit stays in the $|F = 1\rangle$ manifold the whole time, thus avoiding decoherence due to differential trap frequencies for $|F = 1\rangle$ and $|F = 2\rangle$ [63].

First we will derive the Hamilton for the application of π-pulses on the atomic qubits. The beam configuration is shown in Fig. 4.2. The atomic basis states are ($|1, -1\rangle$, $|1,0\rangle$, $|1,1\rangle$, $|2', -2\rangle$, $|2', -1\rangle$, $|2',0\rangle$, $|2',1\rangle$, $|2',2\rangle$) where the excited states are part of the $|5^2P_{1/2}\rangle$ manifold. Two light fields are applied, one $\sigma^{\pm}$-polarized with frequency ω_y and phase ϕ_y, and one π-polarized with frequency ω_x and phase ϕ_x.

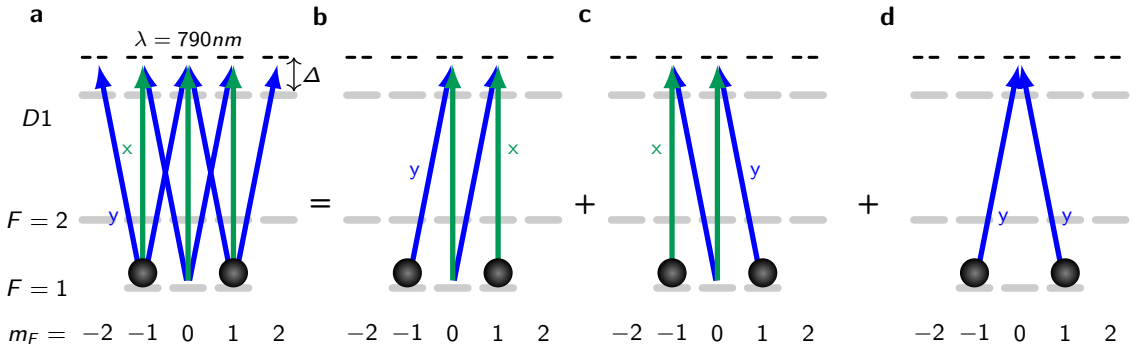

Figure 4.2.: Intra-hyperfine Raman configuration A combination of $\sigma^{\pm}$ (y, blue) and π-polarized (x, green) beams is used to drive the Raman transition. The application of these light fields results in the driving of multiple transitions (b-d), of which only (b) is desired. The other two processes can be tuned out of two-photon resonance by application of a Zeeman splitting. The illustrated equation is not to be understood strictly mathematical, but rather indicates the different possible transitions.

The following Hamilton describes the relevant energy offsets and driving interactions:

$$\hat{H} = \frac{\hbar}{2} \begin{bmatrix} 0 & 0 & 0 & \Omega_{14}e^{-i\omega_y t - i\phi_y} & \Omega_{15}e^{-i\omega_x t - i\phi_x} & \Omega_{16}e^{-i\omega_y t - i\phi_y} & 0 & 0 \\ & 2\delta_L & 0 & 0 & \Omega_{25}e^{-i\omega_y t - i\phi_y} & \Omega_{26}e^{-i\omega_x t - i\phi_x} & \Omega_{27}e^{-i\omega_y t - i\phi_y} & 0 \\ & & 4\delta_L & 0 & 0 & \Omega_{36}e^{-i\omega_y t - i\phi_y} & \Omega_{37}e^{-i\omega_x t - i\phi_x} & \Omega_{38}e^{-i\omega_y t - i\phi_y} \\ & & & 2E_e/\hbar & 0 & 0 & 0 & 0 \\ & & & & 2E_e/\hbar & 0 & 0 & 0 \\ & & & & & 2E_e/\hbar & 0 & 0 \\ & c.c. & & & & & 2E_e/\hbar & 0 \\ & & & & & & & 2E_e/\hbar \end{bmatrix}, \tag{4.1}$$

where δ_L is the magnetic-field induced Larmor frequency, Ω_{ij} is the Rabi frequency between state i and j and E_e is the energy level of the excited states.

This Hamilton describes multiple simultaneous processes which run in parallel (Figs. (b-d)). We will choose the detuning of the two frequencies ω_x and ω_y so that process (b) will be in two-photon resonance while processes (c&d) will not be. It will not be possible to transfer Eq. (4.1) to a time-independent interaction Hamilton, as it is not possible to go to a rotating frame for all processes simultaneously. We choose the constant Hamilton

$H_0 = \hbar\mathrm{diag}(-2\omega_y, -\omega_y-\omega_x, -2\omega_x, -\omega_y, -2\omega_y+\omega_x, -\omega_y, -\omega_x, \omega_y-2\omega_x)$ which allows to use the unitary transfer operator $\hat{U} = e^{iH_0 t/\hbar}$ to switch to an interaction Hamilton:

$$\hat{H_I} = U^\dagger H U - H_0 =$$

$$\frac{\hbar}{2}\begin{bmatrix} 2(\omega_y-\omega_x) & 0 & 0 & \Omega_{14}e^{-i\phi_y} & \Omega_{15}e^{-i\phi_x} \\ & 2\delta_L & 0 & 0 & \Omega_{25}e^{-i(\phi_y+2t(\omega_y-\omega_x))} \\ & & 4\delta_L-2(\omega_y-\omega_x) & 0 & 0 \\ & & & 2(E/\hbar-\omega_x) & 0 \\ & & & & 2(E/\hbar+\omega_y-2\omega_x) \\ & & & & \\ & & & & \\ & c.c. & & & \end{bmatrix} \tag{4.2}$$

$$\begin{bmatrix} \Omega_{16}e^{-i\phi_y} & 0 & 0 \\ \Omega_{26}e^{-\phi_x} & \Omega_{27}e^{-\phi_y} & 0 \\ \Omega_{36}e^{-i(\phi_y+2t(\omega_y-\omega_x))} & \Omega_{37}e^{-\phi_x} & \Omega_{38}e^{-\phi_y} \\ 0 & 0 & 0 \\ 0 & 0 & 0 \\ 2(E/\hbar-\omega_x) & 0 & 0 \\ & 2(E/\hbar-\omega_y) & 0 \\ & & 2(E/\hbar-2\omega_y+\omega_x) \end{bmatrix},$$

where the diagonal elements where shifted by $-\hbar(\omega_y+\omega_x)$. Note that this is time-independent except of the interaction terms H_{25},H_{36} which drive the second process (c) off-resonantly.

As we will set $\Delta \approx 2\,\mathrm{THz}$, $(E/\hbar-\omega_y) \approx (E/\hbar-\omega_x) = \Delta \gg \Omega$ and we can apply adiabatic elimination to get a compressed interaction Hamilton for the first three states:

$$\hat{H_I} = \frac{\hbar}{4}$$

$$\begin{bmatrix} \frac{\Omega_{15}^2}{\Delta-\delta_T} + \frac{\Omega_{14}^2+\Omega_{16}^2}{\Delta} & e^{-i(\phi_x-\phi_y)}\left(\frac{e^{-i2\delta_T t}\Omega_{15}\Omega_{25}}{-\Delta+\delta_T} + \frac{\Omega_{16}\Omega_{26}}{\Delta}\right) & \frac{e^{-i2\delta_T t}\Omega_{16}\Omega_{36}}{\Delta} \\ & \frac{-\delta_T(\Omega_{26}^2+\Omega_{27}^2)}{\Delta(\Delta-\delta_T)} + \frac{\Omega_{25}^2+\Omega_{26}^2+\Omega_{27}^2}{\Delta-\delta_T} & \frac{e^{i(\phi_y-\phi_x-2\delta_T t)}\Omega_{26}\Omega_{36}+e^{i(\phi_x-\phi_y)}\Omega_{27}\Omega_{37}}{\Delta} \\ c.c. & & \frac{\Omega_{38}^2}{\Delta+\delta_T} + \frac{\Omega_{36}^2+\Omega_{37}^2}{\Delta} \end{bmatrix}. \tag{4.3}$$

Here, $\omega_x - \omega_y = \delta_T$ is the two-photon-detuning which we tuned to compensate for the non-zero diagonal elements ($\delta_T = -\delta_L$). This can be further simplified by $\Delta \pm \delta_T \approx \Delta$ and $\delta_T/\Delta \approx 0$ as $\Delta \gg \delta_T$, and $\phi_y - \phi_x = \phi$:

$$\hat{H_I} = \frac{\hbar}{4\Delta}$$

$$\begin{bmatrix} \Omega_{14}^2+\Omega_{15}^2+\Omega_{16}^2 & -e^{-i(2\delta_L t-\phi)}\Omega_{15}\Omega_{25} + e^{i\phi}\Omega_{16}\Omega_{26} & e^{-i2\delta_L t}\Omega_{16}\Omega_{36} \\ & \Omega_{25}^2+\Omega_{26}^2+\Omega_{27}^2 & e^{i(\phi-2\delta_L t)}\Omega_{26}\Omega_{36} + e^{-i\phi}\Omega_{27}\Omega_{37} \\ c.c. & & \Omega_{35}^2+\Omega_{36}^2+\Omega_{37}^2 \end{bmatrix}. \tag{4.4}$$

If the beams are far-detuned from any excited state manifold, then $\Omega_{14}^2 + \Omega_{15}^2 + \Omega_{16}^2 = \Omega_{25}^2 + \Omega_{26}^2 + \Omega_{27}^2 = \Omega_{35}^2 + \Omega_{36}^2 + \Omega_{37}^2$ which guarantees two-photon resonance. In order to solve the time-dependent Hamilton analytically, we neglect the time-dependent terms in Eq. (4.4). This can be justified, if all Rabi frequencies are chosen so that $\Omega_{ij} \ll 2\delta_L \approx 2\pi \times 100\,\mathrm{kHz}$. This is a significant limitation in the Rabi frequencies, which we were also able to observe experimentally. If the Rabi frequencies are chosen too large with respect to the Zeeman splitting, the different Raman transitions (Fig. 4.2) interfere and lead to unexpected behavior which, for example, made it impossible to concatenate multiple $\pi-$pulses with arbitrary in-between waiting times.

After neglecting the oscillation terms in Eq. (4.4) and adjusting the different Rabi frequencies and Δ to get full population inversion at $\Omega t = \pi$, we get

$$\begin{aligned} \psi' &= R\psi, \text{with} \\ R = R(\Omega t, \phi) &= \begin{bmatrix} \cos^2 \Omega t/2 & \frac{-i}{\sqrt{2}} e^{i\phi} \sin \Omega t & -e^{2i\phi} \sin^2 \Omega t/2 \\ \frac{-i}{\sqrt{2}} e^{-i\phi} \sin \Omega t & \cos \Omega t & \frac{-i}{\sqrt{2}} e^{i\phi} \sin \Omega t \\ -e^{-2i\phi} \sin^2 \Omega t/2 & \frac{-i}{\sqrt{2}} e^{-i\phi} \sin \Omega t & \cos^2 \Omega t/2 \end{bmatrix}. \end{aligned} \tag{4.5}$$

Thus, most prominently:

$$R(\Omega t = \pi) = \begin{bmatrix} 0 & 0 & -e^{2i\phi} \\ 0 & -1 & 0 \\ -e^{-2i\phi} & 0 & 0 \end{bmatrix}, R(\Omega t = 2\pi) = \begin{bmatrix} 1 & 0 & 0 \\ 0 & 1 & 0 \\ 0 & 0 & 1 \end{bmatrix}. \tag{4.6}$$

This shows that every π-pulse adds a phase of 4ϕ to the relative phase of $|F = 1, m_F = 1\rangle$ and $|F = 1, m_F = -1\rangle$ while 2π-pulses give the initial state again.

4.2. Experimental implementation

The Raman setup necessary for driving these intra-hyperfine transitions is in-fact very similar to the one used in the *QGate* sister experiment where it is used for applying single-qubit gates in the $(|F = 1, m_F = 1\rangle, |F = 2, m_F = 2\rangle)$ basis [131]. For this Raman interaction a beam with two orthogonal polarizations is necessary. To this end, we modified beam (5) in Fig. 2.3 from a single-polarization configuration to support π as well as $\sigma^{\pm}$ polarizations. We implemented two major deviations compared to our sister experiment. First, we chose a significantly larger single-photon detuning Δ in order to reduce off-resonant scattering for the application of many π-pulses and to reduce AC-Stark shifts induced by the Raman beams. Second and more importantly, we had to stabilize the relative phase of the two Raman beams (ϕ above). The difference to our sister experiment is, that in their case the initial qubit is defined by the Raman pair itself. Thus, any arbitrary phase, as long as it is constant for one experimental run (1 ms), will not affect the results. In contrast, the qubits in qubit memories are defined outside, without any known reference to the Raman phase ϕ. Thus, it was necessary to stabilize ϕ to a given value (we chose $\phi = 0$) for the complete duration of the data acquisition (days).

4.2.1. Raman configuration

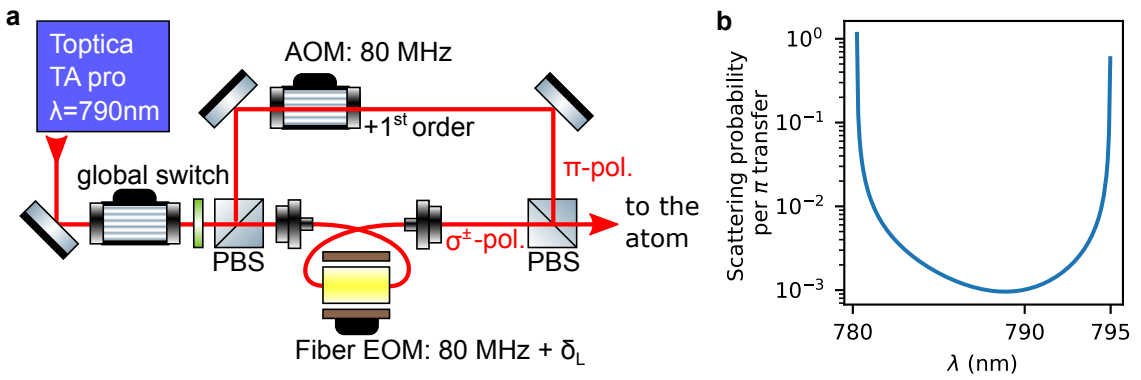

Figure 4.3.: Setup for far-detuned Raman transitions. **a** Optical setup including the relevant frequencies for having a combination of π- and $\sigma^{\pm}$-polarized beams on the atoms which are in two-photon-resonance. **b** Scattering probability per π-pulse as a function of single-photon wavelength, indicating the optimal operation point close to $\lambda = 790\,\mathrm{nm}$.

Figure 4.3(a) shows the optical setup implemented in the laboratory for driving the intra-hyperfine $\Delta m_F = 1$ transfers described above. For historic reasons, a combination of a phase-modulation fiber electro-optical modulator (PM-EOM) and a free-space AOM is used instead of just two AOMs. This configuration also allows to drive the inter-hyperfine transitions mentioned earlier for the *Qgate* sister experiment, for which the EOM needs to be set to $\Delta_{hf} + 80\,\mathrm{MHz}$. Both beams are power-stabilized via photo-diodes on the cavity table and a lab-built stabilization circuit which acts on the global switch for the EOM-path and on the AOM for the AOM-path.

In Fig. 4.3(b), the off-resonant scattering probability is shown for a range of single-photon detunings. The optimum working point is close to $\lambda = 790\,\mathrm{nm}$ which can intuitively be understood as the average of the D_1- and the D_2-line detunings, weighted with their respective Clebsch-Gordan coefficients ($cg^2_{D2}/cg^2_{D1} = 2$). Note that the overall scale of the scattering rate is challenging to estimate, as it depends on the imbalance in power between π-light and $\sigma^{\pm}$-light as well as the modulation depths of the EOM. Both effects can lead to variations on the overall scattering rate by an order of magnitude.

4.2.2. Phase stabilization

As motivated above, the relative phase of the two Raman beams has to be stabilized. To this end, we implemented a phase-locked-loop (PLL). The schematic for the phase stabilization setup is depicted in Fig. 4.4. Starting from the first polarizing beam splitter (PBS), the Mach-Zehnder type beam configuration together with the two modes of a 10 m polarization maintaining (PM)-fiber form an interferometer which defines ϕ. After passing the atoms, this interferometer is made to interfere by overlapping the two polarization modes on a polarizer. This signal can then be used for feedback, which we apply in a stabilization period during cooling of the atoms, as described below:

Stabilization mode: The idea is that there is a stabilization period, in which the light

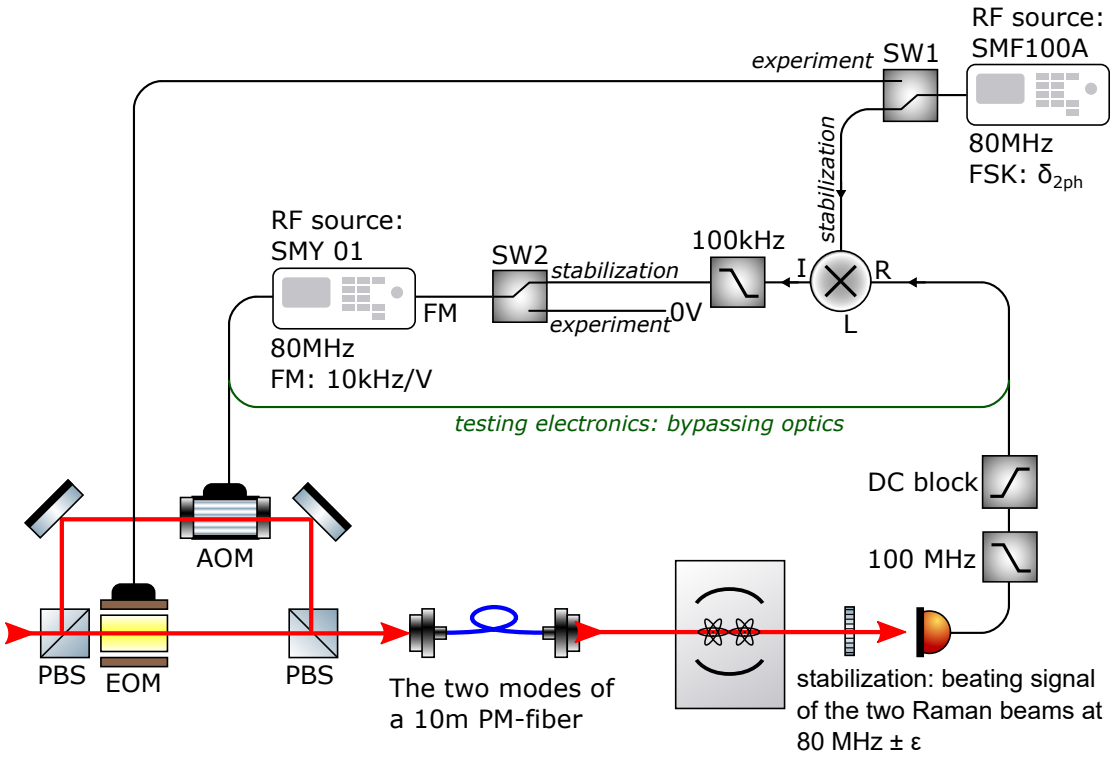

Figure 4.4.: Optical and electronic setup for phase stabilization. The two arms of the Mach-Zehnder interferometer and the two modes of a 10 m polarization maintaining (PM) fiber form an interferometer whose phase has to be stabilized. A phase-locked-loop (PLL) is implemented which frequency-modulates (FM) the AOM to catch up any phase difference. The two switches SW1, SW2 and the frequency-shift-keying (FSK) of the RF source are used for switching between a stabilization mode and an experimental mode which are explained in the text.

is on, but it is not in two-photon resonance so that it is dark for the atom. The EOM is turned off and the AOM is frequency-modulated (FM) so that it catches up any phase difference. This effectively implements a PLL. Thus, in this stabilization mode, the AOM frequency is $(80 \pm \epsilon)\,\mathrm{MHz}$, where ϵ is the difference in frequency necessary for catching up. At the same time, the EOM driver is set to 80 MHz and not directed to the EOM (SW1), but to the demodulation of the AOM-EOM(off) beating which is used for the phase detection of the PLL.

Experiment mode: During the experiment, the AOM and EOM are driven so that the resulting light is in two-photon resonance with the atomic transition. The advantage of the PLL is, that its feedback is 0 as soon as it is in resonance, so that no sample-and-hold is necessary for switching between stabilization mode and experiment mode. While the AOM frequency modulation is made 0 by using an external switch (SW2), the EOM frequency is set via a phase-stable frequency-shift-keying (FSK) to the aforementioned two-photon resonance ($\delta_{2\mathrm{ph}} = \delta_L$). As the AOM/EOM beating accumulates a phase during this period of different frequency of the EOM, the length of the FSK needs to be tuned so that $\delta_{2\mathrm{ph}} \times \tau_{FSK}/2\pi = n$, where n is an integer number. The exact driving time of the atom for e.g. π-pulses is defined via the application of the RF power to the EOM, which

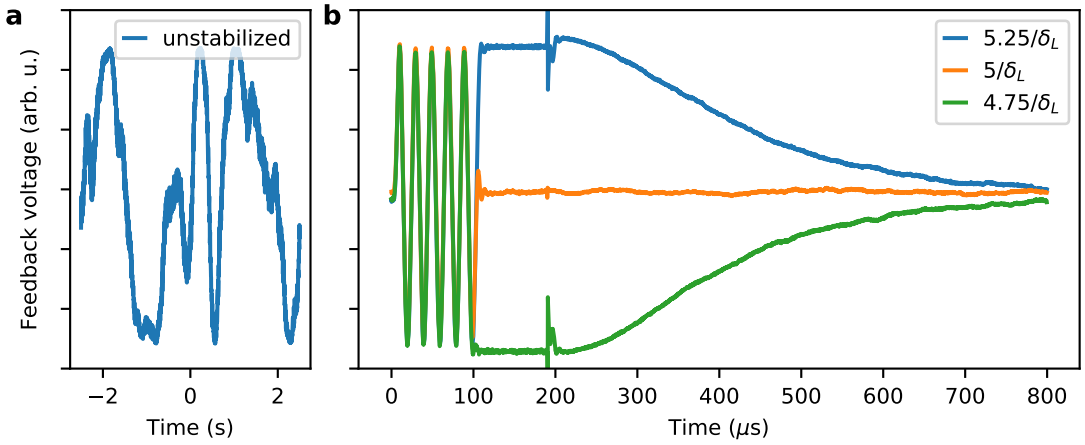

Figure 4.5.: Phase evolution of the Raman setup. **a** PLL feedback voltage as an indicator for the phase evolution without active feedback. Fluctuations on a few hundred *ms* timescales are visible. **b** Phase evolution for three different FSK pulse durations. The FSK imprints a frequency difference which is visible as oscillations in phase (0 μs to 100 μs). Afterwards (100 μs to 200 μs), the FSK is turned off and the phase stays constant at its last value of the oscillation, which can be used for setting an arbitrary phase for the Raman process. After 200 μs, the feedback is turned on which stabilizes the phase to 0 on a timescale of 200 μs.

just needs to be within the FSK period.

Testing the electronics: In order to test the protocol described above, we can bypass the optics generating the phase drift and directly connect the AOM driver to the demodulation via the EOM. In this way we can verify that the FSK does not generate an additional phase and also verify that the two microwave sources have the same frequency.

Figure 4.5 shows a comparison between unstabilized (a) and stabilized (b) phase-evolution, as well as the effect of the application of the FSK which results in fast oscillations of the phase and its return to the initial value if the length of the FSK period is tuned correctly (integer multiple of $1/\delta_L$). From this we conclude phase-stability over a duration of at least 10 ms when there is no compensation, i.e. in experimental mode, and a remaining root-mean-square fluctuation of the phase of 0.9 deg.

4.2.3. Choice of dynamical decoupling rotation axis

For the repeater scheme which will be discussed in Ch. 5, the stored qubits must be in one of four states independent of the number of DD pulses. Obviously, it can not be the same state every time, as in this case there would be no decoupling. For qubits prepared in one of the energy eigenstates, the qubit has to be flipped after every DD pulse as this is essential for decoupling from m_F-dependent noise. As it is known how many DD pulses were applied, this flip can be compensated in post-processing. For qubits prepared in an equal superposition state, the impact of a DD pulse depends on the relative phase of the DD-rotation axis in the Bloch sphere and the phase of the qubit. The DD-rotation axis can be tuned by adjusting the relative phase of the two Raman beams ϕ, which we tune by first stabilizing it to 0 and then applying a controlled frequency difference for a specific

duration. Another peculiarity of the repeater is that it uses a four-state protocol, i.e. the qubit is always prepared in one of the four states $\{|\uparrow_z\rangle, |\downarrow_z\rangle, |\uparrow_x\rangle, |\downarrow_x\rangle\}$. Thus, there are only two possible superposition qubits which are always orthogonal. This allows to tune ϕ to have the DD-rotation axis along this qubit axis, which results in no noticeable qubit alteration although $|\uparrow_z\rangle$ and $|\downarrow_z\rangle$ are being exchanged (Fig. 4.6). Taking the rotation operator from Eq. (4.6) this reads:

$$\begin{bmatrix} 0 & 0 & e^{2i\phi} \\ & 1 & 0 \\ c.c & & 0 \end{bmatrix} \cdot \frac{1}{\sqrt{2}} \begin{bmatrix} 1 \\ 0 \\ \pm e^{i\theta} \end{bmatrix} = \frac{1}{\sqrt{2}} \begin{bmatrix} \pm e^{i(\theta-2\phi)} \\ 0 \\ e^{2i\phi} \end{bmatrix} = \frac{\pm 1}{\sqrt{2}} \begin{bmatrix} 1 \\ 0 \\ \pm e^{i\theta} \end{bmatrix} \text{ for } 2\phi = \theta, \tag{4.7}$$

where θ defines the phase of the initial equal superposition qubit and $\pm$ accounts for the possibility of $|\uparrow_x\rangle$ and $|\downarrow_x\rangle$. Thus, by choosing $2\phi = \theta$, the initial qubit is preserved up to global phases. This is reminiscent of the difference of CPMG and CP, where for the first one the qubit is aligned with the rotation axis while for the second one it is orthogonal while the actual pulse-sequence is the same.

Note that this is only possible because of the limited number of possible qubits in the repeater protocol, which means the decoupling can be optimized for just those states. For a general qubit memory, every possible superposition and energy eigenstate has to be decoupled from noise, for which more complicated decoupling sequences were invented and are still under active investigations [120, 132]. In contrast, here the energy eigenstates $|\uparrow_z\rangle, |\downarrow_z\rangle$ are decoherence-free [63] so that there are only $|\uparrow_x\rangle, |\downarrow_x\rangle$ left which have to be decoupled. This simplifies the sequence significantly on the cost of additional benefits of these more complicated DD-sequences, such as stability against Raman pulse imperfections.

To summarize, we perform DD π-pulses always around the same axis which is aligned with the qubits $(|\uparrow_x\rangle, |\downarrow_x\rangle)$, similar to a concatenation of spin-echo pulses. This results in no change for $(|\uparrow_x\rangle, |\downarrow_x\rangle)$ and in bit-flips for $(|\uparrow_z\rangle, |\downarrow_z\rangle)$.

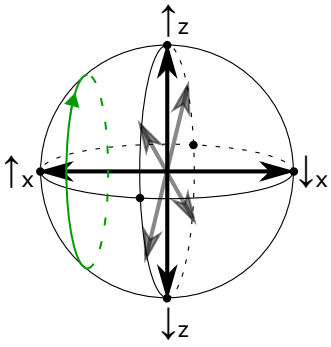

Figure 4.6.: Dynamical decoupling rotation axis. $(|\uparrow_x\rangle, |\downarrow_x\rangle)$ stay the same when applying DD $\pi-$pulses (green arrow), while $(|\uparrow_z\rangle, |\downarrow_z\rangle)$ undergo bit flips.

4.3. Experimental results

4.3.1. Coherent population transfers

First we test the performance of the coherent population transfer within the $|F = 1\rangle$ manifold. To this end, we perform a single-atom photon-photon entanglement experiment similar to Wilk et al. [58] (see App. B).

Assuming the first photon detection projects the atom onto $|F = 1, m_F = 1\rangle$ and using

Eq. (4.5) for describing the driving dynamics, the fidelity of the second photon is given by:

$$\mathcal{F} = \frac{\eta_G P_1 + 0.5\eta_B P_0}{\eta_G P_1 + \eta_G P_{-1} + \eta_B P_0} = \frac{4\eta_G \cos^4(\Omega t/2) + \eta_B \sin^2(\Omega t)}{\eta_B + 3\eta_G + (\eta_G - \eta_B)\cos(2\Omega t)}, \tag{4.8}$$

where $P_i(t)$ are the probabilities of the qubit being in $|F = 1, m_F = i\rangle$ which follow Eq. (4.5). η_G (η_B) is the read-out efficiency for $|F = 1, m_F = \pm 1\rangle$ ($|F = 1, m_F = 0\rangle$), t is the pulse duration of the Raman pulse and Ω is its Rabi frequency. The motivation for this formula is, that population in $|F = 1, m_F = 0\rangle$ results in a fidelity of 0.5 while population in $|F = 1, m_F = 1\rangle$ (the initial state), gives ideally a fidelity of 1.

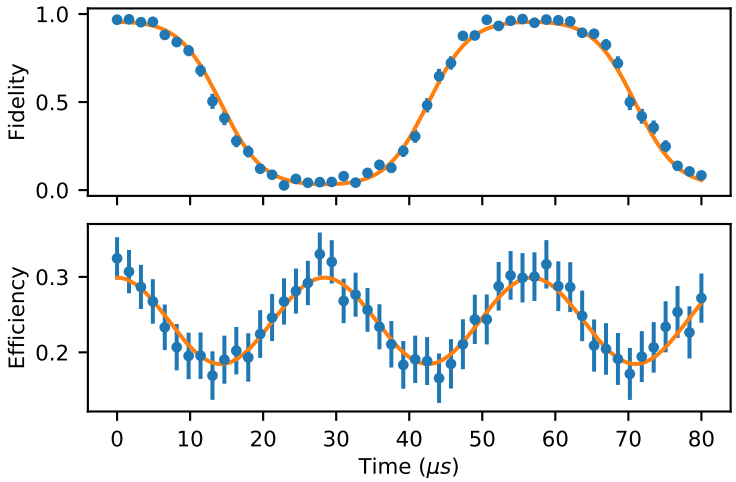

Figure 4.7.: Coherent population transfer in F=1. Fidelity and efficiency for different pulse durations including fits to the combined fidelity/efficiency data sets. The deviation from a *sin*-curve for the fidelity is due to the multi-step process described in the main text.

Figure 4.7 shows the fidelity between the first and the second photon in the circular detection basis, i.e. the case described by Eq. (4.8). The corresponding fit matches nicely and yields a Rabi frequency of $\Omega/2\pi = 17.6\,\mathrm{kHz}$. Additionally, the same figure shows the oscillation in readout efficiency, with maxima whenever the qubit is in $|F = 1, m_F = \pm 1\rangle$, owing to the difference in η_G and η_B.

4.3.2. Coherence time

The main decoherence mechanisms for the employed qubit states are magnetic field fluctuations and varying virtual magnetic fields due to circular polarization components in the optical dipole traps [63]. Both effects should be compensable with dynamical decoupling, if the pulse separation and duration is significantly smaller than the frequency of the noise.

The easiest decoupling sequence is the application of a single π-pulse in the middle of the storage time, called spin-echo after Hahn's pioneering experiments [126]. This technique can already compensate for slowly-varying drifts while oscillations which are fast compared to the total storage time will still decohere the qubit.

In the next step, many π-pulses are applied so that faster drifts can be compensated. In the sequence used for the quantum repeater (Ch. 5), there is a window of $30\,\mu$s every $100\,\mu$s for applying dynamical decoupling pulses (the motivation of this can be found in the respective chapter).

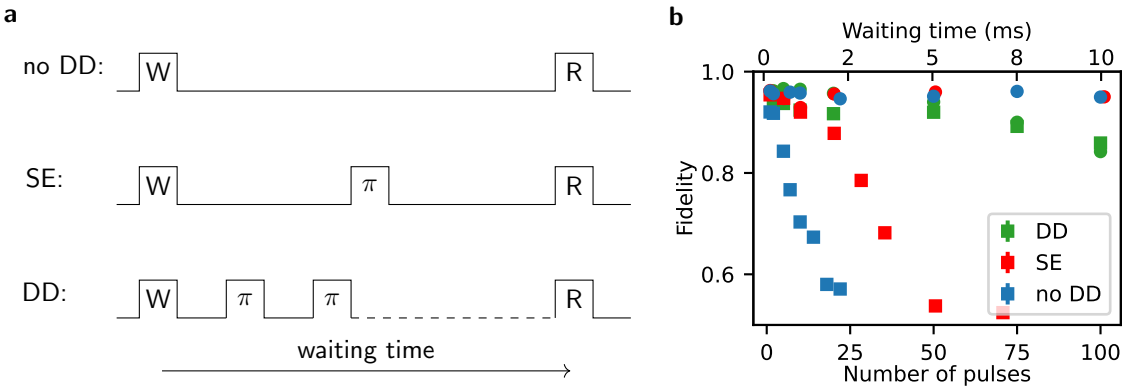

Figure 4.8.: Comparison of coherence times. **a** Sequence for three different configurations, namely without any decoupling (no DD), only with a single π-pulse in the middle of the waiting time (SE) and with many π-pulses separated by $99\,\mu$s. Each π-pulse takes $28\,\mu$s. **b** Fidelity versus number of pulses for the different sequences. Square dots denote qubits in the superposition basis and circular dots denote qubits in the energy eigenbasis.

An overview of the three different investigated sequences is shown in Fig. 4.8(a), where the sequence with no DD pulses serves as a reference. Figure 4.8(b) depicts the experimental results for the different sequences. There are two main observations. First, the $\mathcal{F} = 0.66$ coherence time can be improved from about $1.2\,$ms without decoupling, to $3.8\,$ms with a single spin-echo pulse and to $23\,$ms for the final decoupling sequence. Due to limitations of the FPGA control electronics, only 100 pulses could be applied so that the given fidelity is only an estimate. Note that the coherence time without decoupling is different compared to Ch. 3, as in the meantime, a feed-forward compensation for magnetic field fluctuations at $f = 50\,$Hz and $f = 150\,$Hz was implemented. The second main message becomes apparent when comparing results for the superposition basis (squares) and for the energy eigenbasis (circles). For the sequence without decoupling and for the one with a single pulse, the fidelity for energy eigenstates stays constant over the investigated range as is expected for long-lived atomic ground states [63]. In contrast, the fidelity for the DD sequence decays the same way as the fidelity for the qubits in the superposition basis. This clearly indicates that the major decay mechanism is not a remaining fast fluctuation, but most probably infidelities of the applied DD pulses.

In theory, qubits aligned with the rotation axis (CPMG, $|\uparrow_x\rangle, |\downarrow_x\rangle$) are not sensitive to imperfections in the pulse area of the DD pulses themselves, although the decoupling performance degrades of course. In contrast, qubits perpendicular to the rotation axis (CP, $|\uparrow_z\rangle, |\downarrow_z\rangle$) are maximally sensitive. In our case, however, the situation is different as imperfect transfers do not leave ($|\uparrow_x\rangle, |\downarrow_x\rangle$) unscathed because the qubits can end up in $|F = 1, m_F = 0\rangle$ which is not the case in normal decoupling theory. Thus both qubit bases are sensitive to pulse imperfections. For an estimation on the fluctuation of the pulse area, we use the remaining power fluctuation value after power stabilization. This

number is $\lesssim 1\%$ which can account for an infidelity of only $1\,\%$. Note however that this number is acquired in-loop of the feedback circuit, so that the fluctuations at the position of the atoms might be bigger. A remaining fluctuation of $4\,\%$ could already account for the decay in fidelity we observe.

Another mechanism which acts almost symmetrically on the different qubits is depolarization by off-resonant scattering from the Raman lasers which erases phase as well as population information. For $(|\uparrow_z\rangle, |\downarrow_z\rangle)$, no decoupling is necessary as the results showed. We can thus use this as a reference and just apply the decoupling Raman light without tuning it into two-photon resonance (no RF power on the EOM). In this way, the qubits are subject to off-resonant scattering but do not undergo Raman oscillations. Experiments showed that this leads to a decay in fidelity of $8\,\%$ at 100 pulses. As was noted in the section on the Raman setup (4.2.1), a quantitative estimate on the scattering rate is difficult. We find that the observed infidelity after 100 pulses is within the errorbar of this estimation.

4.4. Summary and outlook

We have successfully implemented and tested the dynamical decoupling of Zeeman-state qubits in the same hyperfine state. We have achieved an application-ready coherence time of about $20\,\mathrm{ms}$, a 20-fold improvement compared to no decoupling. It is worth pointing out that these results have been achieved with just $10\,\mu\mathrm{s}$ of incoherent optical pumping for state preparation, as no cooling to the motional ground state is necessary in contrast to previous approaches.

The coherence time can probably be further extended by making more efficient use of the optical power on the atom, e.g. by using a carrier-free modulation method such as using an AOM instead of an EOM. Another avenue for improvements would be having weaker constraints by the experimental sequence. This would allow to also use more advanced decoupling sequences like XY4 which are resilient against experimental pulse imperfections and which should achieve the observed decoupling with less pulses and thus less scattering. Additionally, larger Zeeman splittings would enable faster driving of the Raman transition so that faster fluctuations can be compensated. This being said, our result is only a factor of about 3 away from a coherence time only limited by the scattering due to the omnipresent optical dipole traps [63], which can not be decoupled.

In addition to the application of dynamical decoupling, the developed high-fidelity gates also enable for the first time single-qubit operations on the often used memory states $|F, m_F = \pm 1\rangle$. While they are currently limited to multiples of π-pulses, this is already sufficient for many applications.

5. Quantum repeater node for quantum key distribution

The content of this chapter follows the publication:
Quantum Repeater Node Demonstrating Unconditionally Secure Key Distribution
S. Langenfeld, P. Thomas, O. Morin and G. Rempe,
Physical Review Letters **126**, 230506 (2021).

In this chapter we will experimentally demonstrate how two atoms in a common cavity can be used for realizing a quantum repeater node for quantum key distribution. We will start by introducing the topics of quantum repeaters, quantum key distribution and how these can be combined for the demonstrated application. We will then continue with presenting the necessary theoretical and experimental foundation which is specific for this experiment and goes beyond the general description provided in Ch. 2. Against this backdrop, we then display the experimental demonstration and its analysis which is followed by an outlook on future improvements and new trajectories for research and applications.

5.1. Overview

5.1.1. Quantum repeater

In classical networks, repeaters build the backbone of long-distance communication to mitigate signal losses along the transmission lines by means of signal amplification and redundancy. In quantum networks, qubit amplification in its naive meaning is forbidden by the no-cloning theorem [20]. Thus, quantum teleportation was invented in order to transport a precious qubit deterministically after the probabilistic creation of entanglement between the communication partners [27]. This leaves the part susceptible to loss to the creation of entanglement, which can be repeatedly tried until a herald confirms that it has been established. While this is a major advantage, it relies on actually establishing the entanglement and also keeping it alive until it will be used for teleportation (or other purposes). The establishing of entanglement is still limited by the no-cloning theorem, so that the probability of creating an entangled link per trial via a fiber-network is given by:

$$p = \eta_S \eta_R e^{-L/L_a}, \tag{5.1}$$

where η_S and η_R are the efficiencies of the sender and the receiver, L is the fiberlink distance and L_a is the attenuation length of the fiber, currently upper-bounded by the transmission

in telecom fibers to $L_{a,1550} = 22\,\mathrm{km}$. Even if perfect sender and receiver efficiencies are assumed in combination with the GHz electronics used in classical communication, the communication rate between e.g. Munich and Berlin still drops down to the Hz regime. Obviously this is not sufficient for today's demands on network communication rates.

A possible solution to this issue was put forward by Briegel et al. in 1998 [35], the so-called quantum repeater. The idea, which is depicted in Fig. 5.1, is relatively straightforward: a string of intermediate repeater nodes connects the two communication parties Alice and Bob. Alice and Bob, as well as all other repeater nodes, try to establish next-neighbor entanglement (a), e.g. via optical Bell-state measurements (BSM). This process can be performed in parallel and its success rate scales with the distance between nearest neighbors. Upon success, local BSMs on each repeater node (b) swap the entanglement to Alice and Bob (c). In principle, by combination of many (noisy) intermediate entangled pairs, the entanglement of Alice and Bob would be of low fidelity. Briegel et al. showed that this can be avoided by nested purification, i.e. by preparing many intermediate pairs in parallel which are purified to a high-fidelity entangled pair. It turns out that this results in a polynomial overhead in time and a logarithmic overhead in number of qubits per node, which gives a fundamental advantage compared to the exponential decay described above.

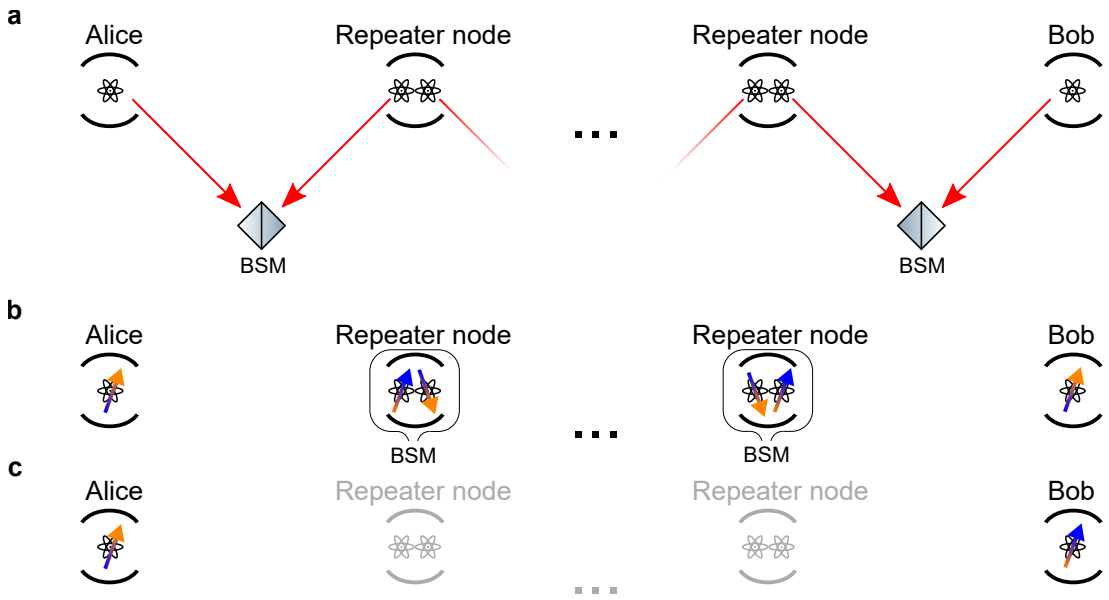

Figure 5.1.: Illustration of quantum repeater. **a** The total transmission line is separated into smaller links which independently attempt to create nearest-neighbor entanglement via Bell-state measurements (BSM). **b** Local BSMs swap the entanglement from the nearest-neighbor to the next higher level. **c** In the end, Alice and Bob share an entangled pair.

Nowadays, multiple extensions of the original repeater protocol have been proposed. Their main difference lies in compensating the loss error (rate) and also operational errors (fidelity) not by heralding and purification but by implementing the operations in a fault-tolerant way via quantum error correcting codes [109]. While this has significant advantages especially for very long distances where the communication time of the heralding signal becomes dominant, they also require significantly more simultaneous resources to

implement their error-correcting codes. Having these resources available seems to need years if not decades of further research. For the reminder of this chapter we will only consider the so-called first generation quantum repeaters which rely on a heralding signal.

5.1.2. Quantum key distribution

In quantum key distribution (QKD), or rather classical-key extension by means of quantum communication (to be precise), Alice and Bob want to generate a shared cryptographic key which they can use as a one-time pad for message encryption and decryption [133]. It has been proven, that this generated key can be secure based on the laws of quantum physics, so that a potential adversary Eve has no possibility of eavesdropping [134].

The initial concept of QKD was introduced by Bennett and Brassard in 1984 (BB84) [22], a protocol which is still used in today's research and applications. The protocol works as follows: Alice, the sender, chooses randomly from two sets of non-orthogonally polarized photons (e.g. H, V and D, A) and sends a string of these photons to Bob, the receiver. Bob measures the incoming photon's polarization in either the (H,V) or the (D,A) detection basis. Afterwards they publicly announce, over an authenticated channel, in which basis they prepared or measured the photons, but of course without enclosing which specific state they prepared/measured. For all photons which have been prepared/measured in the same basis, their information should 100 % correlate, which they can use as a key. The beauty of BB84 and QKD in general lies in detecting an eavesdropper. Alice and Bob can compare a subset of their results, and if the correlation is below a certain threshold, Alice and Bob have to conclude that an eavesdropper intercepted the transmitted photons. This conclusion is governed by the no-cloning theorem of quantum mechanics [20] and the non-orthogonality of the transmitted states. Of course this scheme has certain drawbacks. The requirement of having an authenticated public channel for announcing the preparation/measurement basis already necessitates a shared secret which will be used for this purpose, which motivates the labeling key-extension rather than key-distribution. In the worst case, this could also mean that no key is extended because the newly shared secret has to be used for the next authentication step. However, there are authentication algorithms which work efficiently enough to have a net-extension of the key [135].

Obviously, in the lab and even more so in real-world applications, Alice and Bob will not find 100 % correlation in their results. As it is difficult to differentiate between device imperfections and the errors introduced by Eve, the uncalibrated device scenario assumes that all errors have to be attributed to Eve [133]. In any case, algorithms have been developed which perform (classical) error correction (also called information reconciliation) to get a perfectly correlated key and subsequent privacy amplification [136] to reduce the information Eve has on that key. There are limits to when these algorithms can be applied. It is beyond the scope of this thesis to derive the different limitations for different attack scenarios or error-correction schemes, but the most fundamental limit should be given here:

In one-way classical post-processing, only either Alice or Bob publicly gives information while the other one only listens. Assuming the most general form of attacks, this puts the

listener (Bob) and Eve at equal footing. Thus, the secret fraction of the key is given by the uncertainty of Eve on the shared key minus the uncertainty of Bob [137]:

$$r_S = H(A|E) - H(A|B), \tag{5.2}$$

where H is the conditional Shannon entropy [138], i.e. a figure of how much information is enclosed in one set, or equivalently, how much uncertainty there is in one set (e.g. the set $\{1^n | n \text{ integer}\} \ni \{1...1\}$ has 0 uncertainty and thus carries 0 information, independent of the length n of the string). Evaluating this for the four-state BB84 protocol yields [133]:

$$r_S \geq 1 - h(e_X) - h(e_Z), \tag{5.3}$$

with e_X, e_Z being the quantum bit error rates (QBERs) in the two respective bases (e.g. horizontal and diagonal as used above) which indicate phase and bit-flip errors, respectively. h is the binary entropy function

$$h(x) = -x \log_2(x) - (1-x) \log_2(1-x). \tag{5.4}$$

At $e = e_X = e_Z \gtrsim 11\,\%$, the secret fraction r_S drops to zero and no secret key can be exchanged. [1]

Another practical drawback of QKD is due to the fundamental principle of QKD itself, namely that the transmitted photons cannot be cloned, so that the achievable communication rate and distance are highly limited by the exponentially scaling transmission losses. At this point, the formerly discussed quantum repeater finds a remedy for this limitation [75], which will be discussed in the next section.

5.1.3. A quantum repeater for quantum key distribution

The arguably simplest form of what we call a quantum repeater is a single intermediate node between Alice and Bob. While this setup is not sufficient for breaking the exponential scaling of rate versus distance, it can already modify the exponential decay constant so that the overall rate scales with the square root of the channel loss. If such a setup is used for quantum key distribution, it bears the additional simplification that the nested error correction can be performed classically on the obtained key, which further reduces the necessary resources down to having two quantum memories in between Alice and Bob. Such a scheme was proposed in 2016 [75]. It combines BB84 with the idea of quantum repeaters where the transmission distance is sliced so that individual slices can operate individually and are later combined by entanglement swapping via a BSM. The protocol is as follows (Fig. 5.2): First, one of the quantum memories of the quantum repeater node emits a photon whose polarization is entangled with the memory. This photon is sent to Alice who performs a polarization measurement in a randomly chosen detection basis,

[1] Interestingly, Shannon already showed that the amount of information in the presence of noise is given by $R = 1 - h(e)$. Classically, only bit-flip errors are possible. If this is extended to bit-flip and phase errors, the equation becomes $R = 1 - h(e_X) - h(e_Z)$. Although this is the same equation as above, the meaning appears fundamentally different to me. It says that the amount of information in the exchanged key becomes 0, rather than just talking about the shared information of Bob and Eve.

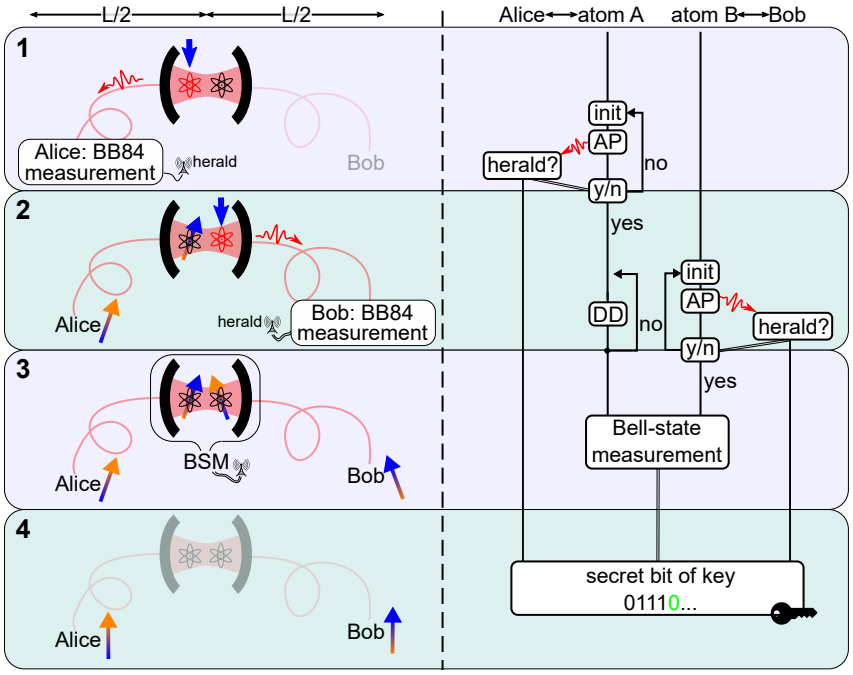

Figure 5.2.: Illustration of our QKD quantum repeater implementation. Four steps for distribution of one bit of a secret key. The vertical axis loosely indicates time while the horizontal one indicates distance. **1** Atom A is initialized and repeatedly performs atom-photon (AP) entanglement until Alice heralds the successful transmission and detection of the photon in a BB84 measurement scheme. **2** The same for atom B and Bob, while dynamical decoupling (DD) on atom A increases the coherence time of the correlation shared by atom A and Alice. **3** After both Alice and Bob have detected a photon, the central repeater node performs a Bell-state measurement (BSM) on atom A and B, which swaps the correlation from atom A-Alice and atom B-Bob to Alice-Bob. **4** Together with the BSM result, Alice and Bob share one more bit of a raw key. Using classical error correction and privacy amplification, this can be converted to a secret key, given that the QBER is small enough.

just like in BB84 (1). If she detected a photon, she publicly announces this to provide a herald for the successful transmission. If no photon arrived, the protocol starts again by re-creating a new photon-memory entangled pair. As soon as the transmission for Alice has been successful, the same procedure starts for the second quantum memory and Bob (2). Note that during Bob's attempts, the first quantum memory preserves the established correlation with Alice. If both Alice and Bob have heralded the successful transmission, a local BSM is performed on the two quantum memories to swap the entanglement (or rather classical correlation) to Alice and Bob (3). Depending on the result of the BSM, which is publicly announced, Bob applies a bit flip or not. Afterwards error correction and privacy amplification as in BB84 are employed to distill a perfectly correlated and secret key (4). As each transmission line only has half of the total length, the rate scales with $e^{-L/(2L_a)}$, a fundamental advantage compared to direct transmission. This comes at the cost of generating and detecting two photons and performing a potentially probabilistic BSM. The impact of these processes on the achievable rate will be discussed in Sec. 5.2.1, but intuitively it is already clear that this repeater scheme will only exploit its benefits

starting from a minimum communication distance so that the scaling advantage surpasses the additional resource disadvantages.

At this point we would like to note, that recently there has been the discovery of a new QKD protocol without repeater, the twin-field QKD [139]. Surprisingly, this scheme achieves the same scaling behavior as the described repeater and thus also beats the repeater-less bound, a term which now certainly has to be reconsidered. While its experimental implementation is far simpler as it does not rely on quantum entanglement, there seems to be no clear avenue on how to scale it further and reach the polynomial scaling behavior promised by extended repeater chains. This is why there is still a lot of research going on investigating how different hardware platforms perform in a variety of quantum repeater proposals [74, 140–146].

5.2. Theory

5.2.1. Key generation yield

The figure of merit used in Ref. [75] is the (secret) key rate per channel usage. The advantage of this figure compared to the typically used rate per time (e.g. in kHz) is that it does not depend on the repetition rate of the protocol, which would have made it impossible to compete with today's communication devices operating at GHz repetition rates.

In order to evaluate the performance of a QKD repeater, we thus have to compare it to the efficiency per channel usage of direct transmission, i.e. normal BB84. For direct transmission, this efficiency is easy to calculate for the raw key rate which is equal to the yield and reads:

$$\mathsf{yield}_{\mathsf{direct,L}} = p_{A\to B} = \eta_S \eta_R e^{-L_{A\to B}/L_a}, \tag{5.5}$$

just like introduced earlier. For the implementation with $^{87}\mathsf{Rb}$, $L_a = 1.1\,\mathsf{km}$ $(4\,\mathsf{db/km})$ at $\lambda = 780\,\mathsf{nm}$. If direct transmission is repeated until success, the distribution of channel usages N until success $P(N)$ forms a geometric series given by:

$$P(N) = p_{A\to B} \times (1 - p_{A\to B})^{N-1}, \tag{5.6}$$

$$\langle N \rangle = 1/p_{A\to B}. \tag{5.7}$$

In the repeater case, the trials of Alice and Bob individually are just like direct transmission with $L_{C\to A,B} = L_{A\to B}/2$, assuming they use the same hardware so that $\eta_{S,R}$ are the same

$$p_{A,B} = \eta_S \eta_R e^{-L_{A\to B}/(2L_a)}. \tag{5.8}$$

The expectation number of overall channel usages is however not uniquely defined. A possible option would be for example the sum of both channel usages $N_A + N_B$, while the community has converged on using the expectation value of the maximum trials of

Alice and Bob, $\langle N \rangle = \langle \max(N_A, N_B) \rangle$ which does not have an exact solution but can be approximated in a high- and low-loss regime [141]:

$$\langle \max(N_A,N_B) \rangle \approx \begin{cases} \frac{1}{p_A} + \frac{1}{p_B} - \frac{1}{p_A+p_B-p_Ap_B}, & \frac{1}{p_A} \leq n^*, \text{low loss limit,} \\ \frac{1}{p_A(1-(1-p_B)^{n^*})}, & \frac{1}{p_A} > n^*, \text{high loss limit.} \end{cases} \tag{5.9}$$

Here, n^* is the maximum number of trials allowed for Alice and Bob. This cut-off is motivated by the limited coherence time of qubit memories, so that the repeating process on atom B has to be stopped before atom A has decohered significantly. If this happens, the whole process has to be restarted which wastes the channel usages invested so far. Equation (5.9) only describes the number of channel usages for Alice and Bob receiving a photon. In order to complete the process, the BSM on the central repeater node has to be successful. Thus the overall rate employing a quantum repeater is:

$$\mathsf{yield}_{\mathsf{repeater}} = \frac{p_{\mathsf{BSM}}}{\langle \max(N_A,N_B) \rangle}. \tag{5.10}$$

The error correction and privacy amplification steps are the same for the direct transmission and for the repeater scenario. Here the important quantity is the quantum bit error rate as introduced in Sec. 5.1.2. For direct transmission, the experimentally most relevant error source for long-distance communication are dark counts of the detectors. As these give uncorrelated results, the signal-to-noise ratio degrades due to the decay in signal for increasing communication distance while the dark count rate stays constant. With state-of-the-art detectors ($p_{\mathsf{dc}} < 1\,\mathsf{Hz}$) and very short photons (FWHM $\approx 1\,\mathsf{ns}$), an optimistic estimation gives a maximum transmission distance of $90\,\mathsf{dB}/(0.2\,\mathsf{dB/km}) = 450\,\mathsf{km}$, which is indeed close to the current maximally achieved fiber-based direct transmission distance [57]. For repeater schemes, there are many more contributors to the QBER. The three dominant ones are the initial fidelity of the atom-photon entangled pairs, the decoherence of atom A during the waiting time for atom B, and the fidelity of the BSM. For state-of-the-art experiments, all of these numbers are in the few-percent region, which makes just beating the threshold of QBER $< 11\,\%$ the prime objective in the current phase of research. We should note, however, that there are also higher error thresholds which allow for communication in the presence of larger errors [147]. One commonly used threshold is QBER $= 14.6\,\%$, which is secure against individual attacks on Alice and Bob, but is not secure against collective attacks, thus it is not *unconditionally* secure. Allowable error rates can be further increased by using two-way communication, i.e. Alice and Bob communicate bi-directionally in the post-processing phase. For a BB84-based scheme, tolerable error rates go up to $18.9\,\%$, but on the cost of significantly reduced key rate [147]. Thus, for tackling the unconditionally secure protocol without further assumptions on the communication in the post-processing phase, we will always compare to the $11\,\%$ threshold. The secret key fraction as function of QBER can then be evaluated according to the already introduced formula:

$$r_S = 1 - h(e_X) - h(e_Z), \tag{5.11}$$

which is also depicted in Fig. 5.3(a).

Figure 5.3(b) depicts a simulated comparison between direct transmission and achievable repeater rate. The underlying mathematical equations are taken from Ref. [75]. The

direct transmission starts with a higher initial rate due to additional imperfections in the repeater process, such as a non-unity Bell-state measurement efficiency and fidelity. It then decays linearly in this logarithmic plot with a rate-distance exponent of $-L/L_a$. The repeater starts with a disadvantage but can potentially achieve higher rates compared to direct transmission at larger distances, due to its improved scaling with distance having an ideal rate-distance exponent of $-L/(2L_a)$. For large distances, the time it takes to get a successful event for atom B and Bob gets on the order of the coherence time of atom A, so that the QBER increases which finally results in zero rate at a distance of about $8L_a$ for the given experimental parameters.

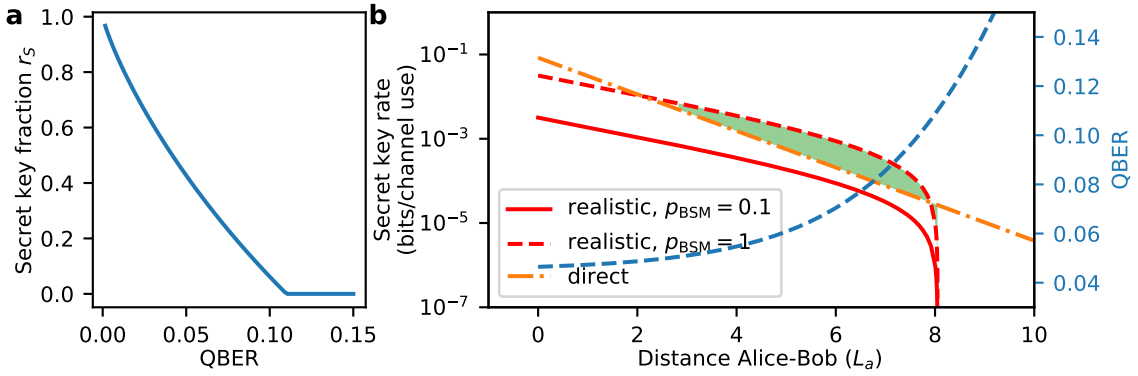

Figure 5.3.: Simulation for key distribution rate of quantum repeater. **a** Secret key fraction of a key with a given quantum bit error rate (QBER). **b** Secret key rate for two realistic repeater setups with different Bell-state measurement probabilities p_{BSM} and the direct transmission using the same experimental parameters. The green shaded area highlights the advantage of the repeater. The same plot shows the increase in QBER for longer distances due to a longer dephasing time.

From this one can deduce two possible benchmarks. First and obviously, the goal is to beat direct transmission which, however, currently seems to be a task far from reach. Recently there has been one experimental demonstration claiming to have achieved that [148]. Although they presented an excellent experiment, their treatment of the involved losses and their choice of QBER-threshold (14.6 % instead of 11 %) makes their claim in my opinion untenable. Indeed, the involved losses can be accounted for in two different ways. Given the single-trial success probability $p(\eta_R, \eta_S, L_{A\to B})$, we can attribute all losses including setup inefficiencies to the communication distance, i.e. $\eta_R\eta_S = 1$. Then the equivalent distance in the direct transmission case is $L_{A\to B}/L_a = -\ln(p)$ while in the repeater case it is $L_{A\to B}/L_a = -2\ln(p)$. Obviously, for the same $\eta_R\eta_S$, this is favorable for the repeater and thus makes it easier to beat the direct-transmission threshold. However, in my opinion, this is not scientifically correct, as the setup inefficiencies are a fundamental component of any experimental implementation. We thus choose the second option for attributing losses, which gives $L_{A\to B}/L_a = -\ln(p) + \ln(\eta_R\eta_S)$ for the direct transmission case and $L_{A\to B}/L_a = -2\ln(p) + 2\ln(\eta_R\eta_S)$ for the repeater case. This still has a scaling advantage with decreasing p, but at a larger initial disadvantage given by $\eta_R\eta_S$. The experimental origin of this disadvantage is clear: while direct transmission only requires one photon emission and detection, even the zero-distance repeater needs two emissions and detections.

The more realistic benchmark to beat, and one which is independent of this discussion,

is thus observing the fundamentally different scaling behavior of a repeater versus direct transmission, thus to observe a rate-versus-distance exponent of $-L/(2L_a)$ instead of $-L/L_a$.

5.2.2. Bell-state measurement of two atoms in the same cavity

To our knowledge, a Bell-state measurement of two atoms in the same cavity has never been demonstrated before. There has been one experiment performing a two-qubit gate within the same cavity [66] but without having the capabilities of extending it to a BSM, and other experiments projecting two specific qubits into an entangled state [65, 149]. Here we will use the latter scheme to perform a BSM. The principal idea is similar to the well-known linear optics Bell-state measurements [150, 151], in which the Hong-Ou-Mandel effect is used to erase which-way information of two incoming photonic qubits on a beam splitter [152]. The projection and measurement of the photons on subsequent polarizing Beam splitters and single-photon detectors allows to distinguish two of the four Bell states. The scheme of Ref. [149], initially put forward by Duan et al. [153], makes use of the common cavity mode to erase the which-way information of the two photons. Afterwards, these photons are again measured in a polarization-resolved detection setup (Fig. 5.4(a)).

a

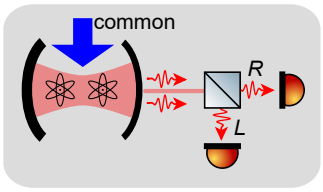

b

Bell state	spin exchange	polarization detection
$\|\Psi^+\rangle$	symmetric ✓	anti-bunched ✓
$\|\Psi^-\rangle$	asymmetric ✗	anti-bunched ✓
$\|\Phi^+\rangle$	symmetric ✓	bunched ✗
$\|\Phi^-\rangle$	symmetric ✓	bunched ✗

Figure 5.4.: Distinction of a specific Bell state. **a** Illustrative view of experimental setup for optical Bell-state measurement of two atoms in a cavity. **b** Selection arguments due to Bosonic nature of the photons in the same spatial mode and the subsequent polarization-resolved detection.

We now reason how this scheme can be used for detecting one specific out of the four well-known Bell states:

$$\begin{aligned}
\left|\Psi^+\right\rangle &= \frac{1}{\sqrt{2}}\left(|\uparrow\downarrow\rangle + |\downarrow\uparrow\rangle\right), \\
\left|\Psi^-\right\rangle &= \frac{1}{\sqrt{2}}\left(|\uparrow\downarrow\rangle - |\downarrow\uparrow\rangle\right), \\
\left|\Phi^+\right\rangle &= \frac{1}{\sqrt{2}}\left(|\uparrow\uparrow\rangle + |\downarrow\downarrow\rangle\right), \\
\left|\Phi^-\right\rangle &= \frac{1}{\sqrt{2}}\left(|\uparrow\uparrow\rangle - |\downarrow\downarrow\rangle\right).
\end{aligned} \tag{5.12}$$

Without loss of generality, we will use $|\uparrow\rangle = R$-polarized photons and $|\downarrow\rangle = L$-polarized photons. The first step of separating the four Bell states is by counting the number of photons in a given polarization, where two times the same polarization heralds one of the

$|\Phi\rangle$-states while two different polarizations heralds one of the $|\Psi\rangle$-states. As detecting twice the same photon polarization requires photon-number resolved detectors, we will concentrate on the $|\Psi\rangle$-states for heralding a specific Bell state. Then, the task lies in separating $|\Psi^+\rangle$ and $|\Psi^-\rangle$. This separation comes naturally due to the Bosonic nature of photons: the overall wave function of a photon, consisting of the spatial wave function and the spin wave function, has to be symmetric under particle exchange. The spatial wave function of two photons emitted simultaneously into the same cavity mode is symmetric as long as the photons are indistinguishable. Thus, any two photons which leave the cavity like that have to have a symmetric spin wave function, i.e. they have to be in one of the $|\Phi\rangle$-states or in the $|\Psi^+\rangle$ state, but they cannot be in the $|\Psi^-\rangle$ state (Fig. 5.4(b)). In combination with the already mentioned polarization resolved detection, this scheme allows to distinguish the $|\Psi^+\rangle$ state from all the other states.

5.2.3. State evolution and qubit timings

In the last section, we assumed without loss of generality that the BSM is performed in the circular detection basis (R,L). Here we motivate why we also chose this basis in the experiment. At the same time, we will reason which detection bases Alice and Bob will detect their photons in.

The fundamental difference between the detection in a circular (R,L) and in a linear (H,V) basis is the time-dependence of their corresponding atomic states. Circular photons are mapped to energy eigenstates while linear photons are mapped to atomic superposition states (see Sec. 2.2.2 and 5.3.4). Due to an intentional bias magnetic field in the experiment, the phase of the superposition states evolves over time with twice the Larmor frequency $2\delta_L$, which makes the success of the protocol timing dependent. There are two important timings in the protocol, namely the time difference between the photon emission for Alice and Bob Δt_{AB} and the timing of the BSM with respect to Bob, Δt_{BB}.

Alice and Bob randomly select between measuring in one of two non-orthogonal bases. Again we will see that choosing a circular basis for one of those is beneficial. As photon and atom are entangled, Alice and Bob's detections project atom A and atom B to a given state $|\Psi_{\mathrm{A}}\rangle$ and $|\Psi_{\mathrm{B}}\rangle$, respectively. This product state $|\Psi_{\mathrm{AB}}\rangle = |\Psi_A\rangle \otimes |\Psi_{\mathrm{B}}\rangle$ will determine the probability to detect $|\Psi^+\rangle$ in the BSM according to $p = |\langle\Psi_{\mathrm{AB}}|\Psi^+\rangle|^2$. These probabilities are summarized in Table 5.1. The first important conclusion is that, if the BSM is performed in the (H,V) basis, both the relative timing of the atom-photon entanglement attempts as well as the readout time for the photonic BSM are important. In contrast, for a BSM in (R,L), only the relative time Δt_{AB} matters. This makes it experimentally easier as the timing of the BSM can be chosen freely. This difference is fundamentally easy to grasp: $|\Psi^+\rangle_{\mathrm{RL}}$ is time-independent. In contrast, the phase of $|\Psi^+\rangle_{\mathrm{HV}}$ oscillates with twice the usual qubit frequency, i.e. $4\delta_{\mathrm{L}}$. Another important consequence and also reason for choosing the (R,L) basis is that due to this time/frequency-independence, $|\Psi^+\rangle_{\mathrm{RL}}$ is ideally decoherence-free against common mode noise [116] while $|\Psi^+\rangle_{\mathrm{HV}}$ is not. To summarize, we will perform the BSM in the circular (R,L) basis and one of the detection bases for Alice and Bob should also be (R,L). The other basis can be any linear basis. Following BB84, we will call the (R,L) basis Z-basis and the (H,V) basis X-basis.

Table 5.1.: The table shows the probability to detect $|\Psi^+\rangle$ in the Bell-state measurement given certain detection results for Alice and Bob in the preceding photon distribution process. Δt_{AB} is the time-difference between the photon emissions for Alice and Bob and Δt_{BB} is the time difference between the emission for Bob and the BSM.

BSM / Alice, Bob	$\left\|\langle\Psi_{AB}\|\Psi^+_{HV}\rangle\right\|^2$	$\left\|\langle\Psi_{AB}\|\Psi^+_{RL}\rangle\right\|^2$
H, H	$\sin^2(\Delta t_{AB}\delta_L + 2\Delta t_{BB}\delta_L)/2$	$\cos^2(\Delta t_{AB}\delta_L)/2$
H, V	$\cos^2(\Delta t_{AB}\delta_L + 2\Delta t_{BB}\delta_L)/2$	$\sin^2(\Delta t_{AB}\delta_L)/2$
V, H	$\cos^2(\Delta t_{AB}\delta_L + 2\Delta t_{BB}\delta_L)/2$	$\sin^2(\Delta t_{AB}\delta_L)/2$
V, V	$\sin^2(\Delta t_{AB}\delta_L + 2\Delta t_{BB}\delta_L)/2$	$\cos^2(\Delta t_{AB}\delta_L)/2$
R, R	0.5	0
R, L	0	0.5
L, R	0	0.5
L, L	0.5	0

Another conclusion is that the distribution of $(\delta_L \Delta t_{AB}) \bmod 2\pi$ has to be kept small. This requires the repetition period, i.e. the time difference between successive trials, to be a multiple of π/δ_L, so that the detected state is independent of which of the trials succeeded. Additionally, the distribution has to be kept small by having short photon durations as will be discussed in Sec. 5.3.4.

5.3. Experimental implementation

In this section we will motivate experimental procedures, techniques and parameters. We will start by detailing the experimental sequence which was implemented in the laboratory. Afterwards we will discuss every element of this sequence and which parameters have to be taken into account for a successful demonstration of a quantum repeater. Then we will give technical details on the detection setup for Alice, Bob and the optical Bell-state measurement. After a brief discussion of the optimum magnetic field, we will be ready to present the achieved results in the next section.

5.3.1. Detailed sequence logic

A schematic of the protocol has already been illustrated in Fig. 5.2. Here we give an overview over the actually implemented timings of the individual constituents. Figure 5.5(a) shows the experimental steps run for every atom-photon entanglement attempt which consist of the atom initialization, the actual photon generation and an idle communication waiting time. This sub-sequence is now integrated into the main experimental sequence (Fig. 5.5(b)) which is repeated at a repetition rate of 160 Hz. The main sequence starts by repeating a maximum of 40 times the atom-photon entanglement sub-sequence. If Alice detected none of the photons, i.e. no success, the sequence jumps to utility tasks such as atom cooling and beam power stabilizations. However, as soon as one photon is detected, i.e. success, the sequence progresses to the connection attempts for atom B and

Bob. Here dynamical decoupling is alternated with atom-photon entanglement attempts to prolong the coherence time of atom A. We do this by attempting AP-entanglement up to three times before applying one DD pulse. The combined sequence is repeated up to 14 times, thus there are in total 42 attempts and up to 14 DD pulses. If none of those attempts succeeded, the sequence again proceeds with the aforementioned utility tasks. Otherwise, the sequence jumps out of this loop and proceeds with the Bell-state measurement which consists of a remapping Raman and the two-photon generation as will be further explained in the following sections. In order to analyze the key distribution rates, we keep track of how many attempts were conducted as well as how often the individual sub-sequences succeed. Experimentally, the repeat-until-success-or-maximum-trials is realized by using external sequence selectors to our field-programmable-gate-array (FPGA) experimental control. The sequence is repeated a certain number of times. If however a photon was detected, one of the external sequence selectors is triggered which starts the next sub-sequence at a controlled time.

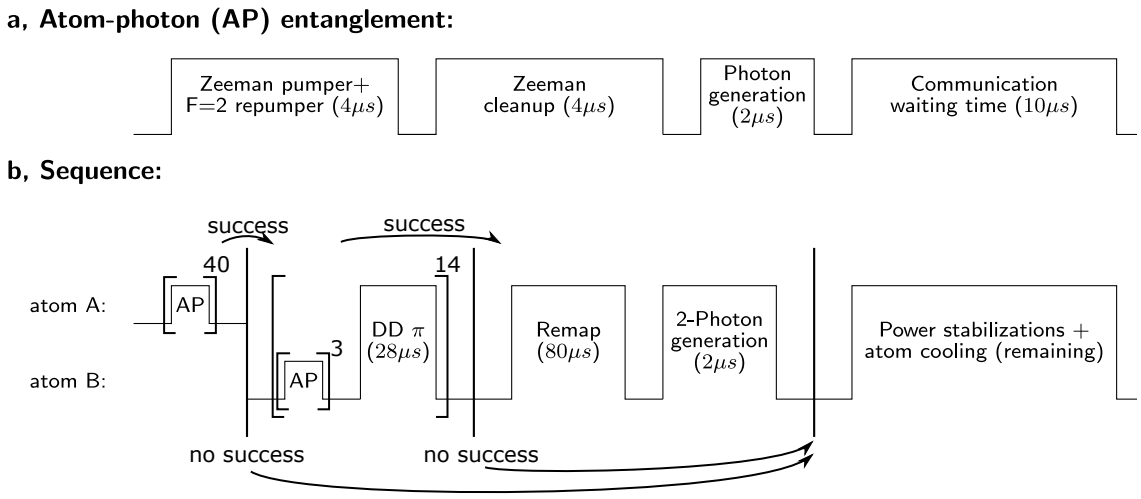

Figure 5.5.: Detailed timing of quantum repeater sequence. **a** Sub-sequence which is run every time atom-photon (AP) entanglement is attempted. **b** Combined sequence which runs at a repetition rate of 160 Hz. Curvy arrows indicate conditional jumpers which act based on the success or failure of the AP entanglement attempts.

5.3.2. Atom trapping and positioning

As was introduced in Sec. 2.3, the atoms are trapped in a two-dimensional potential. In contrast to the experiments presented in Ch. 3, the polarization of the traps and their depths was modified to account for the special needs of the repeater sequence. The red-detuned $\lambda = 1064\,\mathrm{nm}$ trap depth was increased by a factor six while the intra-cavity trap depth was increased by a factor three. The trap depths were not further increased due to already significant heating of the cavity setup in the vacuum chamber. The deeper traps result in a better loading rate and better trapping times. It also reduces the Lamb-Dicke parameter [154] which enables more incoherent repumping attempts before atoms

are heated out of the trap. At the same time, deeper traps allow to make the traps purely linearly-polarized. The reason for this is not yet fully understood, but probably has to do with the trap geometry [85]. Purely linear traps are important, as otherwise ground-state cooling would be necessary for avoiding varying virtual magnetic fields which lead to decoherence on a μs timescale. Good ground-state cooling takes hundreds of μs, so not relying on it is crucial for fast atom initialization which is an important parameter for the repeater scheme. The downsides of deeper traps are more heating of the setup, more off-resonant scattering decreasing the maximally achievable coherence time to about 60 ms [63] and an amplification of any residual virtual magnetic field due to non-perfect polarization tuning. All of these downsides are experimentally manageable or not significant for the timescales under investigation.

Minimum interatomic distance Here we test which minimum distance the atoms should have in order to avoid cross talk via cross-illumination of the pumping and STIRAP control pulses. To this end, we use the full repeater sequence including dynamical decoupling but with a fake second atom at a given distance to the real one (see App. B). We also set the number of trials on this fake atom to a specific number to see how the infidelity scales with number of trials. Thus, this experiment tests all cross-illuminations, addressed or global (but then far-detuned), and including coherence time. Figure 5.6(a) shows the fidelity for a range of (fake) interatomic-distances with 42 initialization and atom-photon entanglement attempts on the fake atom. For distances larger than 5 μm a plateau is reached. As a safety margin, we chose to only allow interatomic distances of $\geq 8\,\mu$m. Figure 5.6(b) shows how the fidelity evolves for this distance with increasing number of trials. The decay is more pronounced for the X-basis than for the Z-basis which is expected as superposition states dephase with the first scattering event while eigenstates can undergo multiple scattering events without depolarization. We also conclude that having about 40 trials is a reasonable limit to stay in a high-fidelity region.

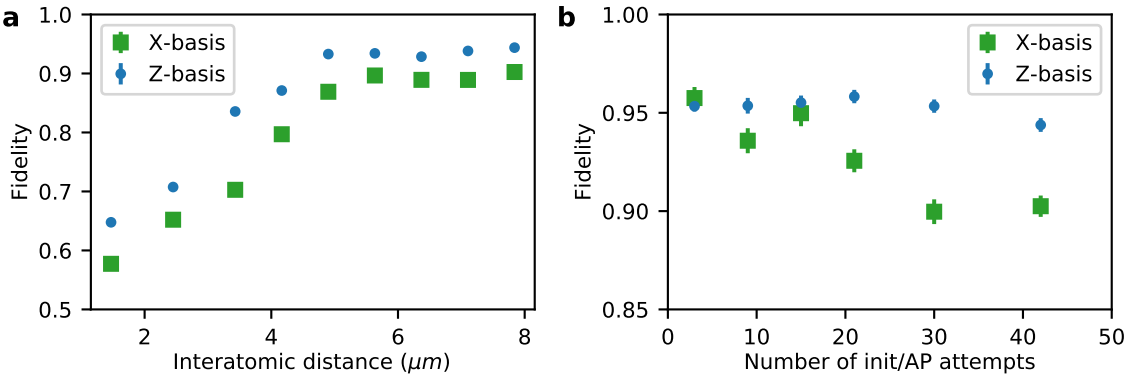

Figure 5.6.: Infidelity due to addressing cross-illumination. **a** Fidelity evaluated in single-atom experiment with applied cross-illumination of 42 pulses on a fake atom at varying distance. **b** Same sequence with fixed distance of 8 μm and varying number of trials.

Absolute atom position In the last paragraph we decided on the distance of the two atoms. Here we discuss the absolute positioning. We observed that we have to tune

certain parameters, mostly the intra-cavity trap power, depending on the atom position to maximize coherence time. This is likely due to some residual virtual magnetic fields which lead to dephasing if the atoms are not in their motional ground state. As only atom A needs an extended coherence time, we circumvent this issue by fixing the position of atom A and allow for a range of positions for atom B to increase data rate. The positions are chosen so that the two atoms are on average centered within the cavity mode which gives maximum efficiency of the photon production processes.

Image postselection While these restraints on the atom position are already checked during run-time, we do also postselect on the acquired images. Additionally to the position of the atoms, we also postselect on their width and the emitted fluorescence intensity. Both parameters allow us to detect multiple atoms which are close enough to look like one. We optimize these parameters by using the fidelity and data-rate obtained in test measurements as a quantitative estimate for how good the postselection is. The survival rate of this image postselection is on average $42\,\%$.

5.3.3. Atom initialization

Each attempt to generate atom-photon entanglement starts with initializing the atom in $|i\rangle = |F = 2, m_\mathsf{F} = 0\rangle$. For atom B, this has to be performed without disturbing the qubit stored in $|F = 1, m_\mathsf{F} = \pm 1\rangle$ in atom A. Thus, any optical field which addresses states in $|F = 1\rangle$ near-resonantly has to be applied via the optical addressing system, while light fields near-resonant to $|F = 2\rangle$ can be applied globally. For Zeeman pumping to $|m_\mathsf{F} = 0\rangle$, we use a π-polarized global beam which is $-56\,\mathsf{MHz}$ red-detuned compared to the $|F = 2\rangle \leftrightarrow |F' = 2\rangle$ transition on the D_1 line. In this configuration, the population in $|F = 2, m_\mathsf{F} = 0\rangle$ is dark due to dipole selection rules. We chose the D_1 line, as its hyperfine splitting is larger compared to the D_2 line, so that nearby excited states do not disturb the dark transition as much. By also fine-tuning the polarization of the beam to be precisely π, we achieved a m_F-selectivity in excitation probability of $1 : 2000$ with a typical depopulation of $m_\mathsf{F} \neq 0$ in $1\,\mu\mathsf{s}$. Due to the decay ratios of the excited states (which are effectively equivalent for D_1 and D_2 excited states), $50\,\%$ of every excitation ends up in $|F = 1\rangle$ instead of $|F = 2\rangle$. Thus, the atom needs to be constantly repumped to $|F = 2\rangle$ to have an efficient multi-step Zeeman pumping process. As motivated above, this repumper has to be applied through the addressing system and is thus also π-polarized. It is $35\,\mathsf{MHz}$ blue-detuned compared to the $|F = 1\rangle \leftrightarrow |F' = 2, m_\mathsf{F} = 0\rangle$ transition on the D_2 line. Here, the D_2 line was chosen because a significantly different wavelength compared to the STIRAP control pulses would necessitate re-aiming of the addressing AOD due to the wavelength-dependent deflection angle. The repumper in this configuration depopulates $|F = 1\rangle$ in $1.2\,\mu\mathsf{s}$ (1/e time). Together, the Zeeman pumper and the repumper are applied for $4\,\mu\mathsf{s}$. Afterwards, only the Zeeman pumper is applied for another $4\,\mu\mathsf{s}$ but at twice the power. This pulse is used to depopulate all $m_\mathsf{F} \neq 0$ states in $|F = 2\rangle$ as these would otherwise emit a photon in the next step which reduces the fidelity. In the end, this sequence prepares about $66\,\%$ in the desired state and takes only $8\,\mu\mathsf{s}$. While we could apply the pumping sequence for longer to achieve better preparation efficiency, this would also disproportionally increase the amount of cross-illumination via the addressing system

on the other atom. Thus care has to be taken to not saturate the atom with the addressed repumper but only repump as little as possible. Next to these figures of merit, which are clearly important for the repeater as they directly influence the atom-photon entanglement efficiency and fidelity, another experimentally important figure is the trapping time of the atoms. Thus all parameters were also optimized to reduce heating of the atoms. In the end, the trapping time for a single atom with an average number of trials $\langle N \rangle \approx 9$ was 8 s.

5.3.4. Atom-photon entanglement

We already gave a brief overview for the atom-photon entanglement process in Sec. 2.2.2. The most important parameter for optimizing the atom-photon entanglement step is the atom-cavity detuning Δ_{ac}, as it determines the photon production efficiency and the cross talk due to off-resonant scattering of the two atoms via the common cavity mode. Figure 5.7(a) shows again the atomic level structure and optical fields used for atom-photon entanglement generation, however this time including qualitatively the AC-Stark shifts due to the optical dipole traps (see App. A). In contrast to the memory experiment in Ch. 3, here $m_{\mathsf{F}} = 0$ is used so that also $|F' = 0\rangle$ is of importance. The impact of that can be seen in the efficiency (Fig. 5.7(b)) and the scattering probability (Fig.5.7(c)) for the AP-entanglement process. As there is no allowed transition from $|F' = 0\rangle$ to $|F = 2\rangle$, it cannot contribute to the STIRAP process. However, cavity photons can still scatter from an atom prepared in $|F = 1\rangle$. Thus, the efficiency dips at resonance to $|F' = 0\rangle$ while the scattering probability peaks. The same holds for $|F' = 2\rangle$, as $|F = 2, m_{\mathsf{F}} = 0\rangle \leftrightarrow |F' = 2, m_{\mathsf{F}} = 0\rangle$ is dipole-forbidden. The optimal working point is thus far red-detuned or in-between $|F' = 1\rangle$ and $|F' = 2\rangle$. Figure 5.7(b) already includes the photon production efficiency for the BSM readout, which dips in-between these two levels. Thus, only being far red-detuned is a viable option for having high efficiency and low scattering of the overall process. From the analysis in Ref. [84] we know that being too far detuned is also counter-productive due to an increased relative excitation probability of $|F' = 3\rangle$ which also cannot contribute to the STIRAP process. We thus chose $\Delta_{\mathsf{ac}}/2\pi = -200\,\mathsf{MHz}$ with respect to $|F' = 1, m_{\mathsf{F}} = 1\rangle$ which equals a detuning of $2\pi \times -115\,\mathsf{MHz}$ to the closest excited state $|F' = 0\rangle$. Experimentally we verified that this gives a decay in fidelity of 0.08 pp per photon. As an additional example, at $\Delta_{\mathsf{ac}}/2\pi = 28\,\mathsf{MHz}$ this decay in fidelity is 1.8 pp per photon.

Another potential concern for populating the cavity mode while one of the atoms already stores a qubit is an AC-Stark shift due to a single photon in the cavity which could alter the phase of a superposition qubit. While this number is theoretically already small for the chosen detuning $\Delta\phi/\mathsf{photon} = 0.017\,\mathsf{rad}$, in the repeater protocol employing BB84 it should not be an issue at all, as only trials are of relevance where Alice and Bob measured in the same basis. Thus if the first atom stores a superposition qubit, the second photon will be projected on a linear polarization which induces no differential AC-Stark shift on the qubit states.

One more experimental parameter which has to be chosen wisely is the shape and including that the duration of the emitted photons. As the photons will just be detected on intensity-sensitive photon counters, no mode-matching to external references is necessary [155].

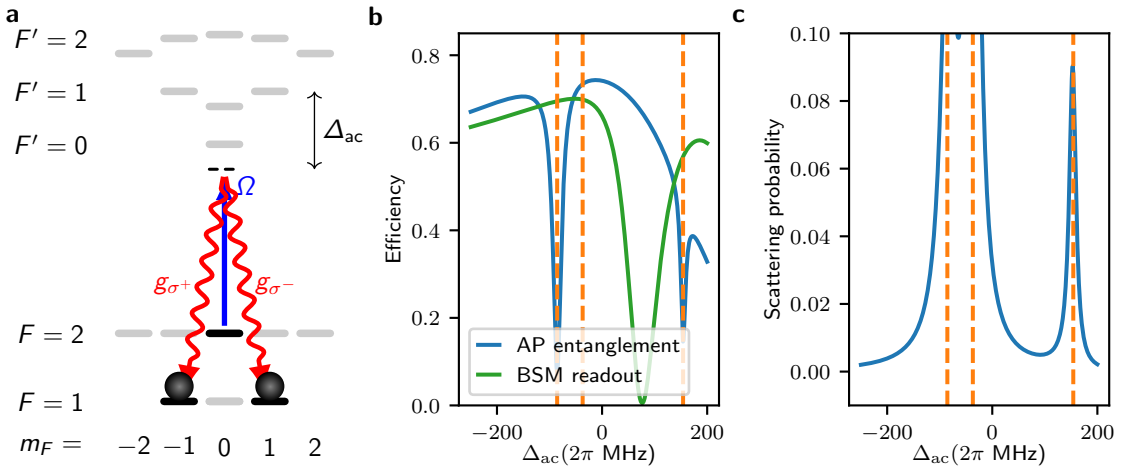

Figure 5.7.: Atom-cavity detuning for atom-photon entanglement. **a** Level scheme including AC-Stark shifts of the excited states. **b** Efficiency of the photon generation processes including the cavity escape efficiency. **c** Scattering probability for a second atom in the same cavity mode and prepared in one of the qubit states when the first atom emits a photon. Dashed vertical lines indicate the position of the excited states $|F', m_F = 0\rangle$ and all detunings are with respect to $|F' = 1, m_F = 1\rangle$.

However, the photon shape still plays an important role for maximizing efficiency, for minimizing the distribution of emission times Δt_{AP} discussed earlier and for minimizing the detection window relevant for the effective dark counts of the detectors. While the latter two demand a photon as short as possible, the efficiency calls for a photon bandwidth significantly smaller than the cavity bandwidth.

Figure 5.8(a) shows the control pulse we used and the resulting photon shape. Note that we do not use a sophisticated control pulse but just a square-shaped pulse. The reasons are that we do not need a specific shape, and experimentally relevant, that the frequency chirp for actively shaped photons of the employed length and at a detuning of $2\pi \times -160\,\mathrm{MHz}$ is larger than the bandwidth of the AOMs used for shaping the control pulse. Thus the optical power varies significantly within the pulse which inhibits the control of the accurately needed amplitude-phase relation of the control pulse. Choosing a square control pulse fixes this as no frequency chirp is necessary because a square pulse creates a constant AC-Stark shift.

In part (b) of the same figure, we analyze how the photon duration and thus Δt_{AP} induces an infidelity. To this end, we perform a single-atom experiment similar to Wilk et al. [58] (see App. B). As expected, depending on the qubit oscillation frequency $2\delta_L$, the impact of the photon duration varies. The theoretical curves for the fidelity F are obtained via $\delta F = F - \int_{\Delta T} (e(t)^2 \cdot F(t) dt)/\Delta T$, where $e(t)$ is the amplitude of the emitted photon and ΔT the range of integration. The curves are offset from 0 infidelity as for this test measurement the length of the second (readout) photon was held constant at $\tau_R = 0.32\,\mu\mathrm{s}$ which adds a τ-dependent infidelity.

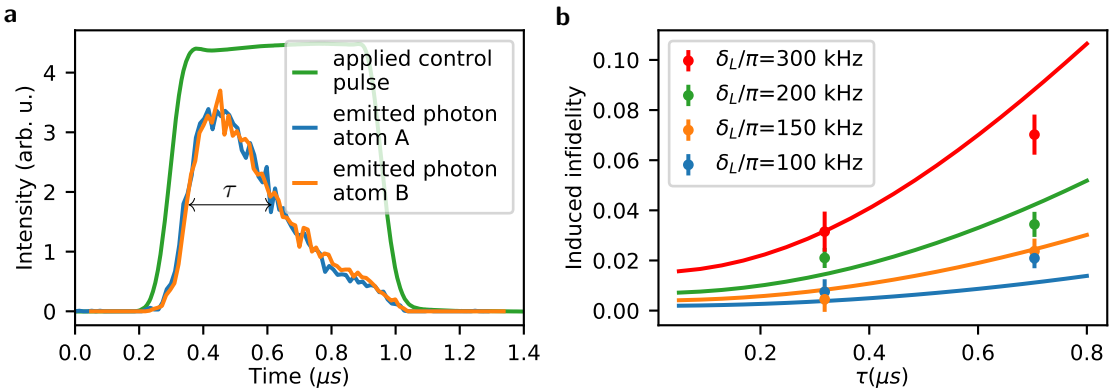

Figure 5.8.: Temporal shape of atom-photon entangled photons. **a** Control pulse and resulting single photon shape for the generated photons. **b** Infidelity induced by too long photons with respect to the qubit oscillation frequency $2\delta_L$. This data was obtained with a corresponding single-atom experiment (App. B).

5.3.5. Dynamical decoupling

The general scheme and the coherence time results have been extensively discussed in Ch. 4. Here we introduce how we apply this technique in the context of the quantum repeater protocol. Currently the DD pulses can neither be applied atom- nor hyperfine-selectively. Thus when they are applied to atom A, they also modify the state of atom B, which e.g. affects the initial state preparation in $|m_F = 0\rangle$. Thus, the DD pulses can only be applied before state initialization of atom B. Another aspect is how often a DD pulse is applied. Here we chose to apply a DD pulse after every third trial on atom B (Fig. 5.5). This results in not too many pulses to be sensitive to decoupling-induced infidelity but is also often enough (every $100\,\mu s$) to decouple from all relevant decoherence mechanisms. Last, the qubit of atom A has to be independent, or at least independent up to a bit-flip, of the number of trials on atom B. This is ensured by having the DD rotation axis aligned with the qubit X-axis as described in the DD chapter. Thus, we only have to account for bit-flips in the Z-basis which we do in a post-processing step.

5.3.6. Bell-state measurement

The Bell-state measurement (BSM) is performed by mapping the atomic qubits onto photons and performing a photonic linear BSM. As the qubits are stored in $|F = 1\rangle$ and the cavity is close to resonance from $|F = 1\rangle \leftrightarrow |F' = 0\rangle$, one solution for the STIRAP readout process is to go from $|F = 1\rangle$ to $|F' = 1\rangle$ as was done in previous experiments using this level scheme [53, 58]. However, as the control pulse is also resonant with the final state of this process, it continues to produce photons which reduces the fidelity. To prevent this, the control pulse is typically only applied for a short duration which results in a bad efficiency. Also, the atom-cavity detuning is typically chosen to be $0\,\mathrm{MHz}$ so that dipole selection rules turn off the process at least partly. This would lead to significant cross talk between the two atoms which excludes this solution.

Here we choose another solution, which is transferring the qubit to $|F = 2\rangle$ before reading it via the already introduced readout of the memory scheme (Sec. 2.2.1). We perform this transfer via a stimulated Raman transition for which we use two phase-locked lasers in two-photon resonance. This Raman process executes the two transfers $|F = 1, m_F = -1\rangle \leftrightarrow |F = 2, m_F = 1\rangle$ and $|F = 1, m_F = 1\rangle \leftrightarrow |F = 2, m_F = -1\rangle$ simultaneously. It has the advantage of being magnetic-field independent in first order but also has the disadvantage that it needs to be performed relatively close to resonance to the excited states [63] (Fig. 5.9(a)). One issue which arose which was not observed in our earlier work including this transition is depicted in Fig. 5.9(b), namely a difference in Rabi frequency for the two transitions, although both are in two-photon resonance. This effect has been reproduced in simulations, and is due to the admixture of the Zeeman-detuned, unintended $\Delta m_F = 0$ transitions. The symmetry for the two transitions is broken by the sign of the Zeeman detuning, and the magnitude of the admixture is given by the Rabi frequency and the magnitude of the Zeeman splitting. Thus, experimentally, we tune the Rabi frequency to minimize this effect ($t_\pi = 80\,\mu$s) while still not being too sensitive to decoherence during the driving.

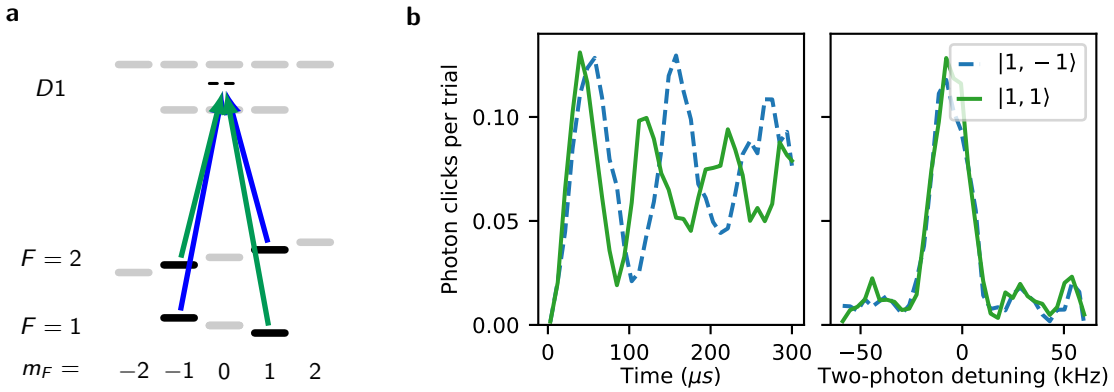

Figure 5.9.: Remapping Raman used for transferring the qubits from F=1 to F=2. **a** Level scheme and light fields used to drive the stimulated Raman transition. **b** Rabi flopping and two-photon detuning scan for relevant transitions. The color coding of (a) and (b) matches, which showcases the different driving speeds of the two relevant Raman transitions.

In addition, due to the relatively small single-photon detuning of $2\pi \times 400\,\mathrm{MHz}$ to both excited state hyperfine manifolds, the probability to scatter incoherently is 7 % [63], which reduces the efficiency and the fidelity of the process. In total, we achieve a remapping efficiency of 90 % (original scheme: 10 % [53, 58]), which makes it the solution of highest efficiency. In order to compare the achievable fidelity, we again perform an experiment similar to Wilk et al. [58] (see App. B) and obtain a photon-photon correlation fidelity of about 94 % (original scheme: 89 % entanglement fidelity [53]).

After transferring the atomic qubits to $|F = 2\rangle$, they are mapped onto photons via the already introduced readout of the memory scheme. As the cavity resonance cannot be changed within the sequence, the relevant atom-cavity detuning for this transition is $\Delta_{ac}/2\pi = -200\,\mathrm{MHz}$, at which the theoretical photon generation efficiency is still 65 % in contrast to the 69 % at $\Delta_{ac}/2\pi = -100\,\mathrm{MHz}$ in the memory protocol. As was discussed

earlier, these two photons are then guided to a polarization-resolved detection setup where a potential detection of $\left|\Psi_{\mathsf{RL}}^{+}\right\rangle$ is heralded.

5.3.7. Detection setup: Alice, Bob and optical BSM

The purpose of a polarization-resolved detection setup is to give information on the projection of an incoming photon onto a given basis. This is achieved with a certain fidelity which mostly depends on the extinction ratio ϵ of the two basis-defining states on the polarization-resolving element, most often a polarizing beam splitter (PBS). The infidelity due to a finite ϵ depends on the to-be-measured state. Distinguishing between a state which is aligned with the detection basis (expected fidelity is 1) and a state which is perpendicular to the detection basis in the Bloch sphere (expected fidelity is 0.5), the infidelity $\delta\mathcal{F}$ is given by:

$$\begin{aligned}\delta\mathcal{F}_{\parallel} &= \frac{1}{1+\epsilon} \xrightarrow{\epsilon\gg 1} \frac{1}{\epsilon},\\ \delta\mathcal{F}_{\perp} &= \frac{\sqrt{\epsilon}}{1+\epsilon} \xrightarrow{\epsilon\gg 1} \frac{1}{\sqrt{\epsilon}}.\end{aligned} \tag{5.13}$$

Thus, in order to achieve small infidelities independent of the input state, the extinction ratio ϵ should be at least on the order of 10^4 so that the resulting error is at most $1\,\%$.

In a real-world application, there would be three detection setups for this experiment, namely two setups at variable distances playing the role of Alice and Bob, and a local setup for the optical BSM. This would necessitate an optical switch between these different options which can be switched on a tens of μs scale while preserving $\lambda = 780\,\mathsf{nm}$ photonic polarization qubits with high fidelity and high efficiency. Such a device is not commercially available. First tests on a self-built switch based on a Mach-Zehnder-Interferometer are promising but not yet ready for a demanding experiment like the one presented here. As a workaround, we chose to use a single detection setup with fast polarization rotation capabilities to allow having different detection bases for Alice, Bob and the BSM.

A picture and schematic of the resulting detection setup is shown in Fig. 5.10. Starting at the incoupling fiber („from atom“) the light first passes a $\lambda = 780 \pm 1.5\,\mathsf{nm}$ bandpass filter which is used for filtering background and intra-cavity trap light. Afterwards, the light passes two waveplates which are used to compensate the birefringence of the single-mode fiber leading from the atom to the detection setup. Note that two waveplates are enough (in contrast to three in the memory detection setup, Ch. 3), as we only rely on compensating the fiber up to an angle which rotates the qubits perpendicular to the detection basis. In the projective measurement on the PBS, this angle has no impact. Next is the key ingredient of the setup, namely a DC-coupled EOM with an efficiency of $99\,\%$, a bandwidth of $100\,\mathsf{MHz}$ and importantly a polarization extinction ratio of better than $1:1000$. As the parasitic polarization component has a slightly different spatial mode due to the birefringence of the EOM crystal, we could further improve this number to $1:10000$ by coupling the output light to single-mode fibers. For switching between the two detection bases (H,V) and (R,L), the rotation axis of the EOM needs to be aligned with (D-A). This we achieve by having another two waveplates in-between the EOM and the

PBS. Two waveplates are again enough for the above reason. The projective measurement is performed on a PBS, again with extinction ratio better than $1:10000$. This is achieved by combining two PBS, as typically the extinction of a single PBS in reflection is limited to $< 1:1000$. After the projective measurement, the light is polarization-matched and coupled to a polarization maintaining (PM) single-mode fiber which directs the light to superconducting nanowire single photon detectors (SNSPDs) for maximum efficiency and very low dark counts. In total, the efficiency of this detection setup is approximately $68\,\%$, which is the product of the SNSPD efficiency including its fiber-fiber-connector (0.9), the PM-fiber transmission (0.96), the free-space to fiber coupling (0.9) and the remaining optical elements (0.88). The intrinsic dark count rate of the SNSPD is very low ($\Gamma_{\mathrm{dc}} \approx 1\,\mathrm{Hz}$) but intra-cavity trap light at $\lambda = 772\,\mathrm{nm}$ leaking through the bandpass filters increases the effective dark count rate to $\Gamma_{\mathrm{dc}} \approx 40\,\mathrm{Hz}$.

Figure 5.10(c) shows an illustration of the operation of the EOM in the underlying Poincaré-sphere. The EOM voltage is tuned so that upon application of a TTL signal

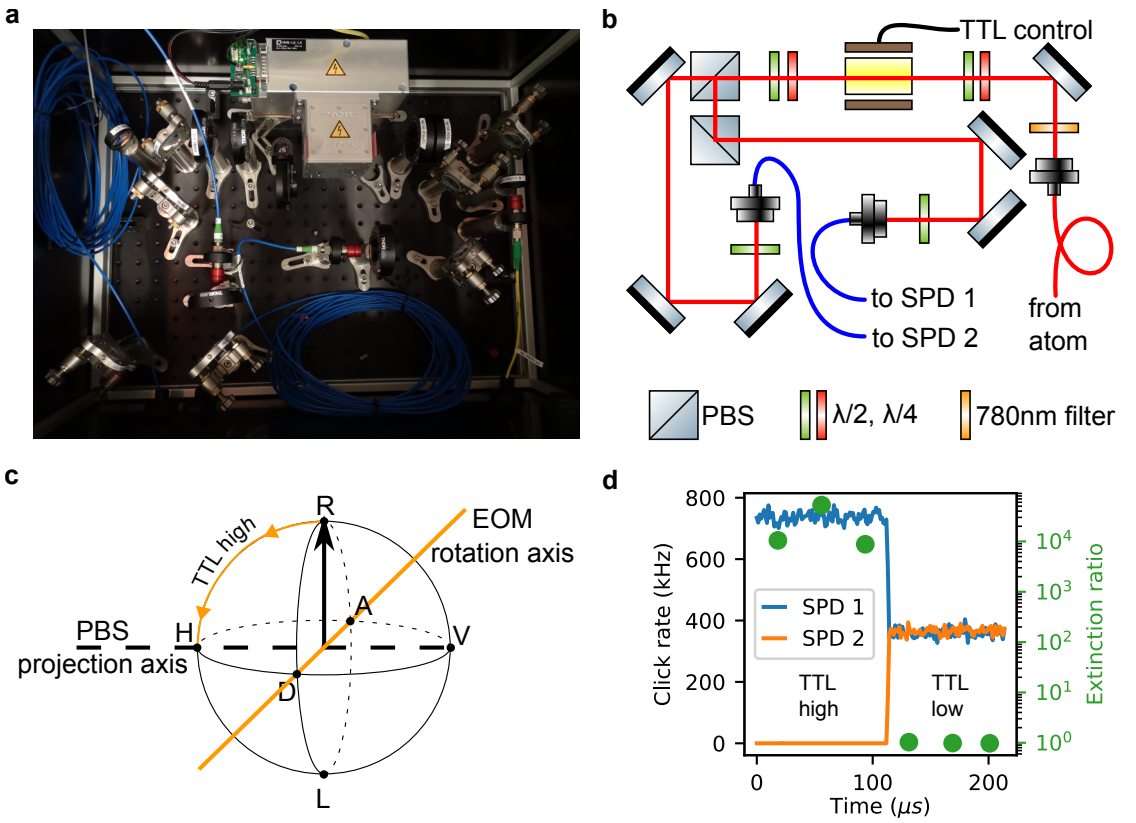

Figure 5.10.: Detection setup used for Alice, Bob and the BSM. Picture (**a**) and schematics (**b**) of the detection setup employing a DC-coupled EOM for fast detection basis switching. **c** Poincaré-sphere illustrating the EOM operation. If the input to the EOM is logical high, it rotates qubits along the (R-L)-line onto the PBS projection axis ((H-V)-line). **d** Histogram of detected clicks in SPD 1 and 2 and their ratio. For R-polarized input light, the mentioned rotation leads to an extinction on the PBS of 1:10000. If the EOM is set to logical low again, the R-polarized input is detected 50:50 in the (H,V) basis.

the polarization is rotated by $\pi/2$, which maps (R,L) $\rightarrow$ (H,V) and thus changes the detection basis accordingly. In Fig. 5.10(d), the time histogram of the two detectors as well as their ratio is plotted for R-polarized input light. With applied EOM voltage („TTL high"), the input is rotated to H so that maximum extinction is achieved on the following PBS. When the TTL is switched low, the polarization rotates back within 100 ns without noticeable ripple effects as observed with other EOMs [156].

This setup thus allows to perform the BB84 measurements of Alice and Bob, as well as the optical Bell-state measurement. For testing the repeater at different communication distances, ideally different fiber lengths are used between detection setup and atom-cavity system. This has the obvious disadvantage of experimental overhead for switching between different lengths, but it also has the disadvantage that these losses affect the BSM in the same way, which is not the case in the real repeater application. The same holds for introducing artificial losses instead of using different fibers, where the losses simulate a specific distance. We thus apply the losses electronically which allows to apply them selectively for Alice and Bob but not for the BSM. Experimentally this is done by AND-gating the photon clicks with a TTL signal which is only applied depending on the outcome of a biased coin flip whose bias can be set to choose the loss-level (see App. D).

5.3.8. Magnetic field

Another important experimental parameter which has only been touched upon multiple times now is the magnetic guiding field. It has an impact on the maximum driving speed of the dynamical decoupling (Ch. 4), of the remapping Raman (Sec. 5.3.6), the optimal photon duration (Sec. 5.3.4), timing accuracy within the sequence (Sec. 5.2.3) and also influences the polarization gradient cooling. Taking these dependencies into account, we chose a Larmor frequency of $\delta_L = 50\,\mathrm{kHz}$ which is a good compromise between driving speeds in the tens of μs and timing accuracies on the order of 100 ns.

5.4. Experimental results

The presentation of the experimental results is straightforward. First we will show the results of the repeat-until-success strategy, which is central to the repeater protocol. This will also confirm the equivalent communication distances to Alice and Bob. We will then discuss the yield or raw key rate of our repeater implementation. Afterwards, the most uncertain but also most crucial part will be discussed, namely the performance of the Bell-state measurement and the achieved quantum bit error rates. In combination with the yield, this finally results in the presentation of the secret key rate.

5.4.1. Repeat until success

For the first time in this group, a single-photon generation process is combined with a repeat-until-success-strategy. Figure 5.11 shows the success probability distribution for

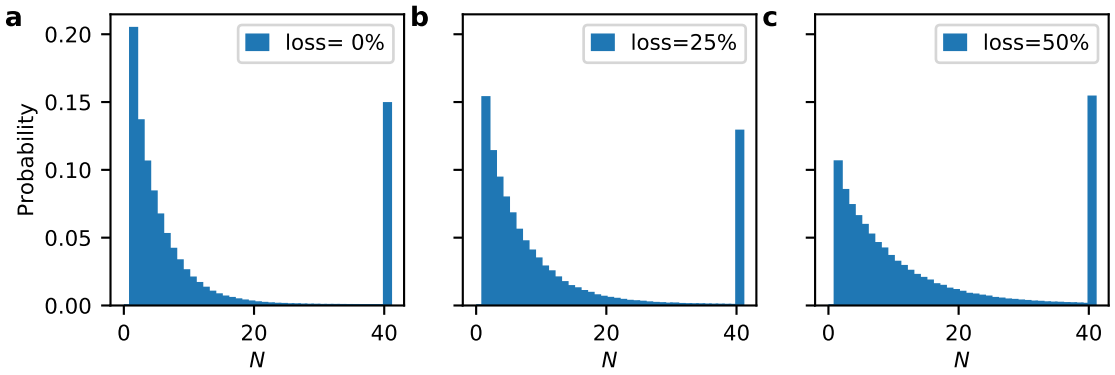

Figure 5.11.: Histogram of number of trials until success. Histograms for three different artificial-loss scenarios with a maximum number of trials $n^* = 40$.

atom A/Alice as a function of the number of trials N for three different introduced artificial losses. As expected the probability distribution follows a geometric series (Eq. (5.6)).

For all distances, there is a residual contribution at $N = 40$ which signals that none of the trials was successful as we try a maximum of $n^* = 40$ times. Especially visible for zero additional losses (Fig. 5.11(a)), this contribution is significantly larger than the expected integrated probability $P(N > 40)$. We attribute this to an imperfect image pre-/postselection. If the addressed atom is lost from the trap, it can have already emitted enough fluorescence to be registered as a valid atom and thus a valid image. The loss will only be detected in the next image and the experiment stops. Obviously if the atom is lost, no photons are generated and the sequence repeats the maximum amount of trials. For the further analysis, we exclude these cases as they increase the amount of channel usages and can be avoided by either longer trapping times or better classical image processing. By doing so, the number of channel usages is reduced by factors $(0.82, 0.85, 0.81)$ for the three different artificial losses $(0, 25, 50)\,\%$, respectively.

With this in mind, we use the probability distribution to evaluate the efficiency per channel usage $p = \eta_S \eta_R e^{-L/(2L_a)}$ and thus also the zero-distance photon sender and receiver efficiency $\eta_T = \eta_S \eta_R$. Additionally, we use these curves to calibrate the equivalent communication distance between central station and Alice/Bob in units of the attenuation length, $L/(2L_a)$. From $\eta_T = 1/\langle N(L = 0)\rangle$, we get $\eta_T = 22\,\%$ which approximately matches the product of the state preparation efficiency $\eta_P = 0.66$, the single-photon emission probability $\eta_E = 0.65$, the first fiber-coupling $\eta_{FC} = 0.85$ and the detection-setup efficiency $\eta_D = 0.68$. Additionally we get $\exp(-L/(2L_a)) = (1, 0.744, 0.541) = 1 - (0,25.6,45.9)\,\%$ which translates to $L/L_a = (0, 0.591, 1.23)$ for the three different artificial losses $(0, 25, 50)\,\%$, respectively. We attribute the discrepancy between the setting of the artificial losses and the actual losses to mechanical drifts in the optical pathway such as fiber couplings which lead to a fluctuation of the actual losses.

At this point, we can also analyze the atom trapping times and duty cycle for the different expectation values in number of trials $\langle N\rangle$. In basically all experiments presented so far in this thesis and more generally this group, experimental trials consisting of state preparation, manipulation and detection are interleaved with cooling of the atoms. Here,

however, we perform up to 40 cycles per atom before going back to cooling. Heating due to optical pumping then accumulates which eventually removes the atom from the trapping potential. By optimization of the cooling and pumping parameters, especially the detuning of the employed laser beams, we achieve trapping times of $(8, 5, 4)\,\mathrm{s}$ and experimental duty cycles of about $(25, 20, 15)\,\%$ for $\langle N \rangle = (4.6, 6.2, 8.6)$, respectively. This poses an important limitation to the current scheme as it prevents us from going to larger $\langle N \rangle$ and thus longer communication distances.

5.4.2. Raw key rate

After creating correlation between atom A/Alice and atom B/Bob, the Bell-state measurement swaps this correlation to Alice/Bob. We find an average success probability of the BSM of $p_{\mathrm{BSM}} = (5.07 \pm 0.03)\,\%$, which already includes the $50\,\%$ limitation of linear optics BSMs [151].

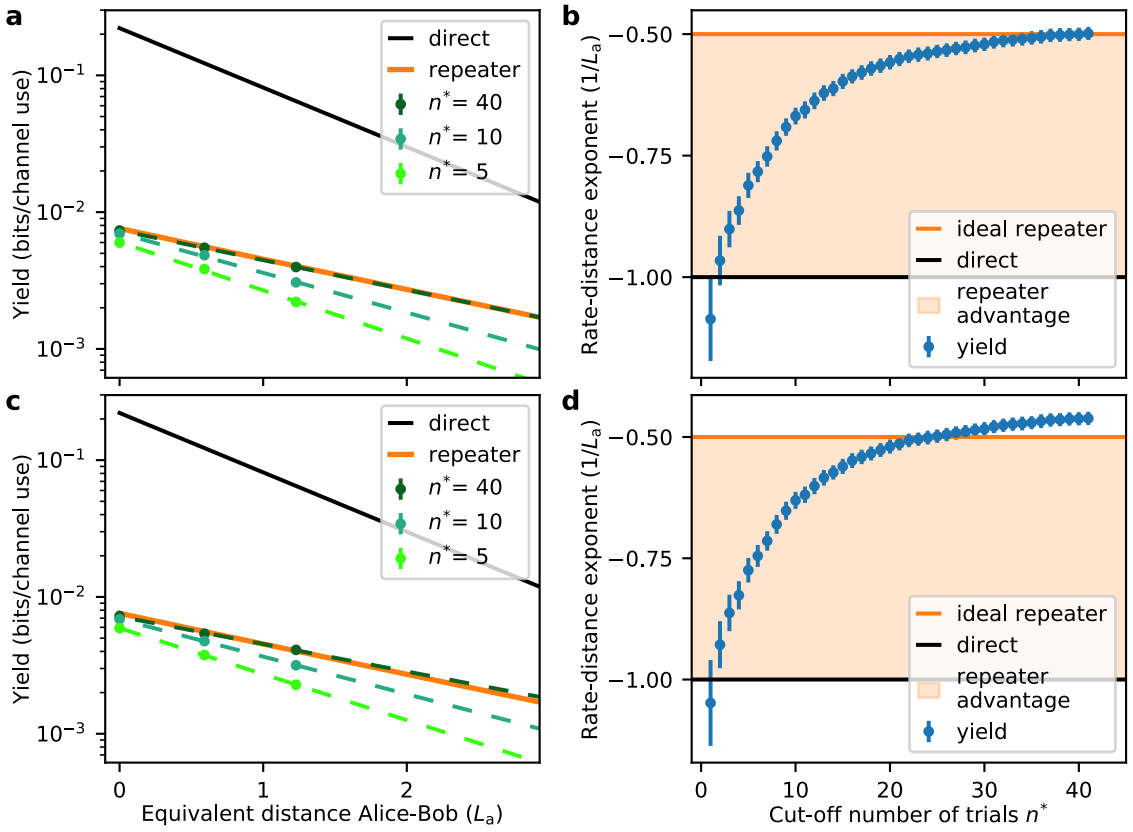

Figure 5.12.: Raw key rate analysis. **a** Raw key rate as a function of equivalent distance for different cut-offs n^*. The theoretical direct transmission and repeater rates are shown as a comparison. **b** Rate-distance-exponent which changes from direct transmission to repeater advantage with increasing n^*. **c & d** The same but without compensation of the BSM efficiency which falsely results in even better scaling. In (c), this is visible in the dashed line being above the theoretical repeater line (orange).

In the following, we analyze the yield of the key distribution, which basically is the number of successful BSMs normalized over the combined number of channel usages for Alice and Bob (see Eq. (5.10)). Figure 5.12(a) shows the achieved yield for the three different examined equivalent distances and for three different maximum number of trials n^* for both Alice and Bob. We analyze the yield for different numbers of the maximum number of trials as it is fundamental to achieving the repeater advantage. For $n^* = 40$, i.e. effectively without limitation for the examined distances, the experimental results match the underlying theory perfectly. At zero distance, the repeater yield compared to direct transmission is reduced by the BSM efficiency ($\sim 5\,\%$) and the additional photon generation and detection ($22\,\%$). Even at zero distance this disadvantage is already partly compensated by the repeat-until-success strategy whose effect increases further for larger distances and results in the advantageous repeater scaling. This scaling is highlighted in part (b) of the figure which shows the slope of linear fits to the data of (a). This slope resembles the rate-versus-distance exponent, the defining property for a quantum repeater. For $n^* = 1$, there is no repeating in the repeater, which results in a scaling exponent of $-1/L_a$, just like direct transmission. With increasing n^*, the repeater advantage unfolds and finally reaches the ideal repeater scenario with a scaling exponent $-1/(2L_a)$.

Note that for getting to these results, we have to compensate for a fluctuation in the BSM efficiency p_{BSM}. As the measurements are taken over multiple days, fiber-coupling efficiencies were not completely reproducible. It happened to be the case, that p_{BSM} was relatively larger for data presenting larger communication distances, with the exact numbers being $p_{\mathrm{BSM,L}} = (5.00, 4.97, 5.24)\,\%$ for $L/L_a = (0, 0.59, 1.23)$, respectively. The effect of that can be seen in Figs. 5.12(c) and (d), where we show the same data as in (a) and (b) but without this compensation. Obviously, the match between experiment and theory is not as good and the experimental results even beat the ideal quantum repeater scenario. Against this backdrop, we can be assured that our compensation leads to a realistic estimation of the repeater performance which will be even more important when analyzing the secret key rate later on. Experimentally, the fluctuation is compensated by multiplying each depicted rate for a given distance with $p_{\mathrm{BSM}}/p_{\mathrm{BSM,L}}$ where $p_{\mathrm{BSM,L}}$ is the BSM efficiency corresponding to this distance.

As this analysis is crucial to quantum repeater performance claims, we detail the error bar estimation for the presented data. The yield Y given in Fig. 5.12 represents a Bernoulli trial with $k \approx 10^6$ trials per data point, with the exact number depending on n^*. Thus, the error bars are given by $\sqrt{Y(1-Y)/k}$. In the next step, we want to faithfully include this uncertainty into the linear fits relevant for the data presented in Fig. 5.12(b). We perform Monte-Carlo simulations assuming the data points (error bars) represent the mean (one standard deviation) of a normally distributed random variable. We draw 1000 samples from these distributions, apply a linear fit to each individual set, and thus obtain distributions for the slopes. From the slope-distributions, we obtain the mean and one standard deviation which we finally plot in Fig. 5.12(b).

5.4.3. Bell-state measurement and quantum bit error rates

So far, only the success of the BSM in terms of efficiency was relevant. For analyzing the secret key rate, the fidelity of the BSM and the resulting QBER become of uppermost importance. We found that the BSM fidelity largely depends on the detection-time-difference $\delta\tau$ of the two BSM photon clicks. As we cannot investigate the BSM on its own, we analyze the resulting QBER of the key distribution for Alice and Bob both measuring either in the X- or the Z-basis. Remember that the BSM measurement is always performed in the Z-basis. Figure 5.13(a) shows the achieved QBERs for both bases as well as the relative number of clicks as a scan of $\delta\tau$. The shape of the number of clicks is given by the convolution of the two photon temporal shapes. The most important feature is the qualitative difference between the QBER in the Z- and the X-basis. While the QBER for the Z-basis stays low for all $\delta\tau$, the QBER for the X-basis rises significantly on the timescale of the photon length. Remarkably, the QBER rises even above the classically expected value of 0.5. This indicates that there is a coherent origin to this process.

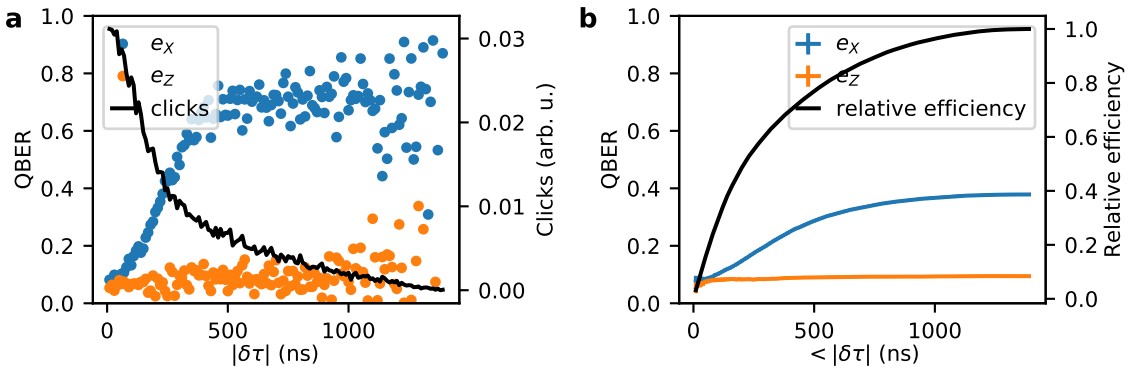

Figure 5.13.: Bell-state measurement. **a** QBER and number of clicks for a given time difference of the two BSM photon clicks. **b** Same data as in (a) when considering all clicks up to a given time difference.

In the following we try to analyze this behavior. Additional measurements referenced in this paragraph can be found in App. E. There are two possible approaches to this analysis. Either the BSM is assumed to always herald the $|\Psi^+\rangle$ state and the observed behavior is attributed to a phase evolution of the atoms in-between the two photon emissions of the BSM. Alternatively, internal processes make the photons distinguishable which results in the potential detection of the $|\Psi^-\rangle$ Bell state, as discussed in Sec. 5.2.2. In the end, both approaches are compatible with the observed effects as only states in the X-basis are sensitive to additional phases and only the X-basis measurements can differentiate between $|\Psi^+\rangle$ and $|\Psi^-\rangle$. We further verified that the change in fidelity correlates with the duration of the emitted photon. To this end, we repeated the same experiment with two different control pulses resulting in characteristic photon durations of 0.15 μs and 1 μs. Also for these durations, the QBER changes on the timescale of the photon duration. We can thus exclude all effects which are uncorrelated with the photon duration or control beam. Historically, a similar effect has been observed by multiple BSM or, more generally, photon-interference experiments [53, 149, 157]. Nölleke et al. [53] attributed this

effect to the inhomogeneous broadening of the atomic transition by atomic-temperature-induced fluctuations of the dipole-trap AC-Stark shift. This broadening leads to varying single-photon detunings which result in different photon emission times. The photons thus become distinguishable which reduces the interference contrast. While this analysis in-principle also applies to our implementation, we employ a 10-fold increased single-photon detuning ($-200\,\mathrm{MHz}$ versus $-20\,\mathrm{MHz}$) and our atomic linewidth is smaller ($10\,\mathrm{MHz}$ versus $14\,\mathrm{MHz}$) so that we can quantitatively exclude this effect. Casabone et al. [149] attributed this effect to a cycling, i.e. excitation and decay back to the initial state, of the atomic population before emitting the second photon. This kind of cycling adds a π phase shift to the atomic qubit with respect to the other atom which has already emitted a photon without cycling. This explains the correlation with the time-difference of the two emissions and thus the photon duration. From previous analyses [84], we know that the cycling probability for our system depends on the single-photon detuning. We thus repeated the same experiment with a single-photon detuning of $+28\,\mathrm{MHz}$ and $-150\,\mathrm{MHz}$ instead of $-200\,\mathrm{MHz}$.While the performance at small $\delta\tau$ was worse due to more cavity cross talk (see Fig. 5.7(c)), the qualitative behavior of the BSM was the same, though being less pronounced especially for the $+28\,\mathrm{MHz}$ case. While this makes it the most probable scenario, the improvement seems too small so that we tend to also exclude this cause. The same argumentation holds for control-field induced light-shifts on the atom, which lead to a differential evolution frequency of the two atomic qubits in-between the two photon emissions. These light shifts however also depend strongly on the single-photon detuning which is why we would have expected a significantly reduced effect for the smaller detunings. Lastly, the most recent experiment in the group of Ben Lanyon in Innsbruck [157] explains this effect by residual frequency differences between the two spatially separated photon emitters. In their case this seems reasonable as the photon duration is about $10\,\mu\mathrm{s}$ so that a frequency difference of $40\,\mathrm{kHz}$ is already sufficient to explain this effect. Such a frequency difference, however, would not scale with the photon duration and thus does not match our observations. Also, for our timescales, the residual frequency difference in the ground states would need to be on the order of $1\,\mathrm{MHz}$ which we can exclude experimentally.

In conclusion, none of the presented explanations in the literature matches our experimental observations which remains an open question for future investigations. The robustness of this effect over multiple platforms and the various regimes we examined suggests a more fundamental origin than regular experimental imperfections. It is worth noting that the exact emission mechanism of two atoms into the same cavity mode has not yet been described theoretically. Currently, we believe that the effect is related to dark states of the combined two-atom-cavity mode. Furthermore, a modeling that fully describes the temporal structure of the emitted electromagnetic field would give more insights. For instance, an analysis with our newly-developed homodyne temporal mode analyzer [155] might give further insights into this process. In a first step, this analysis could be applied to simulation data. For the application on experimental data however, an optical switch would be necessary so that the two atoms can still be well-prepared in a repeat-until-success strategy using single photon counters as presented in this chapter. Otherwise, the efficiency is too low to get measurements with significant signal-to-noise ratio in a reasonable amount of time.

For the application of secret key distribution, we can avoid this effect for the moment

by only using a maximum time-difference between the two photons clicks. The resulting relative efficiency and QBER when taking all cumulative clicks up to a maximum time-difference ($< |\delta\tau|$) are given in Fig. 5.13(b). For achieving a maximum secret key rate, the product of yield and secret-key fraction is optimized, i.e. the maximum $\delta\tau$ is chosen so that $\eta \times r_S(\mathrm{QBER})$ is maximized. The resulting QBER and η are given in Table 5.2. This optimization is valid for the key distribution process as these are information which can be made available to Alice and Bob during the classical post-processing step of the key distribution process.

Table 5.2.: Overview of achieved QBER for examined distances and for different detection-basis combinations for Alice and Bob. Additionally, we give the relative efficiency of the BSM due to a limited usable time-difference $\delta\tau$ of the two photon detection events.

distance (L_a)	Alice	Bob	$\delta\tau$	QBER	relative efficiency η
0	X	X	80 ns	$(8.3 \pm 0.5)\,\%$	0.12
0	X	Z	1400 ns	$(50 \pm 1)\,\%$	1
0	Z	X	1400 ns	$(53 \pm 1)\,\%$	1
0	Z	Z	250 ns	$(7.2 \pm 0.5)\,\%$	0.28
0.59	X	X	70 ns	$(8.7 \pm 0.6)\,\%$	0.11
0.59	Z	Z	290 ns	$(8.5 \pm 0.5)\,\%$	0.29
1.23	X	X	40 ns	$(8.9 \pm 0.6)\,\%$	0.06
1.23	Z	Z	910 ns	$(9.2 \pm 0.5)\,\%$	0.46

Whenever Alice and Bob choose the same detection basis, we achieve a QBER below 11 % by at least three standard deviations and thus demonstrate unconditional security for the secret key distribution process. As expected from BB84, the QBER is about 50 % if Alice and Bob measure in different detection bases. In the following, we analyze certain aspects of the achieved QBER. In single-atom experiments using the in-principle same protocol (see App. B), we achieve fidelities on the order of $\mathcal{F} = 96\,\%$ for eigenbasis measurements (see also Fig. 5.6(b)). These infidelities are mainly due to incoherent scattering in the remapping Raman (Sec. 5.3.6 and Ref. [63]), population cycling induced by scattering of the far-detuned STIRAP control pulse [84] and residual polarization alignment errors (Sec. 5.3.7). For a perfect BSM and uncorrelated infidelities of the two atoms, this single-atom fidelity $\mathcal{F}$ translates to QBERs (see App. E)

$$e_i = \frac{2}{3}(1 + \mathcal{F} - 2\mathcal{F}^2) \approx 7.8\,\%. \tag{5.14}$$

This is already within the range of achieved QBERs given in Table 5.2. On top of that, cross talk during the repeated attempts on Bob's atom further reduces the achievable QBER. Upon analysis of the obtained data as a function of N and thus the amount of cross talk, all results are within the error bars which are multiple percent for each individual N. We can still try to derive an indication for the expectable cross talk from single-atom experiments with simulated cross talk as we already depicted in Fig. 5.6(b). Here, a decay in fidelity of few percent was observed for the number of trials relevant to our results. A core contributor to achieving this slow decay in fidelity is the long coherence time due to dynamical decoupling. For the largest communication distance, the average number of

trials is about 9. At this point, qubits in the X-basis would have decayed to a fidelity of about 87 % without decoupling. While with decoupling, the fidelity is still at 94 % and only decays to 93 % at 40 retrials (see also Sec. 4.3.2).

Additional to these single-atom processes, our implementation of a BSM relies on the cavity to erase the which-atom or more generally the which-way information. For this, both atoms need to emit the BSM photon simultaneously. When measuring in the Z-basis, we do have the information which atom statistically emitted first. For example, if Alice detected $|\uparrow_z\rangle$ and Bob detected $|\downarrow_z\rangle$, then this should have no influence on the time-ordering of the two clicks in the BSM. If it did, we would have which-way information. Indeed, we observe a correlation of $50.6 : 49.4$ (ideally $50 : 50$) between Alice/Bob's qubit and the time-order of the detected clicks. Thus, the cavity correctly erases the which-way information. From this we conclude that the BSM itself operates with very high fidelity in the small $\delta\tau$-limit.

Table 5.3.: Secret-key fraction and relative efficiency for examined distances assuming an unbiased basis selection for Alice and Bob.

distance (L_a)	secret-key fraction r_S	relative efficiency η
0	0.105 ± 0.015	0.19
0.59	0.076 ± 0.032	0.20
1.23	0.062 ± 0.043	0.26

We can now use the results given above to calculate the secret-key fraction r_S as well as the combined relative efficiency assuming both basis settings are used in a duty cycle of 50 % (Table 5.3). Note that this is not necessarily the case as the so-called efficient BB84 [158] predominantly uses the more efficient key-distribution Z-basis. For reasons of generality, we will stick to the original BB84 scheme but keep in mind that this is a valid strategy when it becomes important to beat a specific direct-transmission benchmark. The error bar of the secret-key fraction follows from error propagation of the QBERs. Note that the relative uncertainty of the secret-key fraction, $\delta r_S / r_S$ diverges for $e_{X,Z} \to 0.11$ as $r_S \to 0$. This leads to significant errors in r_S and will become important for the error analysis of the secret key rate in the next section.

5.4.4. Secret key rate

The secret key rate is the product of usable yield and secret-key fraction, both of which have been discussed in the last sections. The experimental results are depicted in Fig. 5.14. The analysis is identical to the one of the yield. There are two important differences. First, the error bars are significantly larger compared to before. This is mainly due to the large relative error of the secret-key fraction which translates directly to the relative error of the secret key rate. Additionally, the amount of data is smaller for the secret key rate due to the limit in $\delta\tau$ which also results in a larger error of the adjusted yield. However, even with these significant error bars, Fig. 5.14(b) still shows the desired effect which is the transition from a direct-transmission scaling to a scaling which shows the repeater advantage. While the rate-distance exponent does not reach $-1/(2L_a)$ for large n^* this time, it is still significantly above the limitation fundamental to direct transmission. The

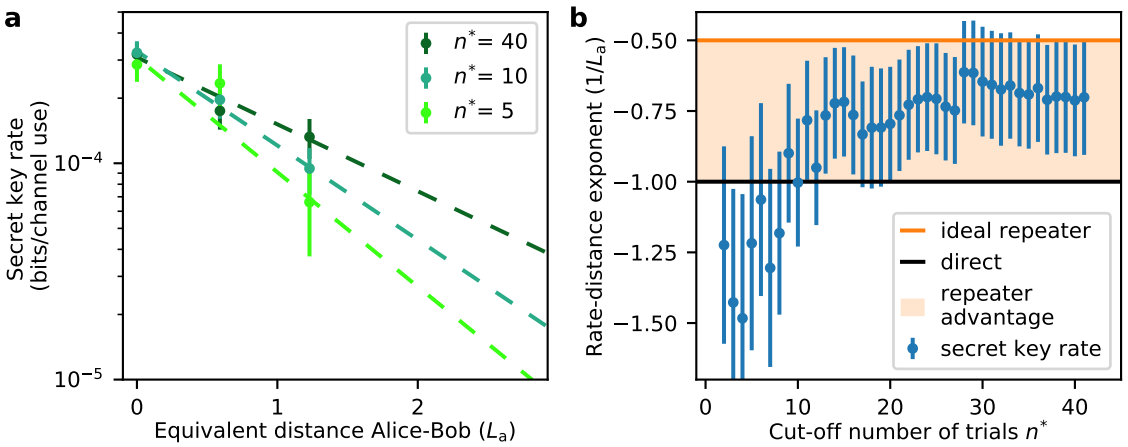

Figure 5.14.: Secret key rate analysis. **a** Rate versus equivalent distance for different cut-offs in number of trials n^*. **b** Slope of linear fits to the data presented in (a).

reason for the worse performance compared to the results of the yield is the increase in QBER and thus decay in r_S with increasing distance. This also poses the final limitation to the scalability of the quantum repeater as, eventually, r_S will decrease faster than the repeater advantage can compensate. Here however we managed to maintain a sufficiently good QBER so that this is not yet the case. We do want to mention that this behavior could also be achieved artificially by worsening the QBER for small distances on purpose which could even lead to a rate-distance exponent better than the ideal repeater scenario. As the QBER in our implementation increases with distance, this unphysical behavior is obviously not present. It just highlights again that there are many possibilities to falsifying results and that care has to be taken when analyzing them. In the end, only the demonstration of a secret key rate which unconditionally beats direct transmission will be free of doubt.

For better comparability to a direct-transmission system, we here want to give a summary of additional contributors to the key-rate which have been introduced over the course of this chapter. First, on average only 43 % of the acquired data survive the image postselection. In Sec. 5.4.1, we have described that we only use cases where the number of channel usages is smaller than 40, which gives an additional factor of on average 0.83. In the same section, we have introduced that the experiment runs with a duty cycle of on average 0.2. These three contributions lead to a bias in the observed key distribution rate of $c_{\mathrm{kgr}} = 0.43 \times 0.83 \times 0.2 \approx 0.07$ which has to be considered when investigating the real-world performance. Additionally, all key rates so far have been given in units of bits per channel use as it became a community standard and allows for better comparisons between different experimental approaches. In our case, converting this to a rate in bits per time is counterintuitive, as it does not depend on the transmission distance. Indeed, due to the repeat-until-success strategy, basically every experimental run is successful. Together with a fixed experimental repetition rate, the real-time yield is given by the BSM efficiency and the experimental repetition rate, giving

$$p_{\mathrm{BSM}} \times \Gamma_{\mathrm{exp}} \times c_{\mathrm{kgr}} \approx 0.05 \frac{\mathrm{bits}}{\mathrm{attempt}} \times 160 \frac{\mathrm{attempts}}{s} \times 0.07 = 0.56 \frac{\mathrm{bits}}{s}. \tag{5.15}$$

In even more realistic implementations, this rate will be distance-dependent as the maximum number of repetitions will be limited which results in a probabilistic repeat-until-success and also the experimental repetition rate should be dynamic.

5.5. Current limitations and future improvements for repeater rates

As we have seen in the last section, the acquired data for the raw key rate matches nicely to theory. This allows to analyze current limitations and make predictions on which measures would improve by how much the achievable raw and secret key rates.

Raw key rate

Not taking into account the limited and decaying fidelities, the raw key rate is only bounded by the Bell-state measurement efficiency (p_{BSM}) and the number of trials $N_{\mathsf{A}}, N_{\mathsf{B}}$ which are necessary to establish a key at a certain distance.

Figure 5.15 shows the raw key rate when either attributing all the losses to the communication channel (effective distance, a) or when only accounting the additionally added losses to the communication channel (equivalent distance, b). Note that the latter was used for the presentation of the results above. The blue-shaded region shows the current maximum distance limited by the maximum average number of trials $\mathsf{max}(\langle N \rangle) = 9$. This number of trials equals a maximum total loss. Depending on which partial losses are attributed to distance, this leads to different maximum communication distances. In the current configuration (blue shaded region) the direct transmission could be beaten in the effective-distance scenario when improving the BSM efficiency to about $p_{\mathsf{BSM}} \approx 0.2$ or when increasing the average number of trials to 30. In the equivalent-distance scenario, the BSM would need to be deterministic, or the average number of trials would need to be increased to about 140.

In the current scheme, improving the BSM in the raw-key-rate scenario will be challenging. While the so-called „efficient BB84“ scenario [158] can nearly double the raw key rate, this advancement would also need to be considered for the direct-transmission case. For measurements in the Z-basis, potentially also BSMs yielding $|\Phi^{\pm}\rangle$ could be used, as for the Z-basis, the distinction between $|\Phi^{+}\rangle$ and $|\Phi^{-}\rangle$ is not necessary. However, the validity of security proofs would need to be reconsidered, as the QBER cannot be verified for X-basis measurements with these BSM results.

Even the change to an in-principle deterministic BSM using a two-atom gate [66] in combination with a true single-photon source probably does not improve much, as also these schemes suffer from non-perfect single-photon sources ($\eta \approx 0.6$), photon detection ($\eta \approx 0.7$), reflection from the atom-cavity system ($\eta \approx 0.55$) and losses in optical elements like optical circulators ($\eta \approx 0.6$), resulting in a best-case efficiency of $\eta \approx 0.14$ which would be an improvement of factor 3. A significant improvement could only be reached by finding a truly deterministic BSM.

Neglecting cross talk and infidelities, the maximum number of trials on the two atoms

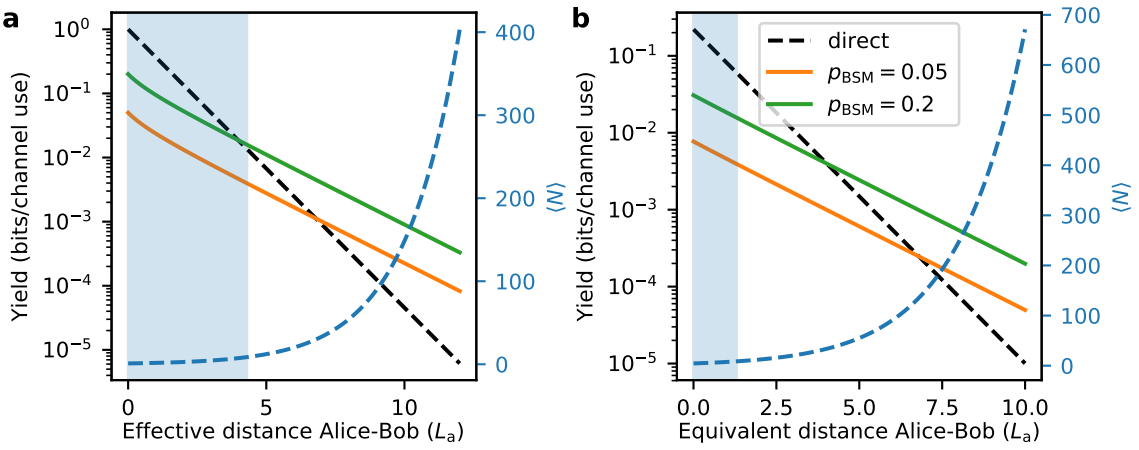

Figure 5.15.: Raw key rate for direct transmission and quantum repeater The rate is compared between direct transmission and a single repeater node with different Bell-state measurement efficiencies p_{BSM}. **a** Attributing all losses to the transmission channel. **b** Only attributing simulated losses to distance as we have also done for the experimental results presented in this thesis. The blue-shaded region shows the maximum average number of trials (9) currently usable in our setup.

is currently limited by heating of the atoms which leads to significantly reduced atom trapping times with increasing number of trials. There are three ways to improve this, either increasing the trap depths so that more heating is acceptable, or improving the atom cooling so that heating is compensated, or reducing the heating caused by every trial. Starting with the last option, this could be achieved by „re-pumping“ the atom from $|F = 1\rangle$ to $|F = 2\rangle$ via a coherent process, such as a STIRAP or a stimulated Raman transition. These would need to be Zeeman-selective to not empty the targeted final dark state $|F = 2, m_F = 0\rangle$ which is at least partly possible by using magnetic-field-induced frequency and polarization selection rules. Improving the cooling has been tried by many PhD generations but is still an open challenge which would definitely be worth tackling again. Increasing the trap depths in the current setup is possible but comes at costs which have been discussed in Sec. 5.3.2. Alternatively, new trapping techniques can be used which might remedy some of these costs [72].

Secret key rate

For the ultimate goal of beating direct transmission in secret key rate, fidelities or QBERs have to be considered. Currently these give a secret key fraction of about 10 %, which means that the advantage against direct transmission has to be increased by the same amount (Fig. 5.15).

So far, the limited coherence time, re-trial-induced cross talk and detector dark counts have been neglected. As this increases the parameter space significantly, not all aspects can be discussed. We will thus just give an overview of the most likely scenarios.

Figure 5.16 shows the rate-distance behavior for the parameters obtained in this thesis (see App. F) and for parameters which might be attainable in the future. For the secret key rate, even the direct transmission has a maximum distance at which the rate decays

abruptly due to detector dark counts increasing the QBER. This limitation only appears later for the repeater case, as every sub-link has a significantly higher success probability. For the repeater, the main limitation is its starting fidelity and its coherence time. Here we defined coherence time as the decay in fidelity for the repeater application, thus it also involves cross talk per trial. One conclusion from the simulation presented in this Figure is, that direct transmission cannot be beaten with the current parameter set for any distance, neither in the „equivalent distance“ nor in the „effective distance“ scenario. Significant improvements would involve doubling the coherence time, doubling the BSM efficiency and improving the overall starting fidelity by 2 pp, either by improving the atom-photon entanglement process or by improving the Bell-state measurement. Combined, these measures would allow to beat the direct transmission in both loss scenarios. Note that it becomes harder to beat direct transmission if dark counts would be reduced as the repeater does not run into the dark-count limitation yet. In any case, the number of maximum repetitions will need to be increased significantly, as the direct transmission can only be beat for on average $100 - 200$ trials, depending on the loss scenario.

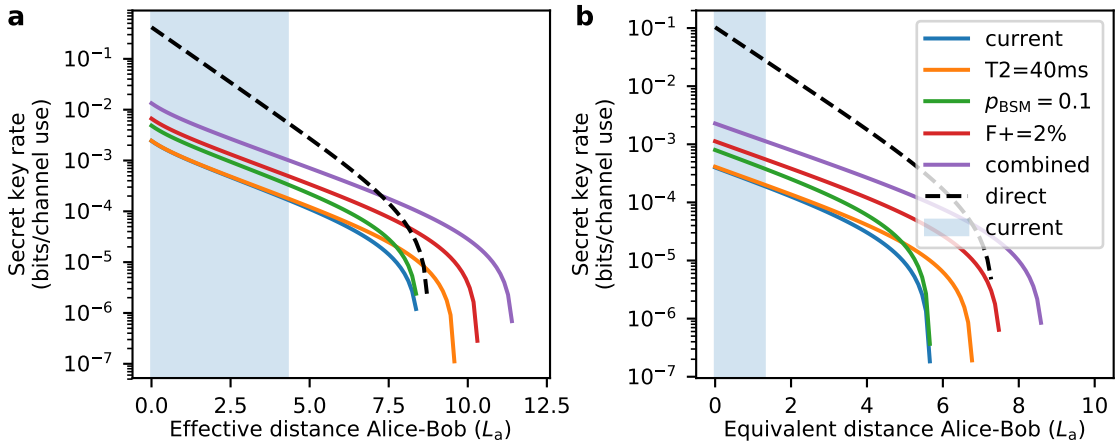

Figure 5.16.: Secret key rate obtainable with direct transmission and with a single repeater node assuming a variety of parameters. Just like Fig. 5.15, (a) and (b) show the rate when attributing all losses to distance or only considering additional losses, respectively. Compared to Fig. 5.15 rates are reduced by a factor of 2 because two modes per trial are necessary for establishing a secret key. Coherence time assumes that there is no other decoherence mechanism like cross talk which depends on time or number of trials. The parameters used in the simulation are detailed in App. F.

Improvements in fidelity might be expected by performing the photon production processes at the D_1 line of ^{87}Rb, as the larger hyperfine splitting of this excited state manifold should lead to less scattering and cycling [84] at the cost of reduced efficiency though. Another source of infidelity is the „remapping“ Raman. Alternative schemes involving other Raman transitions have been considered but no obvious better solution could be found. A possible solution would be using microwave instead of Raman transitions if a future upgrade to the experiment enables high-Rabi-frequency microwave transitions. After all, a second cavity could help so that no „remapping“ is necessary at all (App. C).

The coherence time is currently mostly limited by the employed dynamical decoupling se-

quence and by cross talk induced by the repumping light field which is applied through the addressing system. The former was discussed in Ch. 4 and should be straight forward to be improved. The latter would require another iteration of improving the spatial addressing profile, probably in combination with optical tweezers for deterministic positioning at a certain interatomic distance.

One major drawback of the current scheme or rather the current level of understanding is the limited usable time difference of the two BSM photons in the X-basis detection, see Sec. 5.4.3. Solving this issue would increase the secret-key-rate in this basis by a factor of $4-5$. However, this effect is not considered in Fig. 5.16 and would need to be addressed additionally. Other possibilities for increasing the BSM efficiency have been discussed above already.

5.6. Summary and outlook

We have realized a quantum repeater node for quantum key distribution that beats the rate-versus-distance scaling of direct transmission. We have achieved the necessary quantum bit error rates to proof unconditional security against any possible attack by adversary eavesdroppers. The core achievements towards this goal were, first, the implementation of a repeat-until-success atom-photon entanglement generation which is fast and has high fidelity. Second, the long-lived preservation of the entanglement via dynamical decoupling and third, a high-fidelity Bell-state measurement.

The outlook on achieving higher rates including opportunities for higher fidelities has already been given in the last section. However, there are additional avenues for future research. Most importantly, research should be directed in transitioning from quantum key distribution to long-distance entanglement distribution. To this end, quantum end-nodes are necessary which utilize heralded qubit memories instead of classical photon detectors, just like recently demonstrated in a neighboring laboratory [62]. Their heralding efficiency of $11\,\%$ matches a $90\,\%$ loss scenario and thus would require a five-fold increase in maximum number of trials or improvements in the heralding efficiency, e.g. by using superconducting single photon detectors. Their achieved process fidelity of $95-98\,\%$ in combination with the achieved QBER in this thesis should already be enough to beat the CHSH inequality [24] limit of $\mathcal{F} \geq 86\,\%$, however it might require atomic readout of the stored qubit for higher data rates. The biggest experimental obstacle is probably the trapping time and resulting duty cycle of four simultaneously trapped atoms, which has been discussed previously in this thesis. The same obstacle exists for the pathway of increasing the number of qubits within the repeater node. The goal of this would be to implement entanglement distillation after multiple entangled pairs have been created, very much following the seminal proposal by Briegel et al. [35]. To this end, of course, an efficient distillation scheme would be necessary. While multi-qubit gates, the core ingredient to distillation, have been demonstrated for atoms within a cavity [66], their efficiency and fidelity currently does not allow for scaling to many operations. The most promising avenue for implementing high-fidelity gates on neutral atoms seems to be utilizing Rydberg states [159]. The combination of cavity QED for atom-photon interactions and Rydberg excitations for atom-atom interactions thus seems a promising research opportunity.

Alongside these fundamental research opportunities, also technological issues should be tackled. The most obvious disadvantage of the current implementation is certainly the combination of Alice, Bob and the optical BSM in a single detection setup. For demonstrations in the field, the development of high-fidelity and fast switches for single photon polarization qubits are necessary. While there are some commercial options, none of them have shown to fulfill our demands. Thus, the development and potential commercialization of these switches would be a valuable contribution for our laboratory and also the community. Another inconvenience of the current implementation is the overall stability and supervision necessary to obtain consistent and high-quality results. For example, in the current implementation, the exact timing of the atom-photon entanglement attempts needed to be retuned about every hour, so that Alice and Bob's qubits are properly in phase. To this end, better passive and potentially also active stabilization of beam pointings and powers would be a valuable improvement. Similarly, while the implemented feedforward on the magnetic field largely compensates AC fluctuations, mu-metal shielding could improve the DC stability of magnetic fields which also contribute to the accurateness of rephasings.

6. Summary and outlook

In this thesis, we have realized the evolution from a single atom inside a high-finesse optical cavity for quantum information processing to multiple, individually usable atoms within the same cavity. To this end, we have identified the fundamental processes leading to cross talk between the individual atoms. By optimizing the experimental setup and choosing experimental parameters carefully, we could reduce cross talk to a negligible level and thus make the transition from 1 to n atoms. Further scaling beyond the experimentally implemented $n = 2$ is now mostly technological. Especially crucial for reducing cross talk are two mechanisms. First, classical light fields need to be focused onto individual atoms with as little as possible cross-illumination. This we achieved by the combination of a high numerical aperture objective and an acousto-optical deflector for steering the beam to the target atom. At the same time, the atomic positions need to be chosen so that the still finite beam size interacts only with a single atom, eventually limited by the size of the cavity. Second, although both atoms are in-principle coupled to the cavity, quantum light fields in the cavity mode should only interact with the target atom. To this end, incoherent processes which act on all atoms have to be minimized. This is achieved by detuning the cavity from the atomic resonance while developing quantum processes which also work reliably at these elevated detunings.

Having minimized these unwanted effects, already with two atoms, we could extend the single-atom qubit memory developed in this group to a random-access two-qubits memory. We could largely maintain the performance of the single-atom implementation, i.e. a combined write-read efficiency of $26\,\%$, fidelities of about $96\,\%$ and a coherence time approaching $1\,\mathrm{ms}$. We have demonstrated multiple random-access patterns and handled up to 11 individual photonic qubits in a single experiment, with still negligible cross talk. Although we observed basically no cross talk, the access-time to any memory of currently $40\,\mu\mathrm{s}$, limited by the AOD sound propagation time, in combination with the observed coherence time poses a limitation on how many operations can be performed on one atom, while the other atom already stores a qubit.

To overcome this limitation, we developed a novel dynamical decoupling scheme for qubits encoded in Zeeman-states of the same hyperfine manifold. This scheme extends the coherence time beyond $20\,\mathrm{ms}$ in an application-ready scenario. To this end, we implemented a stimulated Raman transition which connects states with $\Delta m_\mathrm{F} = 2$ while operating at a single-photon detuning of many THz. While this transition normally destructively interferes due to transition paths via multiple excited states, we could bypass this limitation by performing two $\Delta m_\mathrm{F} = 1$ transfers simultaneously. This Raman configuration was the enabling technology to perform up to 100 $\pi-$pulses with high fidelity.

The combination of the aforementioned achievements enabled us to experimentally demonstrate a quantum repeater for quantum key distribution for the first time. This included

the distribution of photons which are individually entangled with the two atoms in a repeat-until-success strategy. Here, the extended coherence time is important so that the two probabilistic photon transmissions can be synchronized. As the two communication parties Alice and Bob measure their arriving photons according to the seminal BB84 proposal, they each deterministically share a highly correlated state with the central repeater node. As both atoms are coupled to the same high finesse cavity, we can employ a Bell-state measurement which erases the which-atom information and swaps the correlation so that afterwards Alice and Bob share these highly correlated states which they can use to establish a cryptographic secret key. As a result of the cross talk elimination and the extended coherence time, we were able to perform high-fidelity operations which finally lead to a quantum bit error rate of below 11 %, the fundamental threshold for providing quantum key distribution which is unconditionally secure based on the laws of quantum mechanics. The motivation for quantum repeaters is beating the key distribution rate Alice and Bob would get via direct quantum communication with one another. We accomplished observing the expected rate-versus-distance scaling improvement which is fundamental to the quantum repeater operation. However, in its current implementation, we were not able to beat the direct transmission key rate in absolute numbers. Finally, we have given an extensive outlook on how the achievable absolute key rates can be improved in future implementations.

The outlook on future research opportunities can be divided into two parts. First, the development of additional tools which further advance the control in the multi-atom single-cavity platform and second, new protocols which are enabled by this level of control.

The most obvious extension of this platform is scaling to more atoms. As we have already discussed in Sec. 2.6, this can be achieved by atomic tweezers or multi-dimensional optical lattices. Most importantly, the atomic trapping time needs to be increased so that protocols involving more than two atoms, potentially also distributed over multiple cavities in a network, can be implemented reliably.

For maximum flexibility on which protocols can be implemented on multiple atoms, there are still some capabilities missing which have been implemented before on single-atom systems. Most prominently, this is the ability to perform stimulated Raman transitions on individual atoms. While we did perform coherent processes via the implemented addressing system, all of them were adiabatic. For example, the stimulated Raman configuration presented for dynamical decoupling could also be used for single qubit gates. As it operates at very large detunings, it would be sufficient to only address one of the two Raman beams onto an individual atom, while the other is applied commonly. The downside of stimulated Raman transitions is that they are more sensitive to power fluctuations and thus require an even better level of control. However, this is a purely technological effort which has been addressed before in other systems [160] and which is already in development in a neighboring laboratory.

While we have been focusing on quantum communication and quantum networks, each network node needs at least basic computation capability to fulfill the demanding requirements of the following and many other protocols. To this end, high-efficiency and high-fidelity multi-atom gates are necessary. While multi-atom gates have been demonstrated on a very similar setup [66], they neither had high fidelity nor were highly efficient.

Although the cavity offers a powerful tool for collective effects on multiple atoms, schemes employing photons will never be fully deterministic. Consequently, I believe that research should go in the direction of combining highly interactive Rydberg states with single atoms in optical cavity QED. While the Rydberg states will probably be influenced by the close-by cavity mirrors, in contrast to ions [161], this interaction can be controlled and only needs to be „on“ during a gate operation. Achieving this ability would complete the seven DiVincenzo [94] criteria and ready this platform for basically any protocol.

Instead of describing basically any protocol, we will restrict ourselves to the ones which are enabled by combining a multi-atom register with a high-finesse cavity.

A rather simple use-case is operating on multiple atoms simultaneously, by performing previously demonstrated protocols in a multiplexed fashion. This effectively increases the experimental repetition rate without duplicating the whole experimental setup.

In 1997, van Enk et al. proposed a protocol which already works with two atoms per cavity, demonstrates a small quantum network and achieves ideal quantum communication over lossy channels [108]. Here, one atom of the register is used for communication while, in a simplistic picture, the second atom is used for backups in case the transmission fails. In contrast to quantum teleportation [27], it does not rely on pre-shared entanglement and requires no complete BSM to be deterministic.

Another major step would be the realization of entanglement distillation [162, 163] which has only been demonstrated once in a network setting, though with limited success [164]. Each of the atoms would store one part of a low-fidelity entangled pair. By entanglement distillation, the number of entangled pairs is reduced but the entanglement fidelity increases. In our case, entanglement could be generated either via direct transfer of the photon of an atom-photon entangled pair, or via overlapping two photons on a beam splitter [165]. Entanglement distillation is a core ingredient to the scalable and universal quantum repeater proposal by Briegel et al. [35], and would thus elevate our implemented quantum repeater for quantum key distribution to scalable entanglement distribution.

The combination of a highly efficient atom-photon interface and atom-atom computing capabilities also offers promising avenues for the development of distributed quantum computing. For today's quantum computers, it will be difficult to significantly increase the number of qubits in a single monolithic setup, independent of its physical implementation. The connection of multiple smaller computing modules could remedy this obstacle. To this end, basically small quantum computers would be integrated into the optical cavity. These can then be combined via gate teleportation [166] or the latest achievement of our group, a non-local quantum gate [33]. While these schemes already promise universal quantum computation with two qubits per cavity only, scaling to more individually addressable atoms will be necessary to fully leverage the promised quantum advantage. Thus our work has implemented one corner stone, with more to come, for bridging the gap between quantum communication and quantum computation, which brings useful quantum networks one step closer.

A. Detailed level structure of the ^{87}Rb D_2 and D_1 lines

Here we give the AC-Stark shifts relevant for the Repeater experiment in Ch. 5. The AC-Stark shifts in Ch. 3 are so small that they can be neglected.

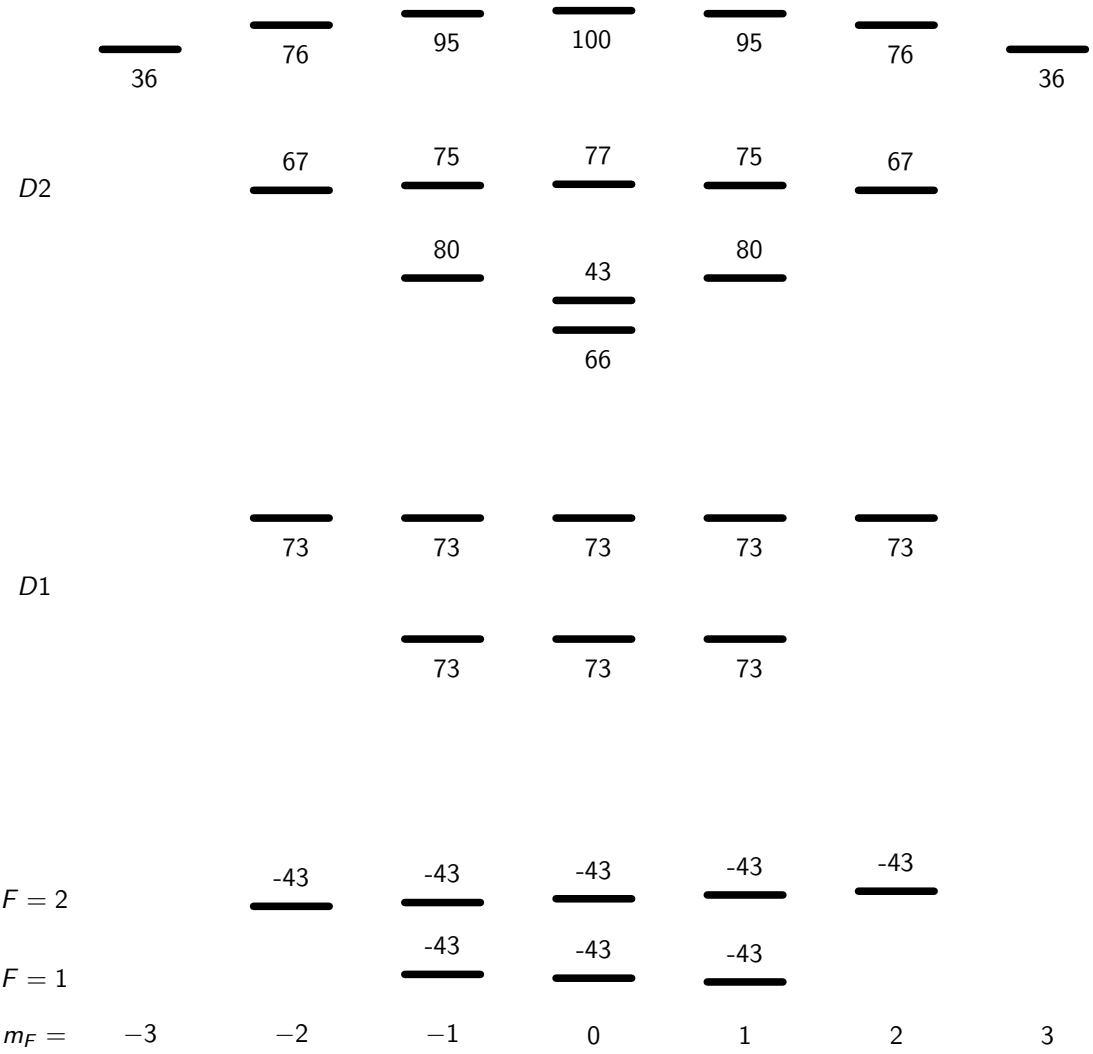

Figure A.1.: Level scheme. Numbers denote the calculated AC-Stark shift in MHz. Within the D_2 and D_1 manifolds, the shifts are depicted to scale. Additional Zeeman shifts on the order of 100 kHz are not shown.

B. Single-atom characterization experiment similar to Wilk et al. [58]

In order to test most of the components of the quantum repeater protocol, we perform a single-atom photon-photon entanglement experiment. After all, the repeater protocol essentially realizes two times photon-photon entanglement with a Bell-state measurement on two of the four photons.

The procedure is depicted in Fig. B.1. After each of the four steps, the atom-photon/photon-photon states are:

$$
\begin{aligned}
1.\ |\psi\rangle_{\mathrm{AP}} &= \frac{1}{\sqrt{2}}\left(|\uparrow R\rangle - |\downarrow L\rangle\right), \\
2.\ |\psi\rangle_{\mathrm{AP}} &= \frac{1}{\sqrt{2}}\left(|\downarrow R\rangle - e^{i\Phi}\,|\uparrow L\rangle\right), \\
3.\ |\psi\rangle_{\mathrm{AP}} &= \frac{1}{\sqrt{2}}\left(|\downarrow_{F=2} R\rangle - e^{i\Phi}\,|\uparrow_{F=2} L\rangle\right), \\
4.\ |\psi\rangle_{\mathrm{PP}} &= \frac{1}{\sqrt{2}}\left(e^{i\delta_{\mathrm{L}} t_{\mathrm{PP}}}\,|LR\rangle - e^{i\Phi - i\delta_{\mathrm{L}} t_{\mathrm{PP}}}\,|RL\rangle\right),
\end{aligned}
$$

assuming a single DD pulse imprinting a phase ϕ and accounting for the total storage time between the two photon emissions t_{PP} in the last step.

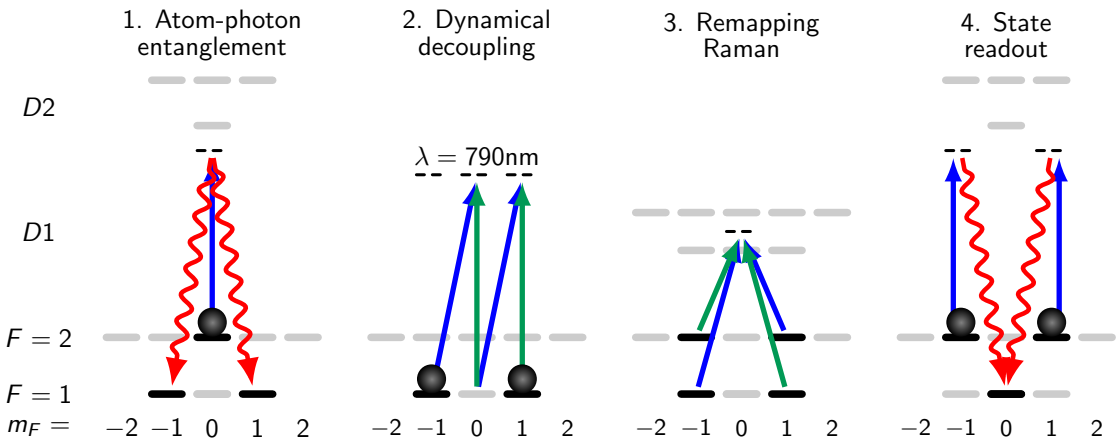

Figure B.1.: Atomic level scheme and logical order for testing major components of repeater sequence.

Then the fidelity with a given Bell state, e.g. $\left|\Psi^{+}_{\mathsf{RL}}\right\rangle$, can be measured and used for analyzing certain aspects of the scheme. The fidelity is given by:

$$\mathcal{F} = \left|\left\langle \Psi^{+}_{\mathsf{RL}} | \Psi_{\mathsf{PP}} \right\rangle\right|^2 = \frac{1}{4}\left| e^{i\delta_{\mathsf{L}} t_{\mathsf{PP}}} - e^{i\Phi - i\delta_{\mathsf{L}} t_{\mathsf{PP}}} \right|^2 = \frac{1}{2}\left(1 - \cos(\phi - 2\delta_{\mathsf{L}} t_{\mathsf{PP}})\right). \tag{B.1}$$

Thus this allows to investigate the distribution of $\delta_{\mathsf{L}} t_{\mathsf{PP}}$ as well as the impact of ϕ introduced by the decoupling pulses.

In addition to investigating the fidelity, it also can be used for testing the efficiency of individual processes such as the initial state preparation, the remapping efficiency or the photon production in step 4 after the heralded state preparation by the photon in step 1.

C. Additional repeater level schemes

Here we present additional ideas for which atomic level schemes could or could not have been used for the repeater protocol. Generally, the motivation was to increase the fidelity via high-fidelity operations or to ease state preparation by having the initial state in $|F = 1\rangle$.

One promising possibility for increasing the overall fidelity is to replace the „remapping Raman“. To this end, only high-fidelity Raman operations should be involved, which are limited to $\Delta m_F = \pm 1$ transfers. One option uses a $\sigma^{\pm}$-STIRAP which unfortunately does not work as is displayed in Fig. C.1. The reason is that the two arms of the $\sigma^{\pm}$-STIRAP can also drive two-photon transitions within $|F = 2\rangle$. Another option we considered is using a time-bin encoding for the readout photons. Typically, measuring time-bin photonic qubits is experimentally challenging, as the two components of the time-bin need to be overlapped in an interferometer. However, as the BSM only needs to measure in one detection basis, e.g. $(|\uparrow_z\rangle, |\downarrow_z\rangle)$, measuring early ($|e\rangle$) and late ($|l\rangle$) individually would have been easily possible. The tricky part is then to map the atomic states $|F = 1, m_F = \pm 1\rangle$ to $|e\rangle$ and $|l\rangle$, which is depicted in Fig. C.2. While the scheme only uses high-fidelity $\Delta m_F = \pm 1$ transfers, it requires a total of five of them. Due to its complexity, we did not

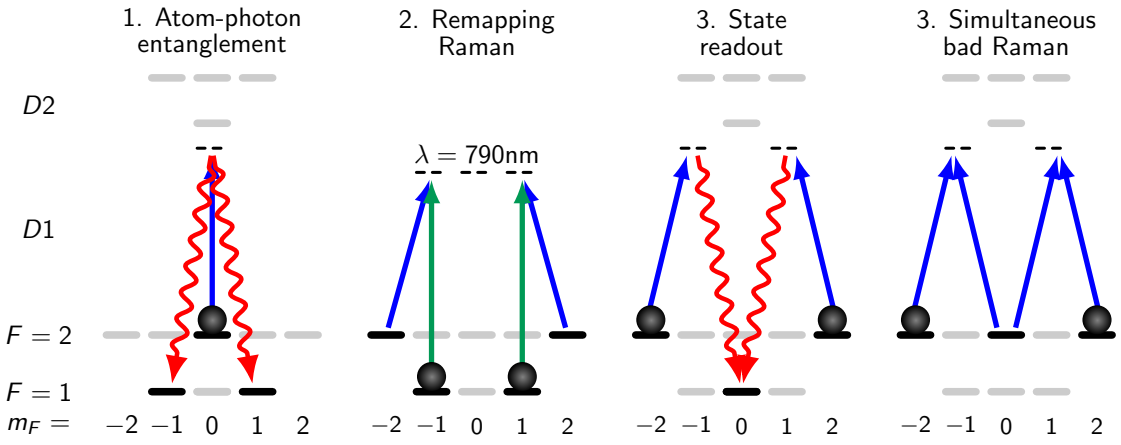

Figure C.1.: Only using high-fidelity gate operations. Here, the idea was to only use high-fidelity intermediate remapping Ramans so that the overall fidelity can be improved. To this end, we employed a far-detuned $\Delta m_F = \pm 1$ transfer which also maps from $|F = 1\rangle$ to $|F = 2\rangle$. As the readout STIRAP has to end in the same final state for both atomic states, a $\sigma^{\pm}$-STIRAP control beam was supposed to bring the population back to $|F = 1, m_F = 0\rangle$. Unfortunately, this control beam also drives intra-hyperfine transitions via $|F = 2, m_F = 0\rangle$. While this can be avoided by increasing magnetic fields and making the photon longer (both effects increase Zeeman selectivity), we ran simulations and verified experimentally that this never results in a sufficient fidelity.

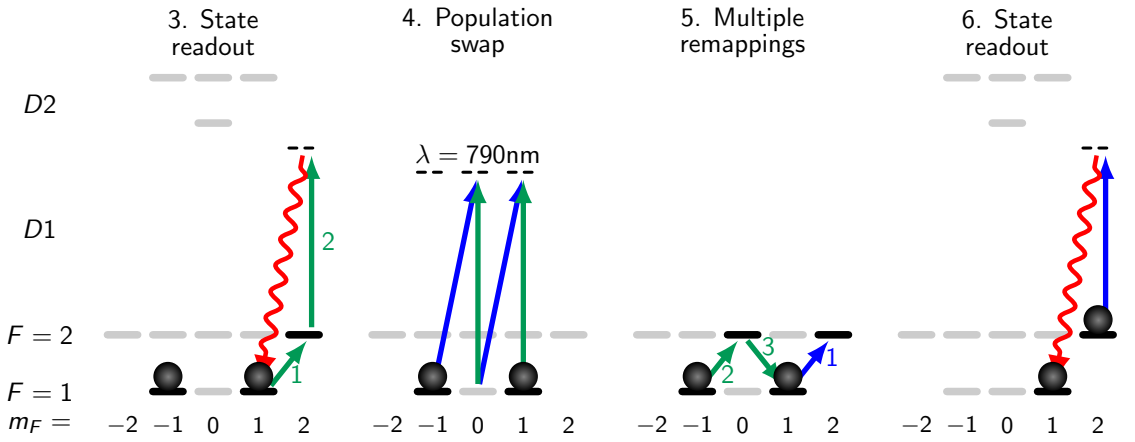

Figure C.2.: Using time-bin photonic qubits. We skip displaying the usual atom-photon entanglement and dynamical decoupling step. In order to produce time-bin photons and leave no information on the atom, the final state of the atom has to be independent of its initial state. 3. In the early-bin ($|e\rangle$) generation, $|1,1\rangle$ is first transferred to $|2,2\rangle$ which afterwards produces a photon. 4. The two populations are swapped. 5. Similar to (3.), $|1,1\rangle$ is transferred to $|2,2\rangle$. $|1,-1\rangle$ is transferred selectively to $|1,1\rangle$ so that both atomic initial states lead to the final state $|1,1\rangle$. 6. The late-bin photon ($|l\rangle$) is produced. Green arrows act on the early time-bin qubit, blue arrows act on the late time-bin qubit, except of step (4) where they act on both.

try this scheme experimentally. Additionally, it is not clear whether the phase of atomic superposition qubits is transferred correctly to the generated time-bin photon. Although the photon would be analyzed only in its eigenbasis, the phase might still be important for the Bell-state selection of the BSM.

The final state of any protocol can never be in the $|F=2\rangle$ manifold, because atomic excited states in $|m_F=0\rangle$ can decay to multiple ground states ($|F=2, m_F=\{0,\pm 2\}\rangle$) while still emitting into the $\sigma^{\pm}$ cavity modes, thus the cavity needs to be resonant starting from $|F=1\rangle$. At the same time, the initial and the final state of a STIRAP should always be far-detuned to automatically stop the process after a single photon. The combination of these two effects makes it impossible to use $|F=1, m_F=0\rangle$ as the initial state when using only one cavity. Figure C.3 shows a potential scheme using two separately tunable cavity modes, which has additional benefits. This scheme does not need remapping between $|F=1\rangle$ and $|F=2\rangle$. It can use state initialization in $|F=1\rangle$, where Zeeman pumping is significantly easier. Additionally it uses two separate cavities for the long-distance transmission to Alice/Bob and the local detection (BSM), so that there is less need for a photon switch. We simulated the dynamical decoupling in $|F=2\rangle$, and it should work just the same way. As a side remark, the single-photon detunings would have to be chosen differently, so that only one cavity is in two-photon resonance at any given time.

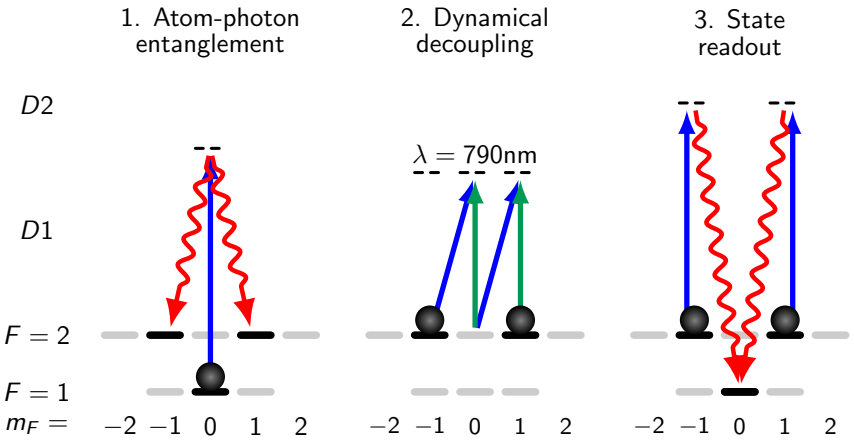

Figure C.3.: Potential future scheme with two cavities. The first cavity is used for atom-photon entanglement and is resonant starting from $|F = 2\rangle$. The second cavity is used for atom-readout, and is resonant starting from $|F = 1\rangle$.

D. Electronics used in repeater project for dynamic experimental sequence

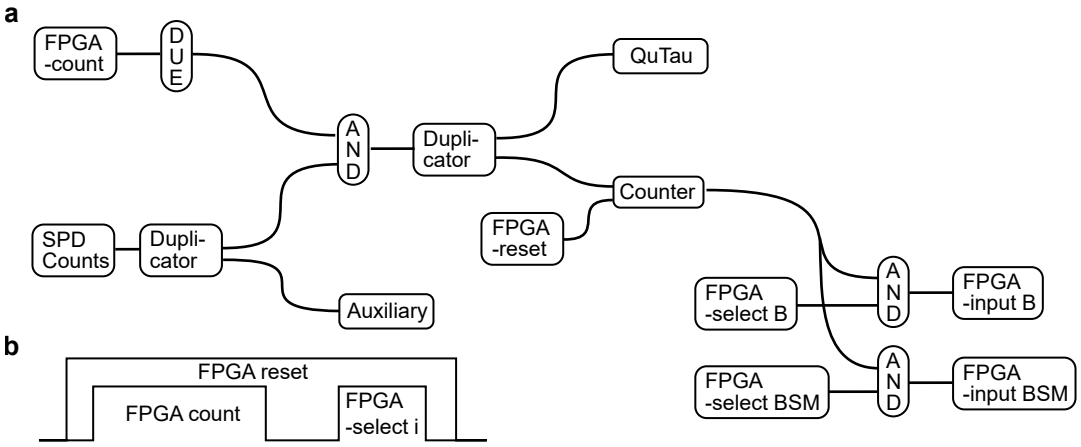

Figure D.1.: Electronics for quantum repeater protocol. a Wiring of the components for dynamically running the repeater sequence based on photon clicks. A microcontroller (Arduino DUE) is used to generate random numbers. Based on a biased coin flip, the microcontroller gates the single photon detector (SPD) counts via an AND-gate. As all signals are 50 Ohm terminated, duplicators have to be used to direct the signal to different components. A time-to-digial converter (QuTools QuTau) records the timestamps of the photon clicks which are attributed to Alice, Bob or the optical BSM. The counter counts until 1, which is when it outputs a signal to enable the AND-gates leading to external sequence selectors of the FPGA. **b** Timing sequence of the FPGA elements used in (a). First, the FPGA resets the photon counter. Afterwards, the counting is enabled only for the time in which photons are expected, which effectively reduces dark counts. The FPGA-select for actually triggering the next sequence is run independently of the photon arrival time at a fixed timing, so that there is no jitter in the run-time of the sequences. The pulse heights are different only for illustrative purposes.

E. Additional QBER investigations

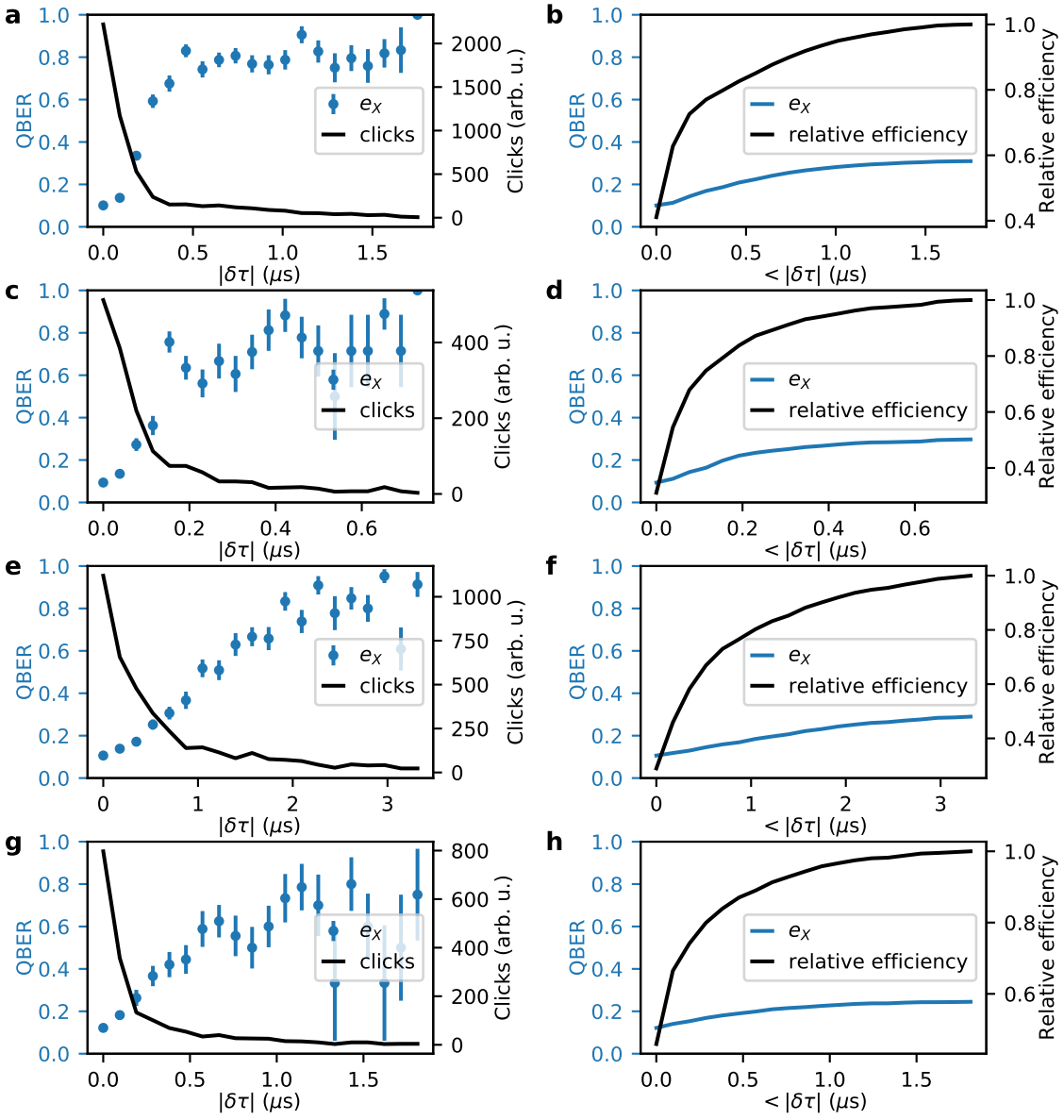

Figure E.1.: Additional measurements for BSM investigation. **a & b** $\Delta_{ac}/2\pi = -150\,\mathrm{MHz}$. **c & d** $\Delta_{ac}/2\pi = -150\,\mathrm{MHz}$, shorter readout photon. **e & f** $\Delta_{ac}/2\pi = -150\,\mathrm{MHz}$, longer readout photon. **g & h** $\Delta_{ac}/2\pi = 28\,\mathrm{MHz}$. (b, d, f, h) shows the integrated results of (a, c, e, g), respectively.

Additionally to the final results presented in the main text, Fig. E.1 shows measurements of the quantum bit error rate (QBER) for different experimental parameters.

One result which was used in the main text (Eq. (5.14)) is the combination of two photon-photon entanglement experiments which basically form the heart of the repeater protocol. Here we will briefly derive the aforementioned equation. We will assume a perfect Bell-state measurement and uncorrelated infidelities for the two separate entanglement processes. The photon-photon state is given by:

$$\rho_{\mathrm{pp,i}} = p_i \left|\psi^+\right\rangle \left\langle\psi^+\right| + \frac{1-p_i}{4}\mathbb{I}_4, \tag{E.1}$$

where $i = A,B$ is an indicator for the different atoms and p_i is connected to the photon-photon entangled state fidelity via:

$$\mathcal{F}_i = \left\langle\psi^+\right| \rho_{\mathrm{pp,i}} \left|\psi^+\right\rangle = \frac{1+3p_i}{4}. \tag{E.2}$$

Next, we combine A(lice) and B(ob) to the four-qubit product state:

$$\rho_{\mathrm{pppp}} = \rho_{\mathrm{pp,A}} \otimes \rho_{\mathrm{pp,B}}. \tag{E.3}$$

Here, the first qubit is atom A, the second is Alice, the third is atom B and the fourth is Bob. At this point, just looking at Alice and Bob, the density matrix is the completely mixed state:

$$\rho_{\mathrm{AB}} = \frac{1}{4}\mathbb{I}_4. \tag{E.4}$$

Next we measure the two atomic qubits within the repeater station in the Bell basis. To do so, we apply a controlled NOT-gate (the control is atom A and the target is atom B) and project the two atomic qubits to a specific state. Without loss of generality, we choose one of the four possible outcomes ($|\uparrow_x\uparrow_z\rangle$), which results in the two-qubit density matrix for Alice and Bob:

$$\rho_{\mathrm{AB}} = \frac{1}{4}\begin{pmatrix} 1-p_Ap_B & 0 & 0 & 0 \\ 0 & 1+p_Ap_B & -2p_Ap_B & 0 \\ 0 & -2p_Ap_B & 1+p_Ap_B & 0 \\ 0 & 0 & 0 & 1-p_Ap_B \end{pmatrix}. \tag{E.5}$$

Assuming the same fidelity for both single photon-photon entangled states ($p_A = p_B$), the (in)fidelity with the Bell state is then given by:

$$\mathcal{F} = \frac{1}{3}(1 - 2\mathcal{F}_i + 4\mathcal{F}_i^2), \tag{E.6}$$

$$e = 1 - \mathcal{F} = \frac{2}{3}(1 + \mathcal{F}_i - 2\mathcal{F}_i^2). \tag{E.7}$$

F. Details on simulation for quantum repeater

Here we give a brief overview how the formulas derived in Luong et al. [75] have been used to obtain the simulation results in Sec. 5.5.

Luong et al. define the coherence time T_2 via a dephasing channel on the input density matrix ρ:

$$\rho' = (1 - \lambda_{\mathsf{dp}})\rho + \lambda_{\mathsf{dp}}\sigma_3\rho\sigma_3, \tag{F.1}$$

$$\lambda_{\mathsf{dp}} = \frac{1 - e^{-t/T_2}}{2}. \tag{F.2}$$

Note that this assumes $\mathcal{F}(t = 0) = 1$. For a linear polarization input this gives:

$$\rho = \frac{1}{2}\begin{pmatrix} 1 & 1 \\ 1 & 1 \end{pmatrix} \to \rho' = \begin{pmatrix} 1/2 & e^{-t/T_2} \\ e^{-t/T_2} & 1/2 \end{pmatrix}, \tag{F.3}$$

$$\mathcal{F} = \langle \Psi | \rho' | \Psi \rangle = 1 - \lambda_{dp} = \frac{1 + e^{-t/T_2}}{2}. \tag{F.4}$$

Although our results in fidelity do not follow an exponential, comparing the $1/e$ value gives $T_2 \approx 20\,\mathsf{ms}$. However, in our situation, this dephasing channel applies to qubits prepared in the X- as well as the Z-basis, as the dephasing is mostly given by imperfections of the dynamical decoupling pulses. We thus modify the theory so that also $e_Z = e_X(t)$ decays with time. Note that by choosing $T_2 = 20\,\mathsf{ms}$, we neglect any additional cross talk which would also scale with time/number of retrials.

Next we consider the reduced starting fidelity of the atom-photon entanglement as well as the Bell-state measurement fidelity. While the authors do not consider a reduced starting fidelity, we absorb all static, i.e. time-independent, infidelities in the BSM fidelity. This has also practical reasons, as we can not quantify the BSM fidelity on its own. For approximately matching our experimental results on the obtained QBER, we get $\mathcal{F}_{\mathsf{BSM}} = 0.94$.

Parameters which we use are:

- preparation time $T_p = 10\,\mu\mathsf{s}$
- preparation success $\eta_p = 0.66$
- detection efficiency $\eta_d = 0.68$
- atom-fiber generation/coupling efficiency $\eta_c = 0.55$
- attenuation length $L_a = 1.1\,\mathsf{km}$

- dark count rate $\Gamma_{\mathsf{dc}}/\mathsf{detector} = 20\,\mathsf{Hz}$
- detection window $\delta t = 0.5\,\mu\mathsf{s}$.

Bibliography

[1] Planck, M. *Zur Theorie des Gesetzes der Energieverteilung im Normalspectrum. Verhandlungen der deutschen physikalischen Gesellschaft* **2**, 237 (1900).

[2] Young, T. *II. The Bakerian Lecture. On the theory of light and colours. Philosophical Transactions of the Royal Society of London* **92**, 12 (1802).

[3] Maxwell, J. C. *VIII. A dynamical theory of the electromagnetic field. Philosophical Transactions of the Royal Society of London* **155**, 459 (1865).

[4] Einstein, A. *Über einen die Erzeugung und Verwandlung des Lichtes betreffenden heuristischen Gesichtspunkt. Annalen der Physik* **322**, 132 (1905).

[5] Planck, M. The Nobel Prize in Physics 1918. https://www.nobelprize.org/prizes/physics/1918/planck/lecture/ (1918).

[6] Einstein, A. The Nobel Prize in Physics 1921. https://www.nobelprize.org/prizes/physics/1921/summary/ (1921).

[7] Bohr, N. *On the constitution of atoms and molecules I. The London, Edinburgh, and Dublin Philosophical Magazine and Journal of Science* **26**, 1 (1913).

[8] De Broglie, L. *Recherches sur la théorie des quanta.* Ph.D. Thesis, Migration-université en cours d'affectation (1924).

[9] Einstein, A., Podolsky, B. & Rosen, N. *Can Quantum-Mechanical Description of Physical Reality Be Considered Complete? Physical Review* **47**, 777 (1935).

[10] Heisenberg, W. *Über den anschaulichen Inhalt der quantentheoretischen Kinematik und Mechanik. Zeitschrift für Physik* **43**, 172 (1927).

[11] Schrödinger, E. *Die gegenwärtige Situation in der Quantenmechanik. Die Naturwissenschaften* **23**, 807 (1935).

[12] Feynman, R. P. *Simulating physics with computers. International Journal of Theoretical Physics* **21**, 467 (1982).

[13] Dowling, J. P. & Milburn, G. J. *Quantum technology: the second quantum revolution. Philosophical transactions. Series A, Mathematical, physical, and engineering sciences* **361**, 1655 (2003).

[14] European-Consortium. Quantum Manifesto (2016).

[15] Arute, F. *et al. Quantum supremacy using a programmable superconducting processor. Nature* **574**, 505 (2019).

[16] Cho, A. *IBM promises 1000-qubit quantum computer—a milestone—by 2023. Science* (2020).

[17] Gibney, E. *Quantum computer race intensifies as alternative technology gains steam. Nature* **587**, 342 (2020).

[18] Georgescu, I. M., Ashhab, S. & Nori, F. *Quantum simulation. Reviews of Modern Physics* **86**, 153 (2014).

[19] Degen, C. L., Reinhard, F. & Cappellaro, P. *Quantum sensing. Reviews of Modern Physics* **89**, 035002 (2017).

[20] Wootters, W. K. & Zurek, W. H. *A single quantum cannot be cloned. Nature* **299**, 802 (1982).

[21] Wiesner, S. *Conjugate coding. ACM SIGACT News* **15**, 78 (1983).

[22] Bennett, C. H. & Brassard, G. Quantum Cryptography: Public Key Distribution and Coin Tossing. In *Proceedings of the IEEE International Conference on Computers, Systems and Signal Processing*, 175 (New York, 1984).

[23] Schrödinger, E. *Discussion of Probability Relations between Separated Systems. Mathematical Proceedings of the Cambridge Philosophical Society* **31**, 555 (1935).

[24] Clauser, J. F., Horne, M. A., Shimony, A. & Holt, R. A. *Proposed Experiment to Test Local Hidden-Variable Theories. Physical Review Letters* **23**, 880 (1969).

[25] Aspect, A., Dalibard, J. & Roger, G. *Experimental Test of Bell's Inequalities Using Time-Varying Analyzers. Physical Review Letters* **49**, 1804 (1982).

[26] Ekert, A. K. *Quantum cryptography based on Bell's theorem. Physical Review Letters* **67**, 661 (1991).

[27] Bennett, C. H., Brassard, G., Crépeau, C., Jozsa, R., Peres, A. & Wootters, W. K. *Teleporting an unknown quantum state via dual classical and Einstein-Podolsky-Rosen channels. Physical Review Letters* **70**, 1895 (1993).

[28] Kimble, H. J. *The quantum internet. Nature* **453**, 1023 (2008).

[29] Wehner, S., Elkouss, D. & Hanson, R. *Quantum internet: A vision for the road ahead. Science* **362**, eaam9288 (2018).

[30] Buhrman, H. & Röhrig, H. Distributed quantum computing. In *International Symposium on Mathematical Foundations of Computer Science*, 1 (Springer, Berlin, Heidelberg, 2003).

[31] Monroe, C., Raussendorf, R., Ruthven, A., Brown, K. R., Maunz, P., Duan, L.-M. & Kim, J. *Large-scale modular quantum-computer architecture with atomic memory and photonic interconnects. Physical Review A* **89**, 022317 (2014).

[32] Brown, K. R., Kim, J. & Monroe, C. *Co-designing a scalable quantum computer with trapped atomic ions. npj Quantum Information* **2**, 16034 (2016).

[33] Daiss, S., Langenfeld, S., Welte, S., Distante, E., Thomas, P., Hartung, L., Morin, O. & Rempe, G. *A Quantum-Logic Gate between Distant Quantum-Network Modules. in preparation* (2020).

[34] Nielsen, M. A. & Chuang, I. L. *Quantum Computation and Quantum Information* (Cambridge University Press, 2000).

[35] Briegel, H. J., Dür, W., Cirac, J. I. & Zoller, P. *Quantum Repeaters: The Role of Imperfect Local Operations in Quantum Communication. Physical Review Letters* **81**, 5932 (1998).

[36] Liao, S.-K. *et al. Satellite-to-ground quantum key distribution. Nature* **549**, 43 (2017).

[37] Main, D. Undersea Cables Transport 99 Percent of International Data. https://www.newsweek.com/undersea-cables-transport-99-percent-international-communications-319072 (2015).

[38] Maiman, T. H. *Stimulated Optical Radiation in Ruby. Nature* **187**, 493 (1960).

[39] Cohen-Tannoudji, C. N. *Nobel Lecture: Manipulating atoms with photons. Reviews of Modern Physics* **70**, 707 (1998).

[40] Phillips, W. D. *Nobel Lecture: Laser cooling and trapping of neutral atoms. Reviews of Modern Physics* **70**, 721 (1998).

[41] Chu, S. *Nobel Lecture: The manipulation of neutral particles. Reviews of Modern Physics* **70**, 685 (1998).

[42] Haroche, S. *Nobel Lecture: Controlling photons in a box and exploring the quantum to classical boundary. Reviews of Modern Physics* **85**, 1083 (2013).

[43] Wineland, D. J. *Nobel Lecture: Superposition, entanglement, and raising Schrödinger's cat. Reviews of Modern Physics* **85**, 1103 (2013).

[44] Predojević, A. & Mitchell, M. W. (eds.) *Engineering the Atom-Photon Interaction* (Springer International Publishing, 2015).

[45] Reiserer, A. & Rempe, G. *Cavity-based quantum networks with single atoms and optical photons. Reviews of Modern Physics* **87**, 1379 (2015).

[46] Rosenfeld, W., Burchardt, D., Garthoff, R., Redeker, K., Ortegel, N., Rau, M. & Weinfurter, H. *Event-Ready Bell Test Using Entangled Atoms Simultaneously Closing Detection and Locality Loopholes. Physical Review Letters* **119**, 010402 (2017).

[47] Sangouard, N., Simon, C., de Riedmatten, H. & Gisin, N. *Quantum repeaters based on atomic ensembles and linear optics. Reviews of Modern Physics* **83**, 33 (2011).

[48] Tiarks, D., Schmidt-Eberle, S., Stolz, T., Rempe, G. & Dürr, S. *A photon-photon quantum gate based on Rydberg interactions. Nature Physics* **15**, 124 (2019).

[49] Northup, T. & Blatt, R. *Quantum information transfer using photons. Nature Photonics* **8**, 356 (2014).

[50] Awschalom, D. D., Hanson, R., Wrachtrup, J. & Zhou, B. B. *Quantum technologies with optically interfaced solid-state spins. Nature Photonics* **12**, 516 (2018).

[51] Hadfield, R. H. *Single-photon detectors for optical quantum information applications. Nature Photonics* **3**, 696 (2009).

[52] Ritter, S., Nölleke, C., Hahn, C., Reiserer, A., Neuzner, A., Uphoff, M., Mücke, M., Figueroa, E., Bochmann, J. & Rempe, G. *An elementary quantum network of single atoms in optical cavities. Nature* **484**, 195 (2012).

[53] Nölleke, C., Neuzner, A., Reiserer, A., Hahn, C., Rempe, G. & Ritter, S. *Efficient Teleportation Between Remote Single-Atom Quantum Memories. Physical Review Letters* **110**, 140403 (2013).

[54] Hensen, B. *et al. Loophole-free Bell inequality violation using electron spins separated by 1.3 kilometres. Nature* **526**, 682 (2015).

[55] Giustina, M. *et al. Significant-Loophole-Free Test of Bell's Theorem with Entangled Photons. Physical Review Letters* **115**, 250401 (2015).

[56] Maring, N., Farrera, P., Kutluer, K., Mazzera, M., Heinze, G. & de Riedmatten, H. *Photonic quantum state transfer between a cold atomic gas and a crystal. Nature* **551**, 485 (2017).

[57] Boaron, A. *et al. Secure Quantum Key Distribution over 421 km of Optical Fiber. Physical Review Letters* **121**, 190502 (2018).

[58] Wilk, T., Webster, S. C., Kuhn, A. & Rempe, G. *Single-atom single-photon quantum interface. Science* **317**, 488 (2007).

[59] Cirac, J. I., Zoller, P., Kimble, H. J. & Mabuchi, H. *Quantum State Transfer and Entanglement Distribution among Distant Nodes in a Quantum Network. Physical Review Letters* **78**, 3221 (1997).

[60] Specht, H. P., Nölleke, C., Reiserer, A., Uphoff, M., Figueroa, E., Ritter, S. & Rempe, G. *A single-atom quantum memory. Nature* **473**, 190 (2011).

[61] Kalb, N., Reiserer, A., Ritter, S. & Rempe, G. *Heralded Storage of a Photonic Quantum Bit in a Single Atom. Physical Review Letters* **114**, 220501 (2015).

[62] Brekenfeld, M., Niemietz, D., Christesen, J. D. & Rempe, G. *A quantum network node with crossed optical fibre cavities. Nature Physics* **16**, 647 (2020).

[63] Körber, M., Morin, O., Langenfeld, S., Neuzner, A., Ritter, S. & Rempe, G. *Decoherence-protected memory for a single-photon qubit. Nature Photonics* **12**, 18 (2018).

[64] Neuzner, A., Körber, M., Morin, O., Ritter, S. & Rempe, G. *Interference and dynamics of light from a distance-controlled atom pair in an optical cavity. Nature Photonics* **10**, 303 (2016).

[65] Welte, S., Hacker, B., Daiss, S., Ritter, S. & Rempe, G. *Cavity Carving of Atomic Bell States. Physical Review Letters* **118**, 210503 (2017).

[66] Welte, S., Hacker, B., Daiss, S., Ritter, S. & Rempe, G. *Photon-Mediated Quantum Gate between Two Neutral Atoms in an Optical Cavity. Physical Review X* **8**, 011018 (2018).

[67] Kaufman, A., Lester, B., Foss-Feig, M., Wall, M., Rey, A. & Regal, C. *Entangling two transportable neutral atoms via local spin exchange. Nature* **527**, 208 (2015).

[68] Weiss, D. S. & Saffman, M. *Quantum computing with neutral atoms. Physics Today* **70**, 44 (2017).

[69] Gross, C. & Bloch, I. *Quantum simulations with ultracold atoms in optical lattices. Science* **357**, 995 (2017).

[70] Bernien, H. *et al. Probing many-body dynamics on a 51-atom quantum simulator. Nature* **551**, 579 (2017).

[71] Barredo, D., Lienhard, V., de Léséleuc, S., Lahaye, T. & Browaeys, A. *Synthetic three-dimensional atomic structures assembled atom by atom. Nature* **561**, 79 (2018).

[72] Covey, J. P., Madjarov, I. S., Cooper, A. & Endres, M. *2000-Times Repeated Imaging of Strontium Atoms in Clock-Magic Tweezer Arrays. Physical Review Letters* **122**, 173201 (2019).

[73] Bruzewicz, C. D., Chiaverini, J., McConnell, R. & Sage, J. M. *Trapped-ion quantum computing: Progress and challenges. Applied Physics Reviews* **6**, 021314 (2019).

[74] Borregaard, J., Kómár, P., Kessler, E. M., Lukin, M. D. & Sørensen, A. S. *Long-distance entanglement distribution using individual atoms in optical cavities. Physical Review A* **92**, 012307 (2015).

[75] Luong, D., Jiang, L., Kim, J. & Lütkenhaus, N. *Overcoming lossy channel bounds using a single quantum repeater node. Applied Physics B: Lasers and Optics* **122**, 96 (2016).

[76] Bochmann, J. *Coherent Dynamics and State Detection of Single Atoms in a Cavity.* Ph.D. Thesis, Max-Planck-Institut für Quantenoptik / Technische Universität München (2010).

[77] Dirac, P. A. M. *The Principles of Quantum Mechanics* (Oxford University Press, 1930).

[78] MacLennan, B. J. Analog Computation. In *Computational Complexity*, 161 (Springer New York, 2012).

[79] Bergmann, K., Theuer, H. & Shore, B. W. *Coherent population transfer among quantum states of atoms and molecules. Reviews of Modern Physics* **70**, 1003 (1998).

[80] Hennrich, M., Legero, T., Kuhn, A. & Rempe, G. *Vacuum-Stimulated Raman Scattering Based on Adiabatic Passage in a High-Finesse Optical Cavity. Physical Review Letters* **85**, 4872 (2000).

[81] Kuhn, A., Hennrich, M., Bondo, T. & Rempe, G. *Controlled generation of single photons from a strongly coupled atom-cavity system. Applied Physics B: Lasers and Optics* **69**, 373 (1999).

[82] Mücke, M., Bochmann, J., Hahn, C., Neuzner, A., Nölleke, C., Reiserer, A., Rempe, G. & Ritter, S. *Generation of single photons from an atom-cavity system. Physical Review A* **87**, 063805 (2013).

[83] Gorshkov, A. V., André, A., Lukin, M. D. & Sørensen, A. S. *Photon storage in Lambda-type optically dense atomic media. I. Cavity model. Physical Review A* **76**, 033804 (2007).

[84] Morin, O., Körber, M., Langenfeld, S. & Rempe, G. *Deterministic Shaping and Reshaping of Single-Photon Temporal Wave Functions. Physical Review Letters* **123**, 133602 (2019).

[85] Neuzner, A. *Resonance Fluorescence of an Atom Pair in an Optical Resonator.* Ph.D. Thesis, Max-Planck-Institut für Quantenoptik / Technische Universität München (2016).

[86] Steck, D. A. Rubidium 87 D Line Data (2015).

[87] Airy, G. B. *On the Diffration of an Object-glass with Circular Aperture. Transactions of the Cambridge Philosophical Society* (1835).

[88] Dalibard, J. & Cohen-Tannoudji, C. *Dressed-atom approach to atomic motion in laser light: the dipole force revisited. Journal of the Optical Society of America B* **2**, 1707 (1985).

[89] Nußmann, S., Murr, K., Hijlkema, M., Weber, B., Kuhn, A. & Rempe, G. *Vacuum-stimulated cooling of single atoms in three dimensions. Nature Physics* **1**, 122 (2005).

[90] Bochmann, J., Mücke, M., Guhl, C., Ritter, S., Rempe, G. & Moehring, D. L. *Lossless State Detection of Single Neutral Atoms. Physical Review Letters* **104**, 203601 (2010).

[91] Wang, Y., Zhang, X., Corcovilos, T. A., Kumar, A. & Weiss, D. S. *Coherent Addressing of Individual Neutral Atoms in a 3D Optical Lattice. Physical Review Letters* **115**, 043003 (2015).

[92] Garcia, S., Ferri, F., Reichel, J. & Long, R. *Overlapping two standing waves in a microcavity for a multi-atom photon interface. Optics Express* **28**, 15515 (2020).

[93] Samutpraphoot, P., Dorđević, T., Ocola, P. L., Bernien, H., Senko, C., Vuletić, V. & Lukin, M. D. *Strong Coupling of Two Individually Controlled Atoms via a Nanophotonic Cavity. Physical Review Letters* **124**, 063602 (2020).

[94] DiVincenzo, D. P. *The physical implementation of quantum computation. Fortschritte der Physik: Progress of Physics* **48**, 771 (2000).

[95] Heshami, K., England, D. G., Humphreys, P. C., Bustard, P. J., Acosta, V. M., Nunn, J. & Sussman, B. J. *Quantum memories: emerging applications and recent advances. Journal of Modern Optics* **63**, 2005 (2016).

[96] Choi, K. S., Deng, H., Laurat, J. & Kimble, H. J. *Mapping photonic entanglement into and out of a quantum memory. Nature* **452**, 67 (2008).

[97] de Riedmatten, H., Afzelius, M., Staudt, M. U., Simon, C. & Gisin, N. *A solid-state light-matter interface at the single-photon level. Nature* **456**, 773 (2008).

[98] Saglamyurek, E., Sinclair, N., Jin, J., Slater, J. A., Oblak, D., Bussieres, F., George, M., Ricken, R., Sohler, W. & Tittel, W. *Broadband waveguide quantum memory for entangled photons. Nature* **469**, 512 (2011).

[99] Yang, S. *et al. High-fidelity transfer and storage of photon states in a single nuclear spin. Nature Photonics* **10**, 507 (2016).

[100] Vernaz-Gris, P., Huang, K., Cao, M., Sheremet, A. S. & Laurat, J. *Highly-efficient quantum memory for polarization qubits in a spatially-multiplexed cold atomic ensemble. Nature Communications* **9**, 363 (2018).

[101] Jiang, N., Pu, Y.-F., Chang, W., Li, C., Zhang, S. & Duan, L.-M. *Experimental realization of 105-qubit random access quantum memory. npj Quantum Information* **5**, 28 (2019).

[102] Laplane, C., Jobez, P., Etesse, J., Timoney, N., Gisin, N. & Afzelius, M. *Multiplexed on-demand storage of polarization qubits in a crystal. New Journal of Physics* **18**, 013006 (2016).

[103] Tang, J.-S. *et al. Storage of multiple single-photon pulses emitted from a quantum dot in a solid-state quantum memory. Nature Communications* **6**, 9652 (2015).

[104] Jobez, P., Laplane, C., Timoney, N., Gisin, N., Ferrier, A., Goldner, P. & Afzelius, M. *Coherent Spin Control at the Quantum Level in an Ensemble-Based Optical Memory. Physical Review Letters* **114**, 230502 (2015).

[105] Holzäpfel, A., Etesse, J., Kaczmarek, K. T., Tiranov, A., Gisin, N. & Afzelius, M. *Optical storage for 0.53 s in a solid-state atomic frequency comb memory using dynamical decoupling. New Journal of Physics* **22**, 063009 (2020).

[106] Saglamyurek, E. *et al. A multiplexed light-matter interface for fibre-based quantum networks. Nature Communications* **7**, 11202 (2016).

[107] Nunn, J., Reim, K., Lee, K. C., Lorenz, V. O., Sussman, B. J., Walmsley, I. A. & Jaksch, D. *Multimode Memories in Atomic Ensembles. Physical Review Letters* **101**, 260502 (2008).

[108] van Enk, S. J., Cirac, J. I. & Zoller, P. *Ideal Quantum Communication over Noisy Channels: A Quantum Optical Implementation. Physical Review Letters* **78**, 4293 (1997).

[109] Muralidharan, S., Li, L., Kim, J., Lütkenhaus, N., Lukin, M. D. & Jiang, L. *Optimal architectures for long distance quantum communication. Scientific Reports* **6** (2016).

[110] Childress, L., Taylor, J. M., Sørensen, A. S. & Lukin, M. D. *Fault-Tolerant Quantum Communication Based on Solid-State Photon Emitters. Physical Review Letters* **96**, 070504 (2006).

[111] Jiang, L., Taylor, J. M., Sørensen, A. S. & Lukin, M. D. *Distributed quantum computation based on small quantum registers. Physical Review A* **76**, 062323 (2007).

[112] Giannelli, L., Schmit, T. & Morigi, G. *Weak coherent pulses for single-photon quantum memories. Physica Scripta* **94**, 014012 (2018).

[113] Ruster, T., Schmiegelow, C. T., Kaufmann, H., Warschburger, C., Schmidt-Kaler, F. & Poschinger, U. G. *A long-lived Zeeman trapped-ion qubit. Applied Physics B: Lasers and Optics* **122** (2016).

[114] Krutyanskiy, V., Meraner, M., Schupp, J., Krcmarsky, V., Hainzer, H. & Lanyon, B. P. *Light-matter entanglement over 50 km of optical fibre. npj Quantum Information* **5**, 72 (2019).

[115] Thiel, C., Böttger, T. & Cone, R. *Rare-earth-doped materials for applications in quantum information storage and signal processing. Journal of Luminescence* **131**, 353 (2011).

[116] Lidar, D. A., Chuang, I. L. & Whaley, K. B. *Decoherence-Free Subspaces for Quantum Computation. Physical Review Letters* **81**, 2594 (1998).

[117] Reiserer, A., Kalb, N., Blok, M. S., van Bemmelen, K. J., Taminiau, T. H., Hanson, R., Twitchen, D. J. & Markham, M. *Robust Quantum-Network Memory Using Decoherence-Protected Subspaces of Nuclear Spins. Physical Review X* **6**, 021040 (2016).

[118] Viola, L. & Lloyd, S. *Dynamical suppression of decoherence in two-state quantum systems. Physical Review A* **58**, 2733 (1998).

[119] de Lange, G., Wang, Z. H., Riste, D., Dobrovitski, V. V. & Hanson, R. *Universal Dynamical Decoupling of a Single Solid-State Spin from a Spin Bath. Science* **330**, 60 (2010).

[120] Merkel, B., Farina, P. C., Valencia, N. H. & Reiserer, A. *Dynamical decoupling of interacting anisotropic spin ensembles. arXiv:2005.08822* (2020).

[121] Shor, P. W. *Scheme for reducing decoherence in quantum computer memory. Physical Review A* **52**, R2493 (1995).

[122] Cory, D. G., Price, M. D., Maas, W., Knill, E., Laflamme, R., Zurek, W. H., Havel, T. F. & Somaroo, S. S. *Experimental Quantum Error Correction. Physical Review Letters* **81**, 2152 (1998).

[123] Chiaverini, J. *et al. Realization of quantum error correction. Nature* **432**, 602 (2004).

[124] Schindler, P., Barreiro, J. T., Monz, T., Nebendahl, V., Nigg, D., Chwalla, M., Hennrich, M. & Blatt, R. *Experimental repetitive quantum error correction. Science* **332**, 1059 (2011).

[125] Reed, M. D., DiCarlo, L., Nigg, S. E., Sun, L., Frunzio, L., Girvin, S. M. & Schoelkopf, R. J. *Realization of three-qubit quantum error correction with superconducting circuits. Nature* **482**, 382 (2012).

[126] Hahn, E. L. *Spin Echoes. Physical Review* **80**, 580 (1950).

[127] Viola, L., Knill, E. & Lloyd, S. *Dynamical Decoupling of Open Quantum Systems. Physical Review Letters* **82**, 2417 (1999).

[128] Carr, H. Y. & Purcell, E. M. *Effects of Diffusion on Free Precession in Nuclear Magnetic Resonance Experiments. Physical Review* **94**, 630 (1954).

[129] Meiboom, S. & Gill, D. *Modified Spin-Echo Method for Measuring Nuclear Relaxation Times. Review of Scientific Instruments* **29**, 688 (1958).

[130] Maudsley, A. *Modified Carr-Purcell-Meiboom-Gill sequence for NMR fourier imaging applications. Journal of Magnetic Resonance (1969)* **69**, 488 (1986).

[131] Uphoff, M. *State manipulation of single atoms in an optical cavity.* Diploma Thesis, Max-Planck-Institut für Quantenoptik / Technische Universität München (2010).

[132] Ahmed, M. A. A., Álvarez, G. A. & Suter, D. *Robustness of dynamical decoupling sequences. Physical Review A* **87**, 042309 (2013).

[133] Scarani, V., Bechmann-Pasquinucci, H., Cerf, N. J., Dušek, M., Lütkenhaus, N. & Peev, M. *The security of practical quantum key distribution. Reviews of Modern Physics* **81**, 1301 (2009).

[134] Shor, P. W. & Preskill, J. *Simple Proof of Security of the BB84 Quantum Key Distribution Protocol. Physical Review Letters* **85**, 441 (2000).

[135] Wegman, M. N. & Carter, J. *New hash functions and their use in authentication and set equality. Journal of Computer and System Sciences* **22**, 265 (1981).

[136] Bennett, C., Brassard, G., Crepeau, C. & Maurer, U. *Generalized privacy amplification. IEEE Transactions on Information Theory* **41**, 1915 (1995).

[137] Scarani, V. & Renner, R. *Quantum Cryptography with Finite Resources: Unconditional Security Bound for Discrete-Variable Protocols with One-Way Postprocessing. Physical Review Letters* **100**, 200501 (2008).

[138] Shannon, C. E. *A Mathematical Theory of Communication. Bell System Technical Journal* **27**, 379 (1948).

[139] Lucamarini, M., Yuan, Z. L., Dynes, J. F. & Shields, A. J. *Overcoming the rate–distance limit of quantum key distribution without quantum repeaters. Nature* **557**, 400 (2018).

[140] Zwerger, M., Lanyon, B. P., Northup, T. E., Muschik, C. A., Dür, W. & Sangouard, N. *Quantum repeaters based on trapped ions with decoherence-free subspace encoding. Quantum Science and Technology* **2**, 044001 (2017).

[141] Rozpędek, F., Goodenough, K., Ribeiro, J., Kalb, N., Vivoli, V. C., Reiserer, A., Hanson, R., Wehner, S. & Elkouss, D. *Parameter regimes for a single sequential quantum repeater. Quantum Science and Technology* **3**, 034002 (2018).

[142] van Loock, P. *et al. Extending Quantum Links: Modules for Fiber- and Memory-Based Quantum Repeaters. arXiv:1912.10123* (2019).

[143] Santra, S., Muralidharan, S., Lichtman, M., Jiang, L., Monroe, C. & Malinovsky, V. S. *Quantum repeaters based on two species trapped ions. New Journal of Physics* **21**, 073002 (2019).

[144] Awschalom, D. *et al. Development of Quantum InterConnects for Next-Generation Information Technologies. arXiv:1912.06642* (2019).

[145] Sharman, K., Asadi, F. K., Wein, S. C. & Simon, C. *Quantum repeaters based on individual electron spins and nuclear-spin-ensemble memories in quantum dots. arXiv:2010.13863* (2020).

[146] Goodenough, K., Elkouss, D. & Wehner, S. *Optimising repeater schemes for the quantum internet. arXiv:2006.12221* (2020).

[147] Gottesman, D. & Lo, H.-K. *Proof of security of quantum key distribution with two-way classical communications. IEEE Transactions on Information Theory* **49**, 457 (2003).

[148] Bhaskar, M. K. *et al. Experimental demonstration of memory-enhanced quantum communication. Nature* **580**, 60 (2020).

[149] Casabone, B., Stute, A., Friebe, K., Brandstätter, B., Schüppert, K., Blatt, R. & Northup, T. E. *Heralded Entanglement of Two Ions in an Optical Cavity. Physical Review Letters* **111**, 100505 (2013).

[150] Bouwmeester, D., Pan, J.-W., Mattle, K., Eibl, M., Weinfurter, H. & Zeilinger, A. *Experimental quantum teleportation. Nature* **390**, 575 (1997).

[151] Lütkenhaus, N., Calsamiglia, J. & Suominen, K. A. *Bell measurements for teleportation. Physical Review A* **59**, 3295 (1999).

[152] Hong, C. K., Ou, Z. Y. & Mandel, L. *Measurement of subpicosecond time intervals between two photons by interference. Physical Review Letters* **59**, 2044 (1987).

[153] Duan, L.-M. & Kimble, H. J. *Efficient Engineering of Multiatom Entanglement through Single-Photon Detections. Physical Review Letters* **90**, 253601 (2003).

[154] *Surprisingly, there is no citeable reference for the introduction of a Lamb-Dicke parameter or regime.*

[155] Morin, O., Langenfeld, S., Körber, M. & Rempe, G. *Accurate photonic temporal mode analysis with reduced resources. Physical Review A* **101**, 013801 (2020).

[156] Hacker, B., Welte, S., Rempe, G. & Ritter, S. *A photon-photon quantum gate based on a single atom in an optical resonator. Nature* **536**, 193 (2016).

[157] Meraner, M., Mazloom, A., Krutyanskiy, V., Krcmarsky, V., Schupp, J., Fioretto, D., Sekatski, P., Northup, T. E., Sangouard, N. & Lanyon, B. P. *Indistinguishable photons from a trapped-ion quantum network node. arXiv:1912.09259* (2019).

[158] Lo, H.-K., Chau, H. & Ardehali, M. *Efficient Quantum Key Distribution Scheme and a Proof of Its Unconditional Security. Journal of Cryptology* **18**, 133 (2005).

[159] Levine, H., Keesling, A., Omran, A., Bernien, H., Schwartz, S., Zibrov, A. S., Endres, M., Greiner, M., Vuletić, V. & Lukin, M. D. *High-Fidelity Control and Entanglement of Rydberg-Atom Qubits. Physical Review Letters* **121**, 123603 (2018).

[160] Teller, M. *Single-ion addressing for high-fidelity quantum network protocols.* Master Thesis, University of Innsbruck (2017).

[161] Brandstätter, B. *et al. Integrated fiber-mirror ion trap for strong ion-cavity coupling. Review of Scientific Instruments* **84**, 123104 (2013).

[162] Bennett, C., Brassard, G., Popescu, S., Schumacher, B., Smolin, J. & Wootters, W. *Purification of Noisy Entanglement and Faithful Teleportation via Noisy Channels. Physical Review Letters* **76**, 722 (1996).

[163] Deutsch, D., Ekert, A., Jozsa, R., Macchiavello, C., Popescu, S. & Sanpera, A. *Quantum Privacy Amplification and the Security of Quantum Cryptography over Noisy Channels. Physical Review Letters* **77**, 2818 (1996).

[164] Kalb, N., Reiserer, A. A., Humphreys, P. C., Bakermans, J. J. W., Kamerling, S. J., Nickerson, N. H., Benjamin, S. C., Twitchen, D. J., Markham, M. & Hanson, R. *Entanglement distillation between solid-state quantum network nodes. Science* **356**, 928 (2017).

[165] Nölleke, C. *Quantum state transfer between remote single atoms.* Ph.D. Thesis, Max-Planck-Institut für Quantenoptik / Technische Universität München (2013).

[166] Gottesman, D. & Chuang, I. L. *Demonstrating the viability of universal quantum computation using teleportation and single-qubit operations. Nature* **402**, 390 (1999).

Acknowledgements

An dieser Stelle möchte ich allen Menschen danken, die mich in den letzten Jahren und darüber hinaus unterstützt und damit zum Erfolg dieser Arbeit beigetragen haben.

Zuallererst geht mein Dank an meinen Doktorvater Gerhard Rempe. Es war für mich keineswegs selbstverständlich, dass er mich als ehemaligen Festkörperphysiker ohne allzu viel Erfahrung in Quantenmechanik oder Optik einstellen würde. Er hat maßgeblich zu meiner Begeisterung für diese beiden Themen beigetragen und darüber hinaus alles bereit gestellt, was man sich als Experimentalphysiker nur wünschen kann.

Diese Art experimentelle Arbeit ist natürlich nicht alleine zu bewältigen. Mein Dank geht daher insbesondere an die aktuellen und auch früheren Mitglieder des „Pistol"-Experiments. Insbesondere möchte ich meinen Postdoc Olivier Morin, sowie meinen Vorgänger Matthias Körber und Nachfolger Philip Thomas nennen. Von allen habe ich fachlich sowie menschlich viel gelernt, und die unzähligen Messreihen und Messnächte wären ohne ihren Support schlicht nicht möglich gewesen. Auch danken möchte ich unserem früheren Senior Scientist Stephan Ritter, der mir gerade anfangs gut geholfen hat in dieses quasi unendliche Thema der Quanteninformation einzutauchen.

Während der kombinierten Messungen mit dem „QGates"-Team hatte ich viel Spaß in der Zusammenarbeit mit Stephan Welte, Emanuele Distante, Severin Daiss und Lukas Hartung. Das gleiche gilt für das „CavX"-Team, welches als weiterer Bestandteil des QIP-Teams unsere Gruppentreffen nicht nur mit Kuchen sehr bereichert hat. Im Institut sowie abseits davon waren Joe & Sarah Christesen, Dominik Niemietz und Pau Farrera sehr geschätzte Kollegen.

Innerhalb des Instituts gilt mein Dank auch ganz speziell unseren Technikern Tobias Urban, Florian Furchtsam und Johannes Siegl sowie unserem Elektroniker Thomas Wiesmeier. Von allen habe ich vieles gelernt, was auch nach meinem Doktor noch sehr nützlich sein wird. Ich möchte ihnen für Ihre schnelle und kompetente Unterstützung im Labor wie auch für private Projekte danken. Darüber hinaus war Iris Anneser als Teamassistenz eine unentbehrliche Kraft in Gerhards Vorzimmer.

Die Quantendynamik-Gruppe hat noch viele weitere großartige Mitglieder, denen ich an dieser Stelle für die tolle Arbeitsatmosphäre sowie gemeinsame Zeit auf Konferenzen danken möchte. Dazu zähle ich auch meine Büronachbarn der Quanten-Netzwerk-Gruppe, die zwischendurch für die nötige Ablenkung gesorgt haben.

Eine weitere Gruppe an die ich nur gute Erinnerungen behalten werde, ist die International Max Plank Research School (IMPRS) und damit insbesondere auch die Münchner Quantencommunity, mit denen ich informative und lustige Sommerschulen und Workshops hatte.

Abseites der wissenschaftlichen Arbeit möchte ich allen Mitgliedern des Betriebsrats danken, von denen ich menschlich einiges in unseren gemeinsamen Sitzungen lernen durfte, sowie für die wöchentliche Ablenkung mit Problemen aus einer ganz anderen Welt.

Da diese Arbeit auch ein Ergebnis meines früheren Studiums ist, möchte ich an dieser Stelle meinen früheren Gruppenleitern Alexander Holleitner an der Tum, Andrew Ferguson an der Universität Cambridge sowie dem damaligen Doktoranden Christoph Kastl, nun ebenfalls wieder an der TUM, danken. Durch sie habe ich meine Grundlagen in der experimentellen Physik, und dadurch auch die Motivation und notwendigen Werkzeuge für meine Doktorarbeit, erhalten.

Zu guter Letzt geht mein Dank an Freunde und Familie in- und außerhalb Münchens. Meinem Bruder danke ich für seine steten Erinnerungen, wie lange ich schon an meiner Doktorarbeit arbeite. Meinen Eltern und Ihren Partnern gebührt ein ganz besonderer Dank, da Sie mich über neun Jahre des Studiums und der Doktorarbeit kontinuierlich und bedingungslos unterstützt haben.

Herzlichen Dank euch allen!